

Aus der
Medizinischen Klinik und Poliklinik V
Klinikum der Ludwig-Maximilians-Universität München

und dem Comprehensive Pneumology Center Munich



**Lung Aging in a Dish:
Induction of senescence and pro-fibrotic changes in
human precision-cut lung slices**

Dissertation
zum Erwerb des Doctor of Philosophy (Ph.D.)
an der Medizinischen Fakultät der
Ludwig-Maximilians-Universität München

vorgelegt von
Maria Camila Melo Narvaez

aus
Bogotá, Kolumbien

Jahr
2023

Mit Genehmigung der Medizinischen Fakultät der
Ludwig-Maximilians-Universität München

Erstes Gutachten: Prof. Dr. Jürgen Behr
Zweites Gutachten: Prof. Dr. Mareike Lehmann
Drittes Gutachten: Prof. Dr. Alexander Dietrich
Viertes Gutachten: Priv. Doz. Dr. Claus Neurohr

Dekan: Prof. Dr. med. Thomas Gudermann

Tag der mündlichen Prüfung: 13.12.2023

Table of Contents

List of Figures	vii
List of Tables	ix
Abstract	xi
1 Introduction	1
1.1 Hallmarks of aging	1
1.2 Cellular senescence	2
1.3 Induction of cellular senescence	3
1.3.1 Ionizing radiation	4
1.4 Characterization of Cellular senescence	4
1.4.1 Nuclear modifications	4
1.4.2 Cell cycle arrest	5
1.4.3 Senescence-Associated β -Galactosidase	6
1.4.4 Senescence-associated secretory phenotype	7
1.5 Cellular senescence and chronic lung diseases	8
1.5.1 Idiopathic Pulmonary Fibrosis	8
1.6 Models of pulmonary fibrosis	11
1.6.1 Animal models	11
1.6.2 Translational models	12
1.7 Targeting Cellular senescence: Senolytics	13
1.7.1 Dasatinib + Quercetin	14
1.7.2 ABT-263: Navitoclax	15
1.8 Hypothesis and objectives	16

2 Materials	19
2.1 Human material	19
2.2 Animal experiments	22
2.3 Primary human and mouse cells	22
2.4 Primers	23
2.5 Reagents	24
2.6 Commercial kits	26
2.7 Enzymes and proteins	27
2.8 Consumables	27
2.9 Laboratory equipment	29
2.10 Software	30
2.11 Antibodies	31
3 Methods	33
3.1 Precision-Cut lung slices	33
3.2 Ionizing radiation exposure	33
3.3 WST-1 assay	34
3.4 LDH assay	34
3.5 Senescence-Associated β -Galactosidase on fresh tissue	34
3.6 RNA isolation from PCLS	35
3.7 cDNA synthesis and RT-qPCR	35
3.8 Bulk RNA-Sequencing	36
3.9 Differential expression analysis	36
3.10 Formalin-Fixed Paraffin-Embedding of PCLS	37
3.11 Immunofluorescence of fresh tissue	37
3.12 Immunofluorescence of FFPE sections	37
3.13 Immunofluorescence of cells	38
3.14 MACS sorting from mPCLS	38
3.15 MACS sorting from hPCLS	39
3.16 Organoid assay	39
3.17 Protein quantification of PCLS supernatants	40
3.18 ELISA	40
3.19 Cytokine arrays	41
3.20 Senolytics treatment on PCLS	42
3.21 Cripto-1 treatment on cells and PCLS	42

4 Results	45
4.1 Validation of radiation-induced senescence in murine and human PCLS	45
4.1.1 IR induces DNA damage response in PCLS	45
4.1.2 IR does not reduce metabolic activity or viability of PCLS	45
4.1.3 IR induces P21-dependent cell cycle arrest in PCLS	47
4.1.4 Senescence-Associated β -Galactosidase activity is increased in IR-PCLS	49
4.1.5 IR-PCLS have a distinct senescence-associated secretory phenotype	49
4.2 Characterization of radiation-induced cellular senescence in human PCLS .	50
4.2.1 Transcriptomics reveal a premature aging phenotype in IR-hPCLS .	50
4.2.2 IR induces epithelial cellular senescence in hPCLS	52
4.2.3 Stem cell potential of epithelial lung progenitors is reduced in IR-hPCLS	53
4.2.4 SASP from IR-PCLS is temporally dynamic and induces immune response modulation via inflammatory mediators	54
4.3 Characterization of radiation-induced fibrotic-like changes in human PCLS	57
4.3.1 IR-PCLS have an upregulation in pro-fibrotic markers and ECM deposition	57
4.4 Pre-clinical testing of senolytics	58
4.4.1 Senolytics reduce senescence and fibrotic burden in IR-PCLS	58
4.5 Discovery of potential biomarkers and therapeutic targets	60
4.5.1 Novel secreted factor CRIPTO1 is pro-fibrotic in hPCLS	60
4.5.2 Novel secreted factor CRIPTO1 activates primary lung fibroblasts in vitro	61
5 Discussion	65
5.1 Induction of cellular senescence in lung tissue ex vivo	66
5.2 Identification of the main senescent cellular compartments in IR-hPCLS . .	67
5.3 Characterization of senescence-induced pro-fibrotic signaling in IR-hPCLS	68
5.4 Discovery of a novel senescence-related secreted factor with pro-fibrotic activity in the lung	70
5.5 Pre-clinical testing of senolytics to target senescence-induced pro-fibrotic signaling in IR-hPCLS	71
5.6 Limitations and conclusions	73

6 Supplementary Material	77
6.1 Supplementary Figures	77
6.2 Supplementary Tables	80
List of Abbreviations	85
References	89
Acknowledgments	111
Curriculum vitae	113
List of publications	115
Affidavit	116
Confirmation of congruency	117

List of Figures

1.1	Global incidence rate of chronic lung diseases	2
1.2	Hallmarks of cellular senescence and the dual role in health and disease	5
1.3	Pathogenesis of pulmonary fibrosis	9
1.4	Hypothesis and Milestones	16
4.1	Induction of DNA damage response after ionizing radiation of PCLS.	46
4.2	Assessment of viability and metabolic activity in IR-PCLS	47
4.3	Characterization of cell cycle arrest induction over time after IR	48
4.4	Induction of SA- β -Galactosidase activity in IR-PCLS	50
4.5	Profiling the senescence-Associated secretory phenotype of IR-PCLS	51
4.6	Transcriptional changes in IR-PCLS	52
4.7	Epithelial cellular senescence in IR-Human Precision-cut lung slices (hPCLS)	54
4.8	Stem cell capacity of alveolar progenitors in IR-hPCLS	55
4.9	Longitudinal temporal characterization of SASP from IR-PCLS	56
4.10	Expression of pro-fibrotic markers and ECM deposition in IR-hPCLS	58
4.11	Reduction of senescence- and fibrotic-related markers on IR-PCLS after treatment with senolytics	59
4.12	Assessment of pro-fibrotic changes after teratocarcinoma-derived growth factor 1 (CRIPTO1) treatment on PCLS	61
4.13	Assessment of pro-fibrotic changes after CRIPTO1 treatment on primary human lung fibroblasts	62
6.1	Immunofluorescence of hPCLS-derived organoids.	77
6.2	Organoid assay from mPCLS	78
6.3	Longitudinal characterization of SASP from IR-PCLS	79
6.4	Gene set enrichment for a fibrosis-related gene set	80

List of Tables

2.1	Patient information from tissues used for PCLS generation	19
2.2	Patient information from Bronchoalveolar lavage fluid samples.	21
2.3	Patient data from primary human fibroblasts used in this study.	22
2.4	Primers used for expression analysis by RT-qPCR.	23
2.5	Laboratory reagents.	24
2.6	Commercial kits.	26
2.7	Enzymes and recombinant proteins.	27
2.8	Laboratory Consumables.	28
2.9	Laboratory equipment.	29
2.10	Software	30
2.11	Primary antibodies used for immunofluorescence	31
2.12	Secondary antibodies used for immunofluorescence	32
3.1	Ionizing radiation doses	34
3.2	cDNA synthesis mix preparation	36
3.3	Organoids culturing medium	40
3.4	Senolytic treatment on PCLS	42
6.1	Top 50 differentially expressed genes in IR-hPCLS.	80
6.2	Cytokines upregulated in IR-PCLS.	82

Abstract

Aging is a natural process characterized by reduced regeneration capacity and therefore, is the main risk factor for chronic lung diseases such as Idiopathic Pulmonary Fibrosis (IPF). Accordingly, several hallmarks of aging such as cellular senescence are increased in fibrotic lungs and have been linked to its pathobiology. Precision-cut lung slices (PCLS) preserve the cellular diversity and architecture of the lung. Therefore, PCLS from bleomycin-treated mice or IPF patients have been used in the past to study the pathobiology of IPF. However, IPF-derived PCLS represent an end stage of the disease and therefore cannot be used to study or target the early changes that initiate the tissue remodeling observed in these patients. To study aging-related mechanisms involved in the pathogenesis of pulmonary fibrosis, we exposed PCLS to ionizing radiation (IR) and evaluated the induction of senescence- and fibrotic-related markers longitudinally. Induction of DNA damage was confirmed by immunofluorescence (IF). Metabolic activity was measured with a WST-1 assay and cytotoxicity was determined using an LDH assay. Apoptosis induction was determined by IF of cleaved-caspase 3 (CC3). Bulk RNA-sequencing was used to characterize transcriptional changes in irradiated precision-cut lung slices (IR-PCLS) at 7 days post irradiation (dpi). Expression of senescence and fibrosis markers after IR and senolytic treatment were evaluated by RT-qPCR or IF. The progenitor capacity of the alveolar epithelium was assessed in organoid assays. The senescence-Associated Secretory Phenotype (SASP) was longitudinally profiled using cytokine arrays and ELISA and compared to the secreted factors in bronchoalveolar lavage fluid (BALF) samples from control and IPF patients. Finally, pro-fibrotic changes after exposure to a novel secreted factor from irradiated human PCLS (IR-hPCLS) were evaluated by RT-qPCR and IF. IR-PCLS remained viable and metabolic active at 7 dpi with no significant increase in LDH release or apoptosis. IR induced DNA damage (phosphorylated H2A histone family member X (γ H2Ax)) as early as 1 h, cyclin dependent kinase inhibitor 1A (*CDKN1A*/P21)-dependent cell cycle

arrest, and senescence-associated β -Galactosidase (SA- β -gal) activity at 7 dpi. Senescence was mainly induced in the epithelial compartment as showed by reduced progenitor capacity and increased *CDKN1A/P21* expression in alveolar type I (AT1) and alveolar type II (AT2) cells. Transcriptomics and longitudinal SASP profiling showed upregulation of pathways related to inflammation, DNA damage, epithelial reprogramming, and senescence. Moreover, IR-hPCLS downregulated pathways involved in cell cycle progression. Fibrosis-related markers such as smooth Muscle Actin Alpha 2 (ACTA2), plasminogen Activator Inhibitor 1 (PAI-1), and transforming Growth Factor Beta (TGF- β 1) were significantly induced in IR-hPCLS. Moreover, early changes related to collagen biogenesis were observed at 7 dpi. Notably, senescence- and fibrosis-related markers could be reversed by treatment with the senolytics Navitoclax (ABT-263) and Dasatinib + Quercetin (DQ), which significantly reduced *CDKN1A/P21* expression and growth Differentiation Factor 15 (GDF-15) secretion in IR-hPCLS. Finally, a novel secreted factor (CRIPTO1) was identified in the SASP and confirmed to be upregulated at both gene and protein levels in IR-hPCLS. Moreover, CRIPTO1 showed pro-fibrotic effects on both hPCLS and primary human lung fibroblasts (phLF) as shown by significant upregulation of ACTA2 expression. In conclusion, we present a novel ex vivo model of distal epithelial cellular senescence and early fibrotic changes that allowed the discovery of a potential biomarker for IPF.

Chapter 1

Introduction

1.1 Hallmarks of aging

Aging is a natural and progressive cellular process that leads to tissue deterioration and altered organ function as well as increased susceptibility to disease (Schneider et al., 2021). Therefore, aging is the main risk factor for several chronic diseases such as cancer, cardiovascular diseases, and chronic lung diseases (CLDs) (Childs et al., 2017; S. Lee et al., 2021; López-Otín et al., 2013; Meiners et al., 2015; Schroth et al., 2020; Xie et al., 2020). Globally, population size and life expectancy are rising and it is expected that by 2050, 16% of the global population will be older than 65 years old (Chaib et al., 2022; United Nations Department of Economic and Social Affairs, Population Division, 2022; Xie et al., 2020). Given that the incidence of CLDs such as interstitial lung diseases (ILDs) or Chronic Obstructive Pulmonary Disease (COPD) dramatically increases with age (Fig. 1.1), understanding the molecular mechanisms behind cellular aging, its role in CLDs, and the discovery of potential targets have become very relevant in the last years. In this effort, several hallmarks of aging have been described and kept updated (López-Otín et al., 2023). These hallmarks include cellular and molecular changes that: 1) increase during physiological aging, 2) accelerate aging when artificially induced in experimental models, and 3) when therapeutically targeted, lead to attenuation or reversal of the age-related phenotypes (López-Otín et al., 2023). The new hallmarks of aging include genomic instability, telomere attrition, epigenetic alterations, loss of proteostasis, deregulated nutrient-sensing, mitochondrial dysfunction, cellular senescence, stem cell exhaustion, disabled macroautophagy,

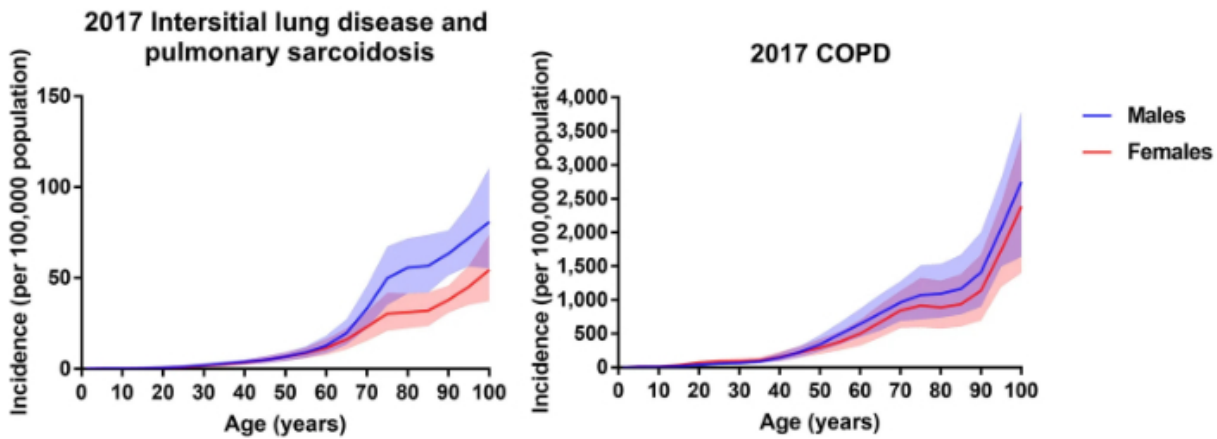


Figure 1.1: Global incidence rate of chronic lung diseases. The incidence of CLDs such as ILDs and COPD increase with age in both females and males. Shade indicates 95% uncertainty intervals. Modified and distributed from Xie et al., 2020 according to the terms of the Creative Commons Attribution 4.0 International License <https://creativecommons.org/licenses/by/4.0/>

chronic inflammation, and dysbiosis (López-Otín et al., 2013, 2023; Schmauck-Medina et al., 2022). All these hallmarks have been shown to increase during aging and current studies focus on targeting these pathways to improve health- and lifespan.

1.2 Cellular senescence

Cellular senescence is a biological response to stress in which cells enter a stable cell cycle arrest and have a deregulated metabolic activity (Basisty et al., 2020; DePianto et al., 2021). This irreversible cell cycle arrest can be maintained either by the tumor Suppressor P53 (TP53)/*CDKN1A*/P21 axis or the phosphorylated Retinoblastoma protein (pRB)/cyclin dependent kinase inhibitor 2A (*CDKN2A*/P16) axis (Chaib et al., 2022; González-Gualda et al., 2021). Moreover, senescent cells have an upregulation of SA- β -gal activity and secrete a large variety of chemokines, growth factors, proteases, and cytokines known as the SASP (Basisty et al., 2020; DePianto et al., 2021). Under homeostatic conditions, senescent cells modulate their microenvironment by recruiting immune cells to remove senescent cells, activating wound healing, and promoting tissue repair (Basisty et al., 2020; Ovadja et al., 2018). This self-limited cellular senescence plays an important role during embryogenesis and tumor suppression (DePianto et al., 2021; Kang et al., 2011; Lujambio et al., 2013; Xue et al., 2007). However, with aging and under chronic injury, senescent cells accumulate and promote age-related hallmarks such as chronic inflamma-

tion, stem-cell dysfunction, and organ fibrosis (Basisty et al., 2020; DePianto et al., 2021; Dimri et al., 1995; Ovadya et al., 2018). This accumulation of senescent cells has been described in numerous chronic diseases and during chronological aging (Chaib et al., 2022; DePianto et al., 2021; Ovadya et al., 2018), however, the mechanism behind it is still under investigation. Current hypothesis proposed an immune clearance escape either by active autocrine/paracrine modulation of the immune response by senescent cells (Chaib et al., 2022; Pereira et al., 2019; T.-W. Wang et al., 2022) or impaired immune response linked to physiological aging (Montecino-Rodriguez et al., 2013; Ovadya et al., 2018; Weng et al., 2009). Moreover, senescent cells upregulate several pro-survival and anti-apoptotic pathways, which again support their accumulation in different organs with age (Chaib et al., 2022).

1.3 Induction of cellular senescence

Cellular senescence can be triggered by different external stimuli as well as a result of biological processes such as oxidative respiration or replication (Campisi and d'Adda di Fagagna, 2007; Coppé et al., 2010; DePianto et al., 2021). Moreover, other cellular alterations such as mitochondrial dysfunction, increased endoplasmic reticulum stress, or altered proteostasis can also lead to cellular senescence (Campisi and d'Adda di Fagagna, 2007; Coppé et al., 2010; DePianto et al., 2021; Di Micco et al., 2021). Irreversible DNA damage mainly present as DNA double-strand breaks (DSBs), is one of the most common triggers of cellular senescence both *in vivo* and *in vitro* (Di Micco et al., 2021). This DNA damage response can be induced by natural causes such as telomere shortening linked to the aging process or spontaneous activation of oncogenes like RAS or BRAF (Campisi and d'Adda di Fagagna, 2007; Coppé et al., 2010; DePianto et al., 2021; Di Micco et al., 2021). Moreover, exposure to external genotoxic compounds such as the chemotherapy drugs bleomycin or etoposide (Bramey et al., 2023; Schafer et al., 2017), oxidizing agents like oxygen peroxide (H_2O_2) (Bramey et al., 2023), or ionizing radiation (Schafer et al., 2017) can also lead to DSBs-dependent DNA-damage response (DDR) response (Campisi and d'Adda di Fagagna, 2007; Coppé et al., 2010; DePianto et al., 2021; Di Micco et al., 2021). Therefore, exposure to all these stimuli have been used *in vitro* to mimic DNA damage-induced cellular senescence in several cell types and in mouse models to study its role in health and disease (Bramey et al., 2023; Campisi and d'Adda di Fagagna, 2007; Coppé et al., 2010; DePianto et al., 2021; Di Micco et al., 2021; Schafer et al., 2017).

1.3.1 Ionizing radiation

IR causes single- and double-strand DNA breaks as well as oxidative DNA lesions (Li et al., 2001). These lesions activate DDR-related proteins, inhibiting cell cycle progression until the DNA integrity is restored (Li et al., 2001). One of the main proteins involved in the DDR activation, is the ataxia telangiectasia-mutated protein (ATM) kinase, which detects the DNA damage and phosphorylates different tumor suppressor proteins such TP53 or breast cancer gene 1 (BRCA1) (Canman et al., 1998; Li et al., 2001). Cell susceptibility and response to IR have been linked to the exposure dose, cell origin, and genetic alterations in the DDR machinery (Chen et al., 2019; Noda et al., 2012). For example, higher doses can lead to apoptosis whereas lower doses induce cellular senescence (Chen et al., 2019; Noda et al., 2012; Y. Wang et al., 2016). Therefore, IR has been extensively used to induce cell death in tumor cells and as a model for DNA-damage-induced senescence in several cell types (Alessio et al., 2014; Chen et al., 2019; Noda et al., 2012; Sadhu et al., 2021; Schafer et al., 2017).

1.4 Characterization of Cellular senescence

The senescent phenotype is very variable depending, for example, on the cell type or the trigger (Gasek et al., 2021; Tang et al., 2019; Wiley et al., 2017). Moreover, there is a low prevalence of senescent cells *in vivo* and the senescence program has a very high cellular and temporal heterogeneity (Gasek et al., 2021; Tang et al., 2019). Therefore, establishing a unique definition of a senescent cell has been very challenging in the field. However, there have been several efforts in recent years to establish a consensus to define the senescent phenotype, proposing different hallmarks of cellular senescence (Fig.1.2). These include nuclear and morphological changes, cell cycle arrest, reduced proliferation, resistance to apoptosis, stem cell exhaustion, increased SA- β -gal, and the SASP (Hernandez-Segura et al., 2018).

1.4.1 Nuclear modifications

After DNA damage or cellular stress, cells undergo several changes in their chromatin in order to suppress proliferation and prevent the spread of damaged cells. For this, the chromatin condenses in senescence-associated heterochromatin foci (SAHFs), which can be detected by 4,6-diamidino-2-phenylindole (DAPI) staining or immune-based detection

of proteins that accumulate around these sites like heterochromatin protein 1 (HP1), trimethylated 9th lysine residue of the histone H3 protein (H3K9me3), and the histone H2A variant macroH2A (T. Chandra and Narita, 2013; González-Gualda et al., 2021). Other structures, known as DNA segments with chromatin alterations reinforcing senescence (DNA-SCARS), which are associated with DDR or telomere dysfunction can also be detected in senescent cells (Anderson et al., 2019; González-Gualda et al., 2021; Victorelli and Passos, 2017). Among them, γ H2Ax is a widely used marker since it accumulates in senescent cells even without any DNA-damaging agent (González-Gualda et al., 2021; Noda et al., 2012; Pospelova et al., 2009; Rodier et al., 2011) (Fig. 1.2). Moreover, senescent cells lose their nuclear integrity and have a lower expression of Lamin B1 on the nuclear lamina (Freund et al., 2012).

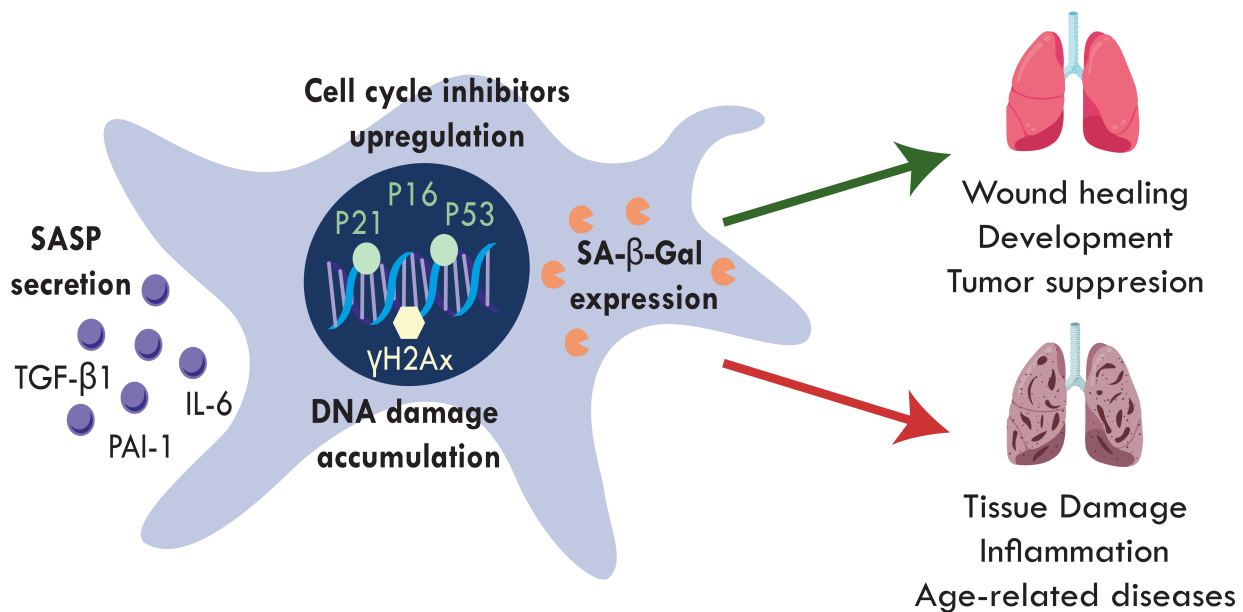


Figure 1.2: Hallmarks of cellular senescence and the dual role in health and disease. Senescent cells undergo several cellular changes such as upregulation of cell cycle inhibitors (P21, P16, and TP53) as well as nuclear accumulation of γ H2Ax foci. They also have increased SA- β -gal activity and secrete growth factors and cytokines known as the SASP. Senescent cells play an important role during development, homeostatic tissue repair, and as a tumor suppressor mechanism. However, the accumulation of senescent cells promotes inflammation and tissue damage, which has been linked to the pathogenesis of different age-related diseases.

1.4.2 Cell cycle arrest

Cell cycle arrest is one of the main markers of senescent cells and it is regulated by the *CDKN2A*/P16 and *CDKN1A*/P21 cyclin-dependent kinase inhibitors (Fig. 1.2). The

pRB is usually phosphorylated by the cyclin D/CDK4, Cyclin D/CDK6, and Cyclin E/CDK2 complexes, inhibiting its binding to the E2F transcription factor and promoting cell cycle progression (González-Gualda et al., 2021; Stein et al., 1999). However, both *CDKN2A*/P16 and *CDKN1A*/P21 can inhibit the activity of these cyclin-dependent kinases, thereby inducing cell cycle arrest (González-Gualda et al., 2021; Stein et al., 1999). The *CDKN1A*/P21 pathway is initially induced by phosphorylation of TP53 as a response to DNA damage. This upregulates *CDKN1A*/P21, which by inhibiting the CDK2-Cyclin E complex, facilitates the formation of the dephosphorylated RB and E2F complex stopping the cell cycle (Beauséjour et al., 2003; González-Gualda et al., 2021; Stein et al., 1999). On the *CDKN2A*/P16 pathway, inhibition of the CDK4/6- Cyclin D complex by activated *CDKN2A*/P16 also leads to RB/E2F-dependent cell cycle arrest (Dulić et al., 2000; González-Gualda et al., 2021; Stein et al., 1999). Although both pathways can induce senescence, this highly depends on the initial stimulus. The *CDKN1A*/P21/TP53 pathway activation has been observed in replicative, DDR-, reactive oxygen species (ROS)-, and oncogene-induced senescence (González-Gualda et al., 2021). On the other hand, the *CDKN2A*/P16/RB pathway is induced by replication and ROS but not by DDR (González-Gualda et al., 2021). Interestingly, temporal distinctions have also been observed, suggesting that the *CDKN1A*/P21/TP53 axis is activated in the initial phase, whereas, the *CDKN2A*/P16/pRB pathway has a main role in sustaining the senescent phenotype in the long term (Dulić et al., 2000; González-Gualda et al., 2021).

1.4.3 Senescence-Associated β -Galactosidase

The increased activity of the lysosomal hydrolase, known as the SA- β -gal, is the most commonly used marker to identify senescent cells (Fig. 1.2). This enzyme is encoded by the *GLB1* gene, which is upregulated in senescent cells but is not essential for senescence induction and establishment (B. Y. Lee et al., 2006). Since only senescent cells showed increased activity of SA- β -gal at pH 6.0, this phenotype was used to establish a histochemical assay for its detection (de Mera-Rodríguez et al., 2021; Dimri et al., 1995). Here, a colorless and soluble substrate known as 5-bromo-4-chloro-3-indoyl--d-galactopyranoside (X-gal) is given to the cells, in which the SA- β -gal enzyme cleaves this substrate producing a deep-blue color that can be directly detected by bright-field microscopy (de Mera-Rodríguez et al., 2021; B. Y. Lee et al., 2006). This technique has been extensively used to describe senescent cells in both cultured cells and tissues, however, single-cell resolution is not possible with this technique. Therefore, some fluorescence-based assays have been developed in the last

years, such as 5-dodecanoylaminofluorescein-di- β -D-galactopyranoside (C₁₂FDG) (Plovins et al., 1994) and SPiDER- β Gal (Doura et al., 2016). These reagents can specifically detect SA- β -gal, after inhibition of the acidic β -galactosidase activity (pH 4) in lysosomes with bafilomycin A1 (BafA1) (Debacq-Chainiaux et al., 2009). BafA1 is an ATPase inhibitor that prevents the acidification of lysosomes (Debacq-Chainiaux et al., 2009), therefore can be used to selectively detect SA- β -gal activity, which is only detectable at a pH of 6 (Kurz et al., 2000). After this step, cells or tissues are incubated with the non-fluorescent probes, that after being hydrolyzed, are retained inside the cells and generate a fluorescent signal that can be detected by fluorescence microscopy (Doura et al., 2016). These probes allow a better characterization of senescent cells at the single-cell level, for example, by co-staining with specific cellular markers *in situ* or for flow cytometry analysis. Although increased SA- β -gal is present in senescent cells, it is important to consider that high levels of β -Galactosidase have been also reported during development, in immortalized cells, macrophages, neurons, and among different tissues such as heart, intestine, and pancreas (B. Y. Lee et al., 2006). Therefore, the current consensus recommends a combination of all the markers described until now to define senescent cells.

1.4.4 Senescence-associated secretory phenotype

The SASP is composed of several growth factors, cytokines, metalloproteases, and chemokines, which are either directly secreted to the extracellular space or transported in extracellular vesicles (Basisty et al., 2020; Chaib et al., 2022; Coppé et al., 2010; Coppé et al., 2008; Kumari and Jat, 2021) (Fig. 1.2). The composition of the SASP is highly variable, changing for example, for different cell types, inducers, localization, or time point (Basisty et al., 2020; Chaib et al., 2022; Hernandez-Segura et al., 2017; Kumari and Jat, 2021). Recent efforts have been focused on defining core SASP components that could be used as biomarkers for senescent cells (Basisty et al., 2020; S. Kim and Kim, 2021). In this way, several secreted factors such as interleukin 6 (IL-6), interleukin 1 Alpha (IL-1 α), interleukin 15 (IL-15), interleukin 8 (IL-8), C-X-C Motif Chemokine Ligand 1 (CXCL1), tumor necrosis factor alpha (TNF- α), TGF- β 1, C-C Motif Chemokine Ligand 2 (CCL2), Chemokine (C-X-C motif) ligand 2 (CXCL2), C-C Motif Chemokine Ligand 3 (CCL3), interferon Gamma (IFN γ), vascular Endothelial Growth Factor A (VEGFA), intercellular Adhesion Molecule 1 (ICAM-1), PAI-1, serine protease inhibitors (SERPINs), and GDF-15 among others, have been described to be secreted by senescent cells (Basisty et al., 2020). However, despite the efforts there is not a universal combination of secreted factors that

defines every senescent cell. The SASP components' expression and secretion are regulated by several signaling pathways that depend mainly on the activation of two transcription factors: nuclear factor kappa B (NF- κ B) and CCAAT Enhancer Binding Protein Beta (CEBP β). Traditional senescence triggers activate these transcription factors, which sustain senescence by autocrine signaling and can induce paracrine senescence in neighboring cells (Acosta et al., 2013; Kumari and Jat, 2021). For this reason, the SASP plays a very important role in the beneficial or detrimental effects of senescent cells on their microenvironment (Chaib et al., 2022; Coppé et al., 2008). Being able to distinguish between the good and the bad senescence would allow for the discovery of novel targets and therapies for age-related diseases.

1.5 Cellular senescence and chronic lung diseases

The lung is a unique organ, constantly exposed to environmental stressors such as cigarette smoke, toxic particles, pollen, or microorganisms that cause injury to the airways and distal regions of the lung (Meiners et al., 2015; Schneider et al., 2021). Under normal circumstances, our immune system is able to clear and promote the repair of lung tissue. However, chronic injury and aging reduce immune clearance, promoting inflammatory responses and impairing tissue regeneration (Meiners et al., 2015; Schneider et al., 2021). Interestingly, the prevalence of CLDs such as COPD and IPF dramatically increases with age, and hallmarks of aging, such as cellular senescence have been shown to be increased in both, suggesting age-related mechanisms underlying the pathogenesis of these CLDs (Aghali et al., 2022; Ptasiński et al., 2021).

1.5.1 Idiopathic Pulmonary Fibrosis

Pulmonary fibrosis is a destructive process characterized by an excessive extracellular matrix (ECM) accumulation and structural changes that finally lead to organ dysfunction (Beach et al., 2017). Pulmonary fibrosis can initiate as a response after occupational or accidental exposure to toxic exogenous agents like pollutants or chemicals. Moreover, can also occur after clinical interventions like radiotherapy or chemotherapy (Beach et al., 2017). Certain gene mutations (surfactant protein C (SFTPC) or telomerase reverse transcriptase (Tert)) have been also linked to familial cases of pulmonary fibrosis (Beach et al., 2017). IPF is a chronic, progressive, and irreversible type of pulmonary fibrosis of unknown etiology (Du et al., 2022; Zheng et al., 2022). IPF affects mainly the elderly population,

with an incidence of around 3-9/100.000 cases per year in North America and Europe, and a median survival of 2-5 years after diagnosis (Du et al., 2022; Ptasiński et al., 2021; Zheng et al., 2022).

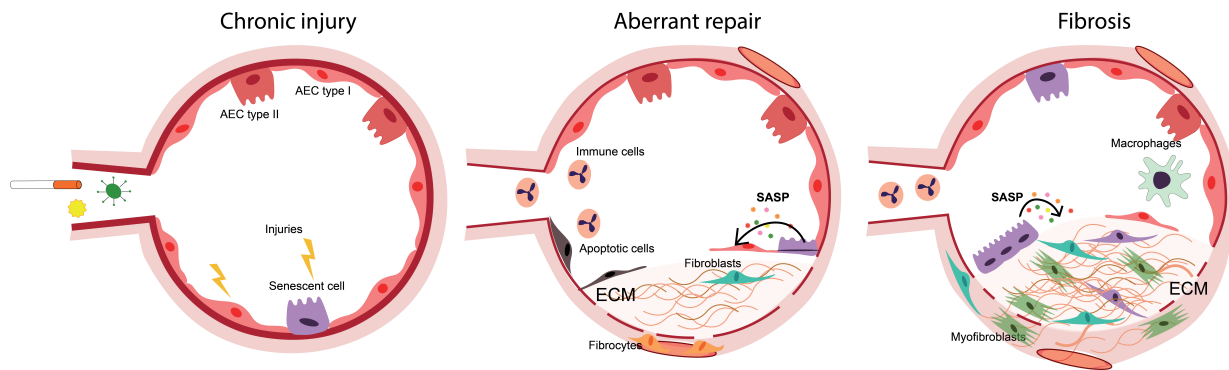


Figure 1.3: Pathogenesis of pulmonary fibrosis. Chronic exposure to injuries of the alveolar epithelium induces apoptosis and senescence of AT2 cells. These cells secrete growth factors and pro-inflammatory cytokines (SASP) that promote the recruitment of immune cells and fibrocytes as well as the activation of fibroblasts to myofibroblasts. These aSMA+ myofibroblasts favor ECM accumulation, finally leading to the lung scarring and organ dysfunction observed in IPF.

Two novel drugs, nintedanib and pirfenidone (Glass et al., 2022; King et al., 2014; Richeldi et al., 2014), have been approved by the U.S. Food and Drug Administration (FDA) for IPF treatment. Pirfenidone is an oral derivative of pyridone that has shown anti-inflammatory, antioxidant, and anti-fibrotic effects retarding disease progression (Aimo et al., 2022; Ruwanpura et al., 2020; Taniguchi et al., 2010). On the other hand, nintedanib is a tyrosine kinase and a platelet-derived growth factor receptor (PDGFR-AB) inhibitor (Wollin et al., 2015) that also has been shown to reduce the lung function decline in IPF (Wollin et al., 2015). However, these two drugs only slow down disease progression and have significant adverse effects, leaving lung transplantation as the only effective cure (Glass et al., 2022; Mei et al., 2022; Ptasiński et al., 2021). Unfortunately, the restrictive supply of organ donors and the limitations linked to organ rejection difficult the patient's access to this therapeutical intervention (Mei et al., 2022).

The histopathology of IPF is characterized by excessive scarring of lung tissue associated with declining lung function (Raghu et al., 2018). Accordingly, IPF lungs present the typical pattern of interstitial pneumonia characterized by patchy dense fibrosis along with honeycomb cysts (Tanabe et al., 2020). On the molecular level, IPF patients display aberrant recapitulation of several developmental pathways like TGF- β 1-, Wnt-, hedgehog-, and Notch-signaling but the mechanism involved in the disease pathogenesis is still not

fully understood (Chanda et al., 2019). The current model proposes that chronic small injuries to the lung epithelium lead to apoptosis or senescence of the alveolar progenitor cells. These senescent cells secrete pro-inflammatory cytokines, chemokines, and growth factors (SASP), which cause activation and transdifferentiation of fibroblasts to ACTA2+ myofibroblasts. These activated myofibroblasts become apoptosis-resistant and promote the continuous accumulation of ECM in the distal lung (Cooley et al., 2023; Lehmann et al., 2018; Mei et al., 2022; Melo-Narváez et al., 2020) (Fig.1.3). Moreover, epithelial changes such as bronchiolarization of the alveoli, accumulation of hyperplastic AT2 cells, and loss of AT1 cells have been described in IPF (Ptasinski et al., 2021). In this way, loss of the alveolar epithelium and the excessive ECM deposition impairs lung repair and effective gas exchange, finally leading to organ dysfunction (Mei et al., 2022).

Homeostasis and maintenance of the distal lung epithelium are mainly supported by AT2 cells, which differentiate into AT1 cells to recover the epithelium lining after injury (Barkauskas et al., 2013; Lehmann et al., 2020; C. Yao et al., 2019). AT2 cells also produce surfactant to support alveolar structure (Barkauskas et al., 2013; Lehmann et al., 2020; C. Yao et al., 2019). However, with age and in chronic lung diseases such as IPF, both the number and the stem cell capacity of AT2 cells are reduced, hindering the regeneration and maintenance of the alveolar epithelium (Barkauskas et al., 2013; Lehmann et al., 2020; C. Yao et al., 2019). Several hallmarks of aging such as telomere attrition, oxidative stress, and cellular senescence are increased in IPF, supporting the idea of premature aging as driver of lung fibrosis (DePianto et al., 2021; Lehmann et al., 2017; Muñoz-Espín and Serrano, 2014; Ptasiński et al., 2021; Schafer et al., 2017; Sueblinvong et al., 2012).

Accordingly, a recent transcriptomic analysis showed that during aging, senescence and pro-fibrotic pathways increase in the lung and are associated with deregulation of the cellular composition (increased fibroblasts and decreased epithelial milieu), increased collagen deposition, impaired alveolar inflation, and surfactant secretion (S. Lee et al., 2021). Moreover, senescence biomarkers (*CDKN1A*/P21, *CDKN2A*/P16, SA- β -gal), and several components of the SASP) have been described to be upregulated in epithelial cells and fibroblasts of IPF lungs (Aversa et al., 2023; Ptasiński et al., 2021; Schafer et al., 2017). Interestingly, recent studies have found new epithelial cell populations that display both senescence-related markers, as well as markers involved in epithelial differentiation (Adams et al., 2020). These cells known as aberrant basaloid cells express the basal marker Keratin 17 (KRT17) along with mesenchymal genes such as alpha-1 Type I Collagen (COL1A1) or

fibronectin 1 (FN1). Moreover, they accumulate in IPF lungs, especially in close proximity to myofibroblasts foci, and secrete pro-fibrotic factors such as TGF- β 1 (Adams et al., 2020). The persistence of these aberrantly activated transitioning senescent cells has now been implicated in IPF pathogenesis. Therefore, the selective removal of these and other senescent cells that accumulate in IPF lungs has become more attractive among novel therapeutical options for IPF.

1.6 Models of pulmonary fibrosis

1.6.1 Animal models

Bleomycin-induced pulmonary fibrosis

Bleomycin is an antibiotic and chemotherapeutic agent initially used as a treatment for various cancers by inducing DNA-damage-dependent apoptosis (Adamson and Bowden, 1974; Mouratis and Aidinis, 2011). However, it was observed that the treatment had severe adverse effects such as pulmonary fibrosis. Therefore, taking advantage of bleomycin as a pneumotoxic agent, the first murine model for IPF was presented in 1974 (Adamson and Bowden, 1974). Early studies focused on describing the general changes in lung structure and function (Adamson and Bowden, 1974), whereas most recent studies have worked on understanding cellular and molecular changes after bleomycin administration (Mouratis and Aidinis, 2011; Strunz et al., 2020). Given, its reproducibility and practicality, bleomycin-induced pulmonary fibrosis is one of the most used *in vivo* models to study this disease (T. Liu et al., 2017). Despite the close resemblance of structural, functional, and cellular changes observed in IPF, the bleomycin-induced fibrosis model has some limitations. The main one is the fact that the young mice (2-3 weeks) used in this model regenerate their lungs reversing the phenotype after a few weeks, contrary to the irreversible phenotype observed in humans (Klee et al., 2023; Mouratis and Aidinis, 2011). In this regard, the model has been adapted by using older animals (Hecker et al., 2014) or repetitive exposure to bleomycin (Degryse et al., 2010), which has improved the recapitulation of the disease *in vivo*. However, the bench-to-bed translation of these models for drug discovery remains limited.

Radiation-induced pulmonary fibrosis

Pulmonary fibrosis is not only caused as a result of aging or exposure to chemo-agents but has been also described as a side-effect of radiotherapy (Beach et al., 2017; Zhou et al., 2022). Similar to the features observed for IPF, radiation-induced pulmonary fibrosis (RIPF) displays as well a progressive and irreversible ECM accumulation that destroys tissue architecture and leads to organ failure (Beach et al., 2017; Curras-Alonso et al., 2023; Zhou et al., 2022). Until now, animal models have been established to study the pathobiology of RIPF (Beach et al., 2017). Although the mechanism is not fully elucidated, it has been shown that IR induces DNA damage that initiate cell death pathways as well as chronic inflammation and cellular senescence (Beach et al., 2017). Interestingly, similar SASP components have been found for both RIPF and IPF (Beach et al., 2017). Recent efforts have been focused on finding similar dysregulated pathways in animal models of RIPF and IPF. For example, similar to what has been described for IPF, IR injures AT2 cells, which by secreting a collection of pro-inflammatory and pro-fibrotic mediators stimulate fibroblasts activation and differentiation as well as the recruitment of immune cells that promotes inflammation and tissue remodeling (Ding et al., 2013; Jin et al., 2020; Zhou et al., 2022). Therefore, it has been proposed that IR-mediated AT2 cell dysfunction is the main initiator and driver of pulmonary fibrosis in this model (Zhou et al., 2022). To date, several animals models for RIPF have been developed, for example, using whole thorax irradiation or more sophisticated techniques like intensity-modulated RT or stereotactic body radiation therapy (Jin et al., 2020). However, the pre-clinical application of this model supposed some challenges, for example, due to varying susceptibility to RIPF on different mouse strains or the long time (6-12 months) these mice need to develop the fibrotic phenotype (Jin et al., 2020). Recently, the first murine atlas of radiation-induced lung injury response was published. Here, the authors showed temporal and cell-specific changes after IR in mice helping to define the main cellular players and the pathways involved in RIPF pathogenesis (Curras-Alonso et al., 2023). However, up-to-date human translation of these findings is very limited given the lack of human specimens from RIPF patients or any translational models based on the human system.

1.6.2 Translational models

Precision-cut lung slices

Different models using human cells have been established to study lung injury and regeneration. For example, 2D monolayer culture of specific cell types or 3D liquid interface (ALI)

cultures, in which basal, club, and goblet cells are co-culture to model the airway epithelium (G. Liu et al., 2019). Moreover, 3D organ-on-a-chip models have provided platforms that recapitulate organ-specific functions such as circulation and mechanical stretching (Baptista et al., 2022; Huh et al., 2010). However, these models usually use a selection of cell types and have limitations in modeling the complex 3D structures of the human lung. Precision-cut lung slices (PCLS) from human lung resections preserve both the cellular composition as well as the lung structure, mimicking closer the cellular environment *in vivo* (Gerckens et al., 2019; Lang et al., 2022). For this, fresh lung tissue is filled with a solution of low-melting point agarose through the airways and cut into 500 μ m slices for their submerged culture (Gerckens et al., 2019; G. Liu et al., 2019). hPCLS can have been used to study molecular mechanisms involved in pulmonary fibrosis such as the Wnt-signalling pathway in tissue repair (Alsafadi et al., 2017; Uhl et al., 2015) or for pre-clinical testing of potential drugs for IPF (Alsafadi et al., 2017; Mercer et al., 2016). In this way, hPCLS were used to establish a model of early fibrotic changes by exposing them to a combination of cytokines and growth factors (TNF-a, platelet-derived growth factor (PDGF-AB), lipoprotein A (LPA), and TGF- β 1) known as the fibrotic cocktail (Alsafadi et al., 2017; Lang et al., 2022). Here, they found upregulation of well-known fibrotic markers as well as epithelial reprogramming as described in the human disease (Alsafadi et al., 2017). Importantly, hPCLS also retain patient heterogeneity, which might facilitate the discovery of drugs with consistent and broad efficiency. Finally, successful studies showing reduced fibrotic burden in hPCLS from different origins after treatment with anti-fibrotic drugs (Gerckens et al., 2021; Hesse et al., 2022; B.-W. Huang and Gao, 2018) or with senolytics (Lehmann et al., 2017) position hPCLS as an attractive model for drug discovery and efficacy testing of novel compounds for IPF therapy.

1.7 Targeting Cellular senescence: Senolytics

Cellular senescence has both beneficial and detrimental consequences on health and disease (Chaib et al., 2022). In the case of IPF, senescence has been linked to impaired regenerative potential of the alveolar epithelium associated with its pathobiology (Aversa et al., 2023; Lehmann et al., 2017; Schafer et al., 2017). Recent studies have demonstrated that the selective removal of senescent cells in aged animals using, for example, a suicide gene-based system (Baker et al., 2011) or small molecules, known as senolytics (Schafer et al., 2017), increased life span and improves lung function (Baker et al., 2011; Schafer et al., 2017; Zhu

et al., 2015). Moreover, senolytics reduced pro-inflammatory and pro-fibrotic markers ex vivo, in fibrotic hPCLS (Lehmann et al., 2017; Schafer et al., 2017) and *in vivo*, in both animal models of pulmonary fibrosis (Verma et al., 2013) as well as in IPF patients (Veith et al., 2017). Currently, most of the senolytics are FDA-approved compounds with oral administration that have been repurposed as anti-aging drugs (Chaib et al., 2022). Their mode of action is based on the elimination of cells that activate senescent anti-apoptotic pathways (SAPs), which are known to be upregulated in senescent cells. Similar to some cancer types, the upregulation of SAPs allows senescent cells to evade apoptosis-mediated cell death (Chaib et al., 2022). For this reason, the current drugs target one or several of these pathways to selectively deplete senescent cells (Chaib et al., 2022). In this way, from the initially 46 discovered compounds, two were selected and have been tested for safety and efficacy: Dasatinib (D) and Quercetin (Q) (Chaib et al., 2022). Moreover, small molecules targeting the B-cell lymphoma 2 (BCL-2)-dependent anti-apoptotic pathways have been used to target senescent cells (Zhu et al., 2016).

1.7.1 Dasatinib + Quercetin

The first two senolytics, DQ, were discovered in 2015 using a hypothesis-driven drug discovery approach. Here, the authors found a synergistic senolytic effect of these two compounds after treating aged mice (Zhu et al., 2015). Moreover, experiments using different cell types *in vitro* showed that DQ treatment leads to apoptosis only in senescent cells and not in proliferating or quiescent cells (Aghali et al., 2022; Zhu et al., 2015).

Quercetin is a plant-derived flavonoid that has been found to inhibit multiple SAPs-related proteins such as phosphoinositide 3-kinase (PI3K)-protein kinase B (AKT) and BCL-2 (Chaib et al., 2022; Zhu et al., 2015). In the lung, it has been shown that treatment with Quercetin alone improves lung function and reduces inflammation and fibrotic burden in bleomycin-induced fibrosis (Boots et al., 2020; Sellarés and Rojas, 2019; Verma et al., 2013) as well as in IPF patients (Veith et al., 2017). On the other hand, dasatinib was initially developed as chemotherapy for myeloid leukemias, given its ability to block the oncoprotein BCR-ABL1 responsible for this pathology (Takekoshi et al., 2020). On top of this, dasatinib inhibits Src kinases, which are known to promote cell survival in tumor and senescent cells (Belsches-Jablonski et al., 2001). Animal studies have demonstrated that removal of senescent cells by DQ combined treatment alleviates age-related alterations (diabetes, cardiac and neural dysfunction, cancer, etc.) and even increases the lifespan of

aged mice (Justice et al., 2019; Kirkland and Tchkonia, 2020). Moreover, DQ-dependent removal of senescent cells in bleomycin-treated mice restores lung function, confirming the role of senescent cells in the pathogenesis of pulmonary fibrosis. First clinical trials to study DQ feasibility, safety, and efficacy for IPF patients have recently started (Justice et al., 2019; Nambiar et al., 2023). These trials provided initial indications that intermittent treatment with DQ is well tolerated and might reduce disease burden in IPF (Justice et al., 2019; Nambiar et al., 2023). However, it is important to consider that treatment with dasatinib alone has been linked to rare pulmonary side effects such as pleural effusion, interstitial pneumonia, and pulmonary hypertension (Weatherald et al., 2020). Therefore, adjustment of doses and treatment regimes might be needed to implement DQ as a standard treatment for pulmonary fibrosis.

1.7.2 ABT-263: Navitoclax

The anti-apoptotic BCL-2 proteins family was found to be upregulated in radiation-induced senescence (Zhu et al., 2015). Therefore, it has also been used as a target to selectively kill senescent cells. The first report by Zhu et al., 2015 showed that the knockdown of B-cell lymphoma-extra large (Bcl-xL) was effective to kill senescent human umbilical vein endothelial cell (HUVECs) but not preadipocytes (Zhu et al., 2016). Suggesting that the upregulation of anti-apoptotic signaling pathways might be cell type-specific response. One year after, the same authors demonstrated that the drug ABT-263 is senolytic in HUVECs and human fetal lung fibroblasts (IMR90) cells (Zhu et al., 2016). ABT-263 is a small molecule inhibitor that was developed as a chemotherapeutic agent for the treatment of lung cancer and lymphoid malignancies (Zhu et al., 2016). This molecule inhibits the activity of the anti-apoptotic proteins: BCL-2, Bcl-xL, and bcl-2-like protein 2 (Bcl-w) (Vogler et al., 2009). These proteins bind to the BCL2-like protein 4 (Bax)/BCL2 Antagonist/Killer (Bak) complex on the mitochondrial membrane, inhibiting the activation of caspase-mediated apoptosis (Zhu et al., 2016). Recent studies have demonstrated beneficial effects of ABT-263 treatment for pulmonary fibrosis as shown by attenuation of bleomycin-induced fibrosis in mice (Cooley et al., 2023; S.-H. Kim et al., 2021; Pan et al., 2017). However, similar to other senolytics, the susceptibility to this drug is cell type dependent, and therefore, the combination with other agents might be useful to target a higher percentage of senescent cells and have a bigger therapeutic effect.

1.8 Hypothesis and objectives



Figure 1.4: Hypothesis and Milestones. The aim of this doctoral thesis was to establish an aging model in human PCLS by exposing them to IR. Then, markers of accelerated aging and fibrosis were determined. Using this model, I expected to increase our understanding of the molecular mechanism behind aging-related fibrotic processes, discover novel biomarkers, and use it for pre-clinical testing of currently available drugs.

Aging is a natural process that leads to reduced organ function and regeneration capacity. Therefore, aging is the main risk factor for chronic lung diseases such as IPF. Although the pathogenesis of IPF remains to be fully elucidated, it has been linked to repetitive injury and aberrant activation of AT2 cells, which promote fibroblasts activation and increased accumulation of ECM. Moreover, several hallmarks of aging such as telomere attrition, increased cellular senescence, oxidative stress, and apoptosis have been described in fibrotic lungs from both human and mice, supporting the role of premature aging in fibrosis development. Different ex vivo models such as precision-cut lung slices (PCLS) derived from bleomycin-treated mice or IPF patients have provided insight into IPF pathobiology. PCLS closely mimic the cellular diversity of the lung and preserve lung architecture. Moreover, they can be obtained from patients, reducing the number of animals needed for experimentation. However, currently available models use PCLS obtained from relatively young mice or end-stage IPF patients, reducing the clinical translation of these findings to the long-term established fibrotic disease in humans. In this way, novel relevant models to study the role of aging in pulmonary fibrosis are still missing. Therefore, I hypothesized that “Inducing cellular senescence by ionizing radiation drives pro-fibrotic hallmarks in human PCLS that will allow the discovery of novel biomarkers and preclinical testing of senotherapies” (Fig.1.4). To this end, my doctoral thesis had the following milestones:

1. Development of an ex vivo model to study the role of cellular senescence in pulmonary fibrosis.
2. Identification of novel secreted factors as potential biomarkers of senescence-mediated

fibrotic changes in the lung.

3. Pre-clinical testing of senolytic drugs to target senescence-induced pro-fibrotic changes.

Chapter 2

Materials

2.1 Human material

Tumor-free lung tissue from lung cancer resections of patients without an IPF/ILD diagnosis (determined by CT and pathology) was used to generate hPCLS. Human tissue was obtained from the CPC-M bioArchive at the Comprehensive Pneumology Center (CPC Munich, Germany). The study was approved by the local ethics committee of the Ludwig-Maximilians University of Munich, Germany (Ethic vote 19-630). Written informed consent was obtained for all study participants. Lung tissue was obtained for patients with a mean age of 65 years, diagnoses and smoking history are listed in Table 2.1. BALF samples were obtained from age matched control and IPF patients (Table 2.2).

Table 2.1: Patient information from tissues used for PCLS generation.

Diagnose	Age	Smoking status	FEV1%FVC
Lung Cancer	57	smoker	76,61
Lung Cancer	66	ex-smoker	87,52
Lung Cancer	69	ex-smoker	82,29
Lung Cancer	65	ex-smoker	76,62
Lung Cancer	77	smoker	65,69
Lung Cancer	73	smoker	75,79
Lung Cancer	67	ex-smoker	72,29
Lung Cancer	78	non-smoker	81,82

Diagnose	Age	Smoking status	FEV1%FVC
Lung Cancer	21	NA	NA
Lung Cancer	71	ex-smoker	73,29
Lung Cancer	62	non-smoker	77,16
Lung Cancer	75		80,06
Lung Cancer	65	ex-smoker	79,39
Lung Cancer	67	ex-smoker	76,79
Lung Cancer	59	smoker	75,39
Lung Cancer	71	smoker	66,96
Lung Cancer	72	smoker	68,29
Lung Cancer	57	smoker	82,08
Lung Cancer	50	smoker	72,41
Lung Cancer	52	smoker	68,81
Lung Cancer	62	non-smoker	74,87
Lung Cancer	72	ex-smoker	NA
Lung Cancer	77	non-smoker	87,86
Lung Cancer	78	smoker	76,51
Lung Cancer	73	smoker	65,77
Lung Cancer	55	ex-smoker	88,22
Lung Cancer	46	ex-smoker	81,89
Lung Cancer	57	ex-smoker	66,73
Lung Cancer	60	ex-smoker	79,47
Lung Cancer	75	non-smoker	73,26
Lung Cancer	60	smoker	71,04
Lung Cancer	64	smoker	68,71
Lung Cancer	62	ex-smoker	76,28
Lung Cancer	81	ex-smoker	60,41
Lung Cancer	64	ex-smoker	78,79
Lung Cancer	70	NA	NA
Lung Cancer	58	smoker	74,78
Lung Cancer	66	smoker	65,81
Lung Cancer	63	smoker	59,42
Lung Cancer	80	ex-smoker	77,16

Diagnose	Age	Smoking status	FEV1%FVC
Lung Cancer	65	smoker	80,89
Lung Cancer	70	NA	NA
Lung Cancer	62	non-smoker	68,45
Lung Cancer	85	ex-smoker	68,81
Lung Cancer	63	ex-smoker	77
Lung Cancer	70	smoker	78,92
Lung Cancer	74	non-smoker	76,01
Lung Cancer	67	ex-smoker	70,32
Lung Cancer	65	smoker	76,14
Lung Cancer	77	non-smoker	90,25
Lung Cancer	67	ex-smoker	80,63

Table 2.2: Patient information from Bronchoalveolar lavage fluid samples.

Diagnose	Age	Sex	Smoking status
IPF	75	male	ex-smoker
IPF	74	male	ex-smoker
IPF	66	male	ex-smoker
IPF-UIP	68	male	NA
IPF-UIP	74	male	non-smoker
Bronchitis	68	male	ex-smoker
Chronic cough	71	female	non-smoker
Bronchitis	37	male	smoker
Postinfection cough	59	male	non-smoker
Chronic cough	65	female	non-smoker

2.2 Animal experiments

Pathogen-free female C57BL/6 mice (6–8 wk. old) were purchased from Charles River and used to obtain murine Precision-cut lung slices (mPCLS). Mice were housed with constant humidity and temperature with 12 h light cycles and had free access to water and food. Mice were euthanized by an overdose of narcotics and lungs were perfused with 1X PBS, filled with 2% of low gelling temperature agarose in DMEM-F12 (Thermo Scientific, USA), harvested and kept at 4°C until use.

2.3 Primary human and mouse cells

Primary human fibroblasts (passages lower than 9) used for organoid assays or 2D culture experiments obtained from the CPC-M bioArchive at the Comprehensive Pneumology Center (CPC Munich, Germany) and are listed in table 2.3. phLF were cultured in DMEM-F12 supplemented with 10% fetal calf serum (FCS) and 1% penicillin/streptomycin at 37°C, 5% CO₂ for maintenance and expansion.

primary murine AT2 cells (pmAT2) cells were freshly isolated. For this, mouse lungs were flushed with DPBS and digested with Dispase for 45 min at RT. Tissue was minced and single-cell suspension was sequentially filtered with 100 µm and 20 µm nylon filters. Fibroblasts were depleted by adhesion to Petri dishes after 30 min incubation at 37°C, 5% CO₂. Floating cells were spun down (200 RCF for 10 min, 15°C), resuspended in MACS cold buffer, and counted. Then, cells were resuspended in 90 µl of MACS Buffer per 10⁷total cells, and 10 µl of murine epithelial cell adhesion molecule (EpCAM) MicroBeads per 10⁷ total cells were added. Cells were incubated at 4°C for 20min and MACS sorter was used to enrich EpCAM+ cells. Finally, pmAT2 were cultured in DMEM-F12 supplemented with Glucose (3.6mg/ml), 2% GlutaMAX, 10mM HEPES, and 1% penicillin/streptomycin.

Table 2.3: Patient data from primary human fibroblasts used in this study.

Sex	Age	FEV1%FVC	Smoking status	Diagnose
Female	72	normal	ex-smoker	Lungcancer
Female	67	NA	smoker	Lungcancer
Male	84	NA	ex-smoker	Lungcancer
Female	56	>80%/97	ex-smoker	IPF

2.4 Primers

Table 2.4: Primers used for expression analysis by RT-qPCR.

Gene	Sequence
mHPRT fw	CCTAAGATGAGCGCAAGTTGAA
mHPRT rv	CCACAGGACTAGAACACACCTGCTAA
mp21_fw_1	ACATCTCAGGGCCGAAAACG
mp21_rev_1	AAGACACACAGAGTGAGGGC
mp16_fw_1	CGGGGACATCAAGACATCGT
mp16_rev_1	GCCGGATTAGCTCTGCTCT
mActin-fw	CTG GGC CGC CCT AGG CAC CA
mActin-rv	TGG CCT TAG GGT TCA GGG
hHPRT_fw	AAGGACCCCACGAAGTGTG
hHPRT_rv	GGCTTGTATTTGCTTTCCA
hp16_fw_1	ACCAGAGGCAGTAACCATGC
hp16_rev_1	CCTGTAGGACCTTCGGTGAC
hp21_fw_2	GTCAGTTCTGTGGAGCCG
hp21_rev_2	TGGGTTCTGACGGACATCCC
hPai1 fw	GACATCCTGGAACTGCCCTA
hPai1 rv	GGTCATGTTGCCTTCAGT
hcol1a1_fw	CAAGAGGAAGGCCAAGTCGAG
hcol1a1_fw	CAAGAGGAAGGCCAAGTCGAG
hcol1a1_rv	TTGTCGCAGACGCAGATCC
hCol3a1_fw	CGCTCTGCTTCATCCACTAT
hCol3a1_rv	CGGATCCTGAGTCACAGACAC
hFn1_fw	CCGACCAGAAGTTGGTTCT
hFn1_rv	CAATGCGGTACATGACCCCT
hActa2_fw	CGAGATCTCACTGACTACCTCATGA
hActa2_rv	AGAGCTACATAACACAGTTCTCCTTGA
hCripto1 FW	CTTCAGAGATGACAGCATTGG
hCripto1 RV	CAGCAGGTTCTGTTAGCTCCT
hGdf15-FW-2	TACTCACGCCAGAAGTGCAG
hGdf15-RV-2	TCACGTCCCACGACCTTGAC

2.5 Reagents

Table 2.5: Laboratory reagents.

Name	Company	ID	Application
DPBS 1X	Gibco	14190-094	Cell culture
AutoMACS Rinsing solution	Miltenyi Biotec	130-091-222	Cell culture
DMEM/F-12-500 mL	Life Technologies GmbH	11320074	Cell culture
Metformin hydrochloride	R&D/BIO-TECHNE	2864	Cell culture
Trypsin 0.25% EDTA	ThermoScientific	5001213	Cell culture
Pen-Strep (10.000U/ml) 100ml	LIFE TECHNOLOGIES	15140122	Cell culture
Matrigel	Sigma	11523550	Cell culture
Pituitary extract bovine sterile	Sigma	P1167-5MG	Cell culture
SPiDER-BGal	Dojindo	SG02-10	Cell culture
CD45 MicroBeads. human	Miltenyi Biotec	130-045-801	Cell culture
Quercetin. =95% (HPLC). Solid	Sigma-Aldrich Chemie GmbH	Q4951-10G	Cell culture
Dasatinib (BMS-354825)	BIOZOL Diagnostica Vertrieb GmbH	SEL-S1021-25MG	Cell culture
ABT-263	BIOMOL GMBH	Cay11500-10	Cell culture
Metformin hydrochloride	R&D/BIO-TECHNE	2864	Cell culture
FBS Good	PAN Biotech	P40-37500	Cell culture
Insulin-Transferrin-Selenium-Sodium Pyruvate	Life Technologies GmbH	51300044	Cell culture
MACS BSA Stock Solution	Miltenyi Biotec	130-091-376	Cell culture
Amphotericin B	Sigma	A2942-100ML	Cell culture
Retionic acid	Sigma	R2625-5G	Cell culture

2. Materials

25

Name	Company	ID	Application
Hoechst 33342 Solution (20 mM)-5 mL	ThermoScientific	62249	Cell culture
Cholera Toxin Vibrio Cholerae	Sigma	C8052-.5MG	Cell culture
Epidermal Growth Factor	Sigma	SRP3196-500UG	Cell culture
Sodium Pyruvate Solution	Sigma	S8636-100ML	Cell culture
GlutaMAX Supplement-100	Life	35050038	Cell culture
Dimethyl Sulfoxide (DMSO), cell culture	Santa CruzBiotechnology	sc-358801	Cell culture
HEPES solution bioxtra, 1 M, PH 7.0-7.6	Sigma	D69H0887-100ML	Cell culture
CD326 (EpCAM) MicroBeads, human	Miltenyi Biotec	130-061-101	Cell culture
Agarose low gelling temperature	Sigma	A9414-250G	Cell culture
Triton X-100	Applichem	A1388,1000	Cell culture
reagent diluent concentrate 1	R&D	DY997	ELISA
DAPI 1mg/ml	ThermoScientific	62248	Immunofluorescence
Dako Fluorescent Mounting Medium	DAKO	S3023	Immunofluorescence
Bovine Serum Albumin	Sigma	A7906-100G	Immunofluorescence
Dako antibody diluent	Agilent Technologies	S3022	Immunofluorescence
Vector True View autofluorescence quencher	VectorLabs	SP8400	Immunofluorescence
RotiCell 10X PBS	Carl Roth	9150.1	Immunofluorescence
Methanol min. 99,9 %,	carl Roth	4627.5	Immunofluorescence

Name	Company	ID	Application
Normal Goat Serum50ML	ABCAM	ab7481	Immunofluorescence
Paraformaldehyde solution 4% in PBS	santa cruz	sc-281692	Immunofluorescence
Tween 20, research grade, 500 ml	VWR International	ICNA11TWEEN201	Molecular biology
RNase free water	Sigma	W4502-1L	Molecular biology
Ethanol absolute	Applichem	A1613,1000PE	Molecular biology
Rnase free Dnase Set	QIAGEN	79254	Molecular biology
Trizol reagent	ambion	15596018	Molecular biology
Random Hexamers (50 uM)-5 nmol	Life Technologies GmbH	N8080127	Molecular biology
LightCycler SYBR Green Master	ROCHE	4887352001	Molecular biology
M-MLV Reverse Transcriptase Buffer-1 mL (DTT + 5x)	Life	18057018	Molecular biology

2.6 Commercial kits

Table 2.6: Commercial kits.

Name	Company	ID	Application
DuoSet hCripto1	R&D	DY145	ELISA
DuoSet hMMP3	R&D	DY513	ELISA
DuoSet hTGF β 1	R&D	DY240	ELISA
DuoSet Ancillary Kit 2	R&D	DY008B	ELISA
StopSolution pack	R&D	DY994	ELISA
Substrate Reagent Pack	R&D	DY999	ELISA
DuoSet hIL-6	R&D	DY206	ELISA
DuoSet hPAI-1	R&D	DY1786	ELISA
DuoSet hGDF-15	R&D	DY957	ELISA

Name	Company	ID	Application
LDH cytotoxicity WST assay	ENZO	ENZ-KIT157-0500	LDH
Pierce BCA protein Assay Kit	ThermoScientific	23227	protein quantification
PeqGold Total RNA kit	VWR	13-6834-02	RNA isolation cells
Rneasy Plus Micro kit 50	QIAGEN	74034	RNA isolation from PCLS
RNA 6000 Nano Kit	Agilent	5067-1511	RNA quantification
hXL Cytokine Array Kit	Bio techne	ARY022B	Secretome

2.7 Enzymes and proteins

Table 2.7: Enzymes and recombinant proteins.

Name	Company	ID	Application
rhCripto-1; 10 µg	Bio-Techne GmbH	145-CR-010	cell culture
Dispase, 100mL	TH. GEYER	7662350	cell culture
Collagenase/Dispase 100mg	Sigma/Roche	10269638001	cell culture
Mitomycin C	Sigma	M4287-2MG	cell culture
DNase I	AppliChem	A3778,0100	cell culture
Bafilomycin A1	BIOMOL GMBH	Cay11038-1	cell culture
RNase Inhibitor	Life Technologies GmbH	N8080119	molecular biology
M-MLV Reverse Transcriptase Buffer-1 mL	Life Technologies GmbH	18057018	molecular biology

2.8 Consumables

Table 2.8: Laboratory Consumables.

Name	Company	ID
SafeSeal Tips Professional 200 µl. Steril	Biozym Scientific GmbH	770200
Safe-Lock PCR CLEAN 1.5 farblos (1000 Stk)	VWR INTERNATIONAL	211-2164
Amicon Ultra 3K-0.5mL centrifugal filter	Millipore	Z740169
Cell strainer 40um nylon	Falcon	352340
Cell strainer 100um nylon	Falcon	352360
Surgical drape	Foliodrape	277500
30ml syringe luer-lock	BD	302832
5ml syringe luer-lock	HENKE SASS WOLF	5050-0000V0
IV Cannula 20G x 1 1/4"	VasoVet	4269115
Filter paper embedding	Medite	
Biopsy embedding cassettes	Carl Roth	
PCR 96-Well TW-MT-Platte. weiß. Packung à 25 Stück	Biozym Scientific GmbH	712282
Nalgene™ Rapid-Flow™ Sterile Top bottle filter	ThermoScientific	10300461
Midisart BV 0.2um 12pc Midisart BV	Neolab Migge GmbH	17805BVE
Stainless Steel Beads, 5 mm (200)	qiagen	69989
Zählkammern, Neubauer	Hirschmann	8100103
50 stainless steel blades	Campden Instruments	7550/1/SS
96 Well Plate Imaging	VWR	NUNC165305
Safe-Lock Tubes, 2,0 mL, PCR clean, farblos, 1.000 Tubes	Eppendorf	30123344
Safe-Lock PCR CLEAN 0.5.	VWR INTERNATIONAL	211-2163
Plates for immunoassays-ELISA	Kisker Biotech	5513
BP LOCTITE® 406 Sekundenkleber	conrad	220783

Name	Company	ID
Disposable Biopsy Punch 4mm	abcam	48401
X72 Slide Superfrost Plus Blue	ThermoScientific	11950657

2.9 Laboratory equipment

Table 2.9: Laboratory equipment.

Name	Company
Bioanalyzer 2100	Agilent
LSRII FACS	BD
FACS AriaII	BD
Decloaking chamber DC2002	Biocare medical
ChemiDoc XRS+ Gel imaging system	Biorad
Vibratome 7000smz2	Campden Instruments
vortex mixer	Corning
Mini microcentrifuge	Corning
Magnetic stirrer	Corning
Centrifuge 5424R	Eppendorf
Thermomixer comfort	Eppendorf
MiniSpin	Eppendorf
Multipipette E3	Eppendorf
Mastercycler nexus	Eppendorf
Centrifuge 5430	Eppendorf
Paraffin streckbad GFL1052	GFL
Shaker duomax103	Heidolph
Microcentrifuge 200R	Hettich
Centrifuge Rotina 420R	Hettich
Waterbath Aqualine AL12	LAUDA
-20°C freezer	LIEBHERR medline
4°C fridge	LIEBHERR medline
Vortexer IKA MS3	Marschall Scientific
Heating plate	MEDAX

Name	Company
Cooling plate COP30	Medite
Hyrax CU65	MICROM GmbH
Nanodrop1000	PeqLab
Tissue Lyser II	Qiagen
Light Cycler LC480II	Roche Diagnostics
Photometer Sunrise	TECAN
HERASAFE KS180	ThermoScientific
Microm STP 420D Tissue processor	ThermoScientific
Microm EC 350-1 Paraffin embedding system	ThermoScientific
Heracus Incubator	ThermoScientific
Alladin Syringe Pump	WPI
pHmeter 720	WTW
Axiovert 40C	Zeiss
Hyrax V50	Zeiss
PrimoVert	Zeiss
Hyrax M55	Zeiss
AxioImager.M2	Zeiss
LSM710	Zeiss
LifeCellImager Observer.Z1	Zeiss

2.10 Software

Table 2.10: Software.

Name	Company
Magellan 7.2	Tecan
ImageLab	Bio-Rad
FlowJo 10.8	BD Biosciences
Zen 2 Blue	Zeiss
Fiji ImageJ 1.53	NIH
R 4.3	R Foundation
R Studio 4.3	R Foundation
Visual Studio Code	Microsoft
Affinity Designer 2	Serif

Name	Company
Python 3.9	Python
Adobe Illustrator 2023	Adobe Inc
Zotero	Center for History and New Media George Mason University
Microsoft Office	Microsoft
Biorender	BioRender
Organoid-Counter	AI HMGU

2.11 Antibodies

Table 2.11: Primary antibodies used for immunofluorescence.

Protein	ID	Host	Reactivity	Dilution	samples
ACT	ab24610	mouse	mouse	200	organoids
aSMA	A5228	mouse	human, mouse	1000	FFPE
CC3	9661	rabbit	human, mouse	150	FFPE
CD45	LS-B14248	goat	human	300	FFPE
Col3a1	600-401- 105-0.1	rabbit	human	400	FFPE
Cripto1	NB100- 1598	rabbit	human, mouse	800	FFPE
Krt8	TROMAI	rat	human, mouse	200	FFPE
LAMP3	DDX0191- P	rat	human	100	FFPE
P19	ab26696	rat	mouse	200	FFPE
P21	ab109520	rabbit	human	100/100	FFPE/organoids
P21	ab188224	rabbit	mouse	800/200	FFPE/organoids
PDPN	AF3244	goat	mouse	200/50	FFPE/organoids
PDPN	AF3670	sheep	human	200	FFPE
ProSP-C	sc-518029	mouse	human	50	FFPE
ProSP-C	ab3786	rabbit	mouse	200	FFPE/organoids
SFTPC	HPA010928	rabbit	human	100	FFPE

Protein	ID	Host	Reactivity	Dilution	samples
SPRR1A	ab125374	rabbit	human, mouse	100	FFPE
yH2Ax	05-636	mouse	human, mouse	200	FFPE/organoids

Table 2.12: Secondary antibodies used for immunofluorescence.

Name	ID	Host	Reactivity	Dilution	samples
AF-568	A10042	donkey	rabbit	250/500	FFPE/Organoids
AF-647	A31573	donkey	rabbit	250/500	FFPE/Organoids
AF-488	A21206	donkey	rabbit	250/500	FFPE/Organoids
AF-647	A21447	donkey	goat	250/500	FFPE/Organoids
AF-568	A21099	donkey	sheep	250/500	FFPE/Organoids
AF-647	A21448	donkey	sheep	250/500	FFPE/Organoids
AF-488	A21208	donkey	rat	250/500	FFPE/Organoids
AF-488	A21202	donkey	mouse	250/500	FFPE/Organoids
AF-568	A10037	donkey	mouse	250/500	FFPE/Organoids
AF-647	A31571	donkey	mouse	250/500	FFPE/Organoids

Chapter 3

Methods

3.1 Precision-Cut lung slices

Precision-cut lung slices were obtained either from murine lungs (mPCLS) or tissue explants from donors (hPCLS) using either a vibratome HyraxV50 (Zeiss, Germany) or 7000smz-2 Vibratome (Campden Instruments, England) as previously described (Lehmann et al., 2018; Uhl et al., 2015). 300 μm slices were obtained from murine lungs pre-filled with agarose. Human lung tissue was filled with 3% of low gelling temperature agarose in DMEM-F12 (Thermo Scientific, USA) and kept at 4°C overnight before slicing the tissue into 500 μm slices. Depending on the down-stream analysis the slices were cultured either as whole slices in 12-well plates or as 4mm punches in 96-well plates. Both mPCLS and hPCLS were cultured for up to 9 dpi in DMEM-F12 supplemented with 0.1% FCS, 1% penicillin/streptomycin and 1% amphotericin B as described before (Lehmann et al., 2018; Uhl et al., 2015) and the medium was changed every 48/72 hours.

3.2 Ionizing radiation exposure

One day after generating the PCLS, the medium was changed. Then, an RS225 X-ray cabinet (Xstrahl, Camberley, UK) was used to expose PCLS to different doses of ionizing radiation according to the settings shown in Table 3.1. IR-PCLS were kept in culture at 37°C, 5% CO₂ until use.

Table 3.1: Ionizing radiation doses used for radiation of PCLS. Doses were calculated from exposure times at 195kV and 15mA.

Dose (Gy)	Time
30	12 min 24 sec
60	24 min 48 sec
120	49 min 35 sec

3.3 WST-1 assay

4mm punches were prepared from mPCLS and hPCLS, plated in triplicates and irradiated after 24 hours. On collection day (1, 3/4, or 7 dpi) lysis control punches were incubated with 0.1%Triton-X 100 in culture medium for 1 hour at 37°C. Then, all punches were transferred to a new 96-well plate containing 100 μ l of pre-warmed PCLS culture medium per well. Only medium was used as background control. Then, 10 μ l of the WST-1 Assay Reagent (Abcam, UK) were added per well and punches were incubated for 1h at 37°C. Finally, absorbance was measured at 450 nm (reference wavelength 690nm) by a microplate reader Tecan Sunrise (Tecan GmbH, Germany). Absorbance values were then calculated by subtracting the background signal.

3.4 LDH assay

4mm punches were prepared from mPCLS and hPCLS, plated in triplicates and irradiated after 24 hours. 24 hours before the collection day, the medium was changed using 200 μ l per well. The next day, (1, 3/4, or 7 dpi) lysis control punches were incubated with lysis solution (1:10 dilution in culture medium) for 30 minutes at 37°C. Then, supernatants (100 μ l) were transferred to a new 96-well plate, LDH working solution (100 μ l) was added to each well and the plate was incubated in a dark place for 30 min at room temperature. Only medium was used as background control. Finally, absorbance was measured at 450 nm (reference wavelength 690nm) by a microplate reader Tecan Sunrise (Tecan GmbH, Germany). Absorbance values were then calculated by subtracting the background signal.

3.5 Senescence-Associated β -Galactosidase on fresh tissue

Fresh punches were stained 7 at dpi. For this, punches were washed once with 1X PBS and then, incubated with BafA1 (100 nM) in culture medium for 1h at 37°C, 5%CO₂. Then, the SPiDER- β -gal working solution was freshly prepared by diluting BafA1 (0.1mM in DMSO) and SPiDER β -gal

(1mM in DMSO) stock solutions in PCLS medium to working concentrations: 100nM and 20uM, respectively. The SPiDER β -gal staining solution was then added to each well and punches were incubated at 37°C, 5%CO₂ for 30 min. Punches were washed once with 1X PBS and counter-stained with Hoechst dye in 1X PBS (1:500) for 10-15 min at room temperature. Finally, punches were washed with 1X PBS and imaged directly using an LSM710 Confocal microscope (Zeiss, Germany). mean fluorescence intensity (MFI) of both channels was quantified using ImageJ and the MFI from SPiDER β -gal was normalized to the nuclear signal.

3.6 RNA isolation from PCLS

For RNA isolation we adapted the protocol previously published (Stegmayr et al., 2021). In summary, six 4mm mPCLS or hPCLS were washed once with 1XPBS and directly snap frozen in liquid N₂ in 2ml safe-lock Eppendorf tubes. On the isolation day, 400 μ l of TRIzolTM and one 5 mm stainless steel bead (Qiagen, USA) were added to each sample. Then, tissue was homogenized using a TissueLyser II (Qiagen, USA) 3 times at 27Hz for 1 min. Homogenates were transferred to a new 1.5 ml RNAse-free eppendorf tube. RNA was precipitated using 100% EtOH, loaded in RNeasy MinElutSpin columns, and spun down at full speed (16,000 x g/RFC) for 30 s at RT. Samples were washed once with RW1 buffer and treated with DNaseI diluted in RDD, according to the manufacturer´s instructions (Qiagen, USA). Samples were then sequentially washed with RW1 buffer (12,000 x g/RFC for 30 s, RT), RPE Buffer (12,000 x g/RFC for 30 s, RT), and 80% EtOH (12,000 x g/RFC for 2 min, RT). Columns were air dried at full speed (16,000 x g/RFC) for 5 min at RT and RNA was eluted in 20 μ l of RNase-free water. RNA concentration was determined using a Nanodrop1000 (PeqLab) and kept at -80°C until use.

3.7 cDNA synthesis and RT-qPCR

500-1000ng RNA were denatured in 20 μ l of RNase-free water (15 minutes at 70°C). Then, the cDNA reaction mix (Table 3.2) was added to each sample and incubated for one cycle at 20°C for 10 min, one cycle at 43°C for 75 min, and one cycle at 99°C for 5 min. Finally, cDNA was diluted with RNase-free water and kept at -20°C until use. The RT-qPCR reaction mix was prepared using 1X Light Cycler 480 SYBR Green Master mix and the desired primer pair (final concentration 5 μ M) (Table 2.4). Samples were loaded in a 96-well plate and incubated in a LightCycler 480II (Roche, Germany) following these steps: Pre-incubation: (1 cycle) 50°C for 2 min. Denaturation: (1 cycle) 95°C for 5 min. Amplification: (45 cycles) at 95°C for 5s, 59°C for 5s, 72°C for 5s. Melting curve: (1 cycle) 95°C for 5s, 60°C for 1min. Cooling: (1 cycle) 40°C for 30s. A two-derivative analysis was used to determine Ct values and the 2- $\Delta\Delta$ Ct method (Livak

and Schmittgen, 2001) was used to calculate the relative fold gene expression to each control.

Table 3.2: cDNA synthesis mix preparation.

Reagent	Article ID	Stock concentration	Final concentration
Random Hexamers	N8080127	50 μ M	10 μ M
dNTP Mix	R0192	10mM	2mM
5X First – Strand Buffer	1805701	5X	1X
0,1 M DTT	1805701	100mM	40mM
Reverse Transcriptase	28025013	200U/ μ l	10U/ μ l
RNAse Inhibitor	N8080119	20U/ μ l	4U/ μ l

3.8 Bulk RNA-Sequencing

Bulk RNA was isolated as described previously from 3 different biological replicates at 7 dpi and samples were sent to the Helmholtz Core Facility Genomics (Germany). mRNA was enriched using oligo(dT) magnetic beads and libraries were prepared using Illumina® Stranded mRNA Prep, Ligation Kit. Samples were ligated to adapters and paired-end strand-specific sequenced using NovaSeq6000 S2 Flowcell with 200 cycles (Read1: 100-Index i7: 10 Index i5: 10 Read2: 100, 30 Million reads/sample). Adapter trimming was performed using Cutadapt (v2.10) with adapter sequence of -A CTGTCTCTTATA -a CTGTCTCTTATA. In parallel, the low-quality reads were cut off with -q 15 using Cutadapt (v2.10). HISAT2 (2.2.1) was used to align reads against GRCh38 reference genome. Mapped reads were quantified using HTseq (v0.13.5) with setting “-stranded reverse”. The gene annotation used for quantification was Ensembl version 108. Quality controls were performed in R.

3.9 Differential expression analysis

Raw counts were corrected for batch bias due to biological variance using ComBatseq package and due to unknown variables calculating surrogate variables on svaseq package (Team, 2008). Then, differential expression analysis was done using the DESeq2 package (pAdjustMethod = "BH", alpha = 0.05, filterFun=ihw) and shrinkage of the log-fold change (LFC) (Team, 2008). Differentially expressed genes (adjusted p-value < 0.05, LFC > 0) were extracted and used for downstream analysis and data exploration (Team, 2008). Gene set enrichment analyses were performed using fgsea, DOSE, and ClusterProfiler R packages (Team, 2008).

3.10 Formalin-Fixed Paraffin-Embedding of PCLS

PCLS were fixed using 4% paraformaldehyde (PFA) for 1h at 37°C or overnight at 4°C. PCLS were then transferred to embedding cassettes and processed by a Microm STP 420D Tissue Processor (Thermo Scientific, USA) following next steps: 4% Formalin (2 cycles, 60 min each), 50% EtOH (1 cycle, 60 min), 70% EtOH (1 cycle, 60 min), 96% EtOH (2 cycles, 60 min each), 100% EtOH (2 cycles, 60 min each), Paraffin (1 cycle, 30 min), and Paraffin (3 cycles, 45 min each). Then, tissue was embedded in paraffin Type 3 (Thermo Scientific, USA) using the modular tissue embedding center EC 350 (Thermo Scientific, USA), and blocks were kept at 4°C until use. 4 μ m formalin-fixed paraffin-embedded (FFPE) sections were cut using a Hyrax M55 microtome (Zeiss, Germany) mounted on slides, dried overnight at 40°C, and kept at 4°C until use.

3.11 Immunofluorescence of fresh tissue

Fresh PCLS were fixed with either 4% PFA for 1h at 37°C or overnight at 4°C or with ice-cold methanol (MeOH) for 10 min at -20°C. Samples were washed once with 1X PBS, and PFA-fixed samples were permeabilized with 0.5% triton X-100 in 1X PBS (PBST) for 15 min at RT and washed 3X with 0.1% PBST. All samples were blocked with 10% normal donkey serum in 0.1% PBST for 1h at RT. Then, samples were incubated with primary antibodies (Table 2.11) diluted in 1% normal serum solution in 0.1% PBST at 4°C overnight. The next day, samples were washed 3X with 0.1% PBST and incubated with secondary antibodies (Table 2.12) and DAPI (1:500) diluted in 1% normal serum solution in 0.1% PBST at RT for 2h. Finally, samples were washed 3X with 0.1% PBST, 10 min each time, and kept in 1X PBS until imaging.

3.12 Immunofluorescence of FFPE sections

FFPE sections were dried at 60 °C for 30 min to 1 h. Then, they were deparaffinized with the following steps: Xylene (2 cycles, 5 min each), 100% EtOH (2 cycles, 3 min each), 90% EtOH (1 cycle, 3 min), 80% EtOH (1 cycle, 3 min), 70% EtOH (1 cycle, 3 min), and Milli-Q water (1 cycle, 5 min). Then, they were exposed to heat-induced antigen retrieval (10 mM citrate buffer, pH=6.0, 1 cycle at 125°C for 30s, 1 cycle at 90°C for 10s). Slides were washed twice with 1X PBS and blocked for 1h at RT in a humid chamber with 10% Normal Donkey Serum in DAKO Antibody Diluent (Agilent Technologies, USA). mPCLS were blocked using an M.O.M.® (Mouse on Mouse) Blocking Reagent (Vector Laboratories, USA) for 1h at RT in a humid chamber when mouse anti-mouse primary antibodies were used. Then, samples were incubated with primary antibodies (Table 2.11) diluted in DAKO Antibody Diluent (Agilent Technologies, USA) and incubated at 4°C, overnight in a humid chamber. The next day, samples were washed twice in

1X PBS and incubated with secondary antibodies (Table 2.12) diluted 1:250 in 1% bovine serum albumin (BSA) in PBS and incubated for 2h at RT in a humid chamber. hPCLS were blocked with the Vector® TrueVIEW® Autofluorescence Quenching Kit (Vector laboratories, USA) for 2-3min at RT in a humid chamber. Finally, samples were counter-stained with DAPI (1:500) for 10 min at RT in a humid chamber and mounted using DAKO Fluorescence mounting medium (Agilent Technologies, USA). Finally, samples were imaged with the fluorescence microscope AxioImager.M2 (Zeiss, Germany). 3-5 regions of interest were captured. Then, the nuclear overlap with the DAPI signal for nuclear proteins (*CDKN1A*/P21, CC3) or the MFI was quantified in ImageJ.

3.13 Immunofluorescence of cells

Organoids were fixed with either 4% PFA for 15 min at RT or with ice-cold MeOH for 10 min at -20°C. Primary human fibroblasts were fixed with MeOH for 10 min at -20°C. Samples were washed once with 1X PBS, and PFA-fixed samples were permeabilized with 0.5% PBST for 15 min at RT and washed 3X with 0.1% PBST. All samples were blocked with 5% normal serum (goat or donkey, depending on secondary antibodies) in 0.1% PBST for 1h at RT. Then, samples were incubated with primary antibodies (Table 2.11) diluted in 1% normal serum solution in 0.1% PBST at 4°C overnight. The next day, samples were washed 3X with 0.1% PBST (Organoids, 30 min each time) and incubated with secondary antibodies (Table 2.12) and DAPI (1:500) diluted in 1% normal serum solution in 0.1% PBST at RT for 2h. Finally, samples were washed 3X with 0.1% PBST, 10 min each time, and kept in 1X PBS until imaging. Organoids and pHLF were imaged using an LSM710 confocal microscope (Zeiss, Germany). For the transdifferentiation assay, the MFI was quantified in ImageJ and normalized to the DAPI count.

3.14 MACS sorting from mPCLS

10-20 mPCLS were washed once with DPBS and incubated in Dispase solution (50U/ml, Corning Inc, USA) for 30-40 min at RT. Then, mPCLS were manually minced in a 3 cm petri dish with PCLS medium containing 0.04 mg/ml DNaseI (AppliChem GmbH, Germany). Single-cell suspension was sequentially filtered through 100um and 40um nylon filters, spun down (200 RCF for 10 min, 15°C), resuspended in MACS cold buffer, and cell number was determined. Cells were spun down (200 RCF for 10 min, 15°C) and resuspended in 90 μ l of MACS Buffer per 10^7 total cells and 10 μ l of murine CD45 MicroBeads per 10^7 total cells were added. Cells were incubated at 4°C for 20min and MACS sorter was used to deplete CD45+ cells. The flow through was spun down (200 RCF for 10 min, 15°C), resuspended in 90 μ l of MACS Buffer per 10^7 total cells, and

10 μ l of murine EpCAM MicroBeads per 10^7 total cells were added. Cells were incubated at 4°C for 20min and a MACS sorter was used to enrich epithelial cells (EpCAM+). The final cell number was determined and kept on ice until use.

3.15 MACS sorting from hPCLS

16-18 hPCLS were manually minced in a 3 cm petri dish with Dispase/Collagenase digestion solution and incubated at 37°C for 30 minutes. Shaking (400 rpm). Then, the tissue was mechanically triturated with a 10 ml pipette 4-6 times and incubated for an additional 30 minutes. Single-cell suspension was sequentially filtered through 100um and 40um nylon filters, spun down (200 RCF for 10 min, 15°C), resuspended in MACS cold buffer, and cell number was determined. Cells were spun down (200 RCF for 10 min, 15°C), resuspended in 90 μ l of MACS Buffer per 10^7 total cells, and 10 μ l of human EpCAM MicroBeads per 10^7 total cells were added. Cells were incubated at 4°C for 20min and a MACS sorter was used to enrich epithelial cells (EpCAM+). The final cell number was determined and kept on ice until use.

3.16 Organoid assay

Fibroblast proliferation was inhibited using 10 μ g/ml Mitomycin C for 2h, at 37°C. Fibroblasts were then washed twice with DPBS and kept in fresh medium for at least 1h at 37°C. Then, they were trypsinized, counted, and kept on ice until use. Fibroblasts and primary human or murine AT2 cells were mixed 1:1 ratio, spun down for 10 min at 300 RFC, and volume was adjusted to 25 μ l per well. The cell suspension was then mixed in a 1:1 ratio with Matrigel and 50 μ l of this mix was loaded in 96-well plates. Plates were incubated at 37°C for 10-15 min and finally 100 μ l of organoid medium supplemented with Rock inhibitor (3.3) were added. After 48h, the rock inhibitor was removed and the medium was changed afterward every 2-3 days. After 10-14 days, wells were filled up with PBS, cover with an optical foil, and imaged using a LifeCellImager Observer Z1 (Zeiss, Germany) at 5X. Maximum projections were generated using the software Zen Blue edition (Zeiss, Germany) and czi. files were exported. These files were then used to determine the organoid size and number using the “Napari organoid counter” (Bukas, 2022). On the image viewer, organoid detection was curated and a table with diameters from each detected organoid was generated. The mean size per organoid was calculated and organoids of at least 50um were included for further statistical analysis on GraphPad Prism 9.5.1.

Table 3.3: Organoids culturing medium.

Reagent	Final concentration
DMEM-F12 (1:1)	1x
GlutaMAX	1x
Penicillin/Streptomycin	1x
AmphotericinB	1x
Insulin-Transferrin-Selenium-Sodium	1x
Pyruvate (100x)	
Cholera toxin	0.1 μ g/ml
EGF	0.025 μ g/ml
Bovine pituitary extract	30 μ g/ml
FBS	5%
Retinoic Acid	0.01 μ M
ROCK inhibitor	10 μ M

3.17 Protein quantification of PCLS supernatants

Supernatants (100-200 μ l) from PCLS were concentrated using the Amicon Ultra-0.5 Centrifugal Filters 3 kDa MWCO (Merck, Germany). For this, samples were loaded in the filters and spun down at 12,000 x g/RFC for 30 min. Then, 3 washes with molecular biology grade water were done (12,000 x g/RFC, 30 min each). Finally, columns were placed inverted in new collection tubes and samples were eluted at 12,000 x g/RFC for 10 min. Samples were kept at -20°C until use. Total protein content was determined using the Pierce™ BCA Protein Assay Kit (Thermo Scientific, USA) for microplates. In short, 25 μ l of sample or standard were added in duplicates and mixed with 200 μ l of the working solution. The microplate was incubated for 30min at 37°C and absorbance was measured at 562 nm using a microplate reader Tecan Sunrise (Tecan GmbH, Germany). Absorbance values were then calculated by subtracting the background signal and protein concentration was calculated by interpolation of a linear regression using GraphPad Prism 9.5.1.

3.18 ELISA

Supernatants from hPCLS were used to quantify the secretion of different cytokines and growth factors by ELISA, following the manufacturer's instructions. For GDF-15 and CRIPTO1, I followed the next steps for DuoSet ELISA kits (R&D Systems, USA): Microplates were pre-coated overnight at RT with capture antibody to the working concentration in PBS without carrier protein. Then, microplates were washed 3 times with wash buffer (0,05% Tween20 in PBS, pH 7,2-7,4) and blocked with reagent diluent (1% BSA in PBS, pH 7,2-7,4) for 1h at RT.

Again, microplates were washed 3 times with wash buffer and 100 μ l of samples and standards were loaded in duplicates. Microplates were incubated for 2h at RT, washed 3 times with wash buffer, and incubated with detection antibody diluted in reagent diluent for 2h at RT. Microplates were washed 3 times with wash buffer, incubated with Streptavidin-HRP solution for 20min at RT, washed 3 times with wash buffer, and incubated with substrate solution (1:1 mixture of Color Reagent A (H₂O₂) and Color Reagent B (Tetramethylbenzidine)) for 20min at RT. Finally, the stop solution was added and absorbance was immediately measured at 450 nm (reference 570 nm) using a microplate reader Tecan Sunrise (Tecan GmbH, Germany). Absorbance values were then calculated by subtracting the background signal and concentrations were calculated by interpolation of a linear regression using GraphPad Prism 9.5.1. For collagen type III N-terminal propeptide (PIIINP) we followed these steps: 100 μ l of standards and samples were loaded in duplicates and samples were balanced using 10 μ l of balance solution per well. Then, the conjugate was added to all wells, and microplates were incubated for 1h at 37°C. Microplates were washed 5 times with washing buffer, and incubated with substrate solution for 15-20min at 37°C. Finally, the stop solution was added and absorbance was measured at 450 nm (reference 570 nm) using a microplate reader Tecan Sunrise (Tecan GmbH, Germany). Absorbance values were then calculated by subtracting the background signal and concentrations were calculated by interpolation of a linear regression using GraphPad Prism 9.5.1.

3.19 Cytokine arrays

To longitudinally characterize the SASP, I used a cytokine array on supernatants from hPCLS at 3, 5, 7, and 9 dpi. For this, the total protein content was determined for each sample. Then, I pooled together 3 biological replicates per membrane adjusting the volume to have 12 μ g per time point and condition (0 or 30 Gy). To determine the secreted cytokines on BALF from 5 healthy donors and 5 IPF patients (Table 2.2), I determined the protein concentration from each sample and pooled them together adjusting the volume to have 15 μ g per condition.

For both sets of samples, I followed the manufacturer's instructions (R&D Systems, USA): Membranes were blocked using Array Buffer 4 for 1h at RT. Then, samples were diluted in Buffer 4 and 6, added to each membrane, and incubated at 4°C overnight in a rocking platform. The next day, membranes were washed 3 times with 1X wash buffer (10 min at RT, each time) and incubated with Detection Antibody Cocktail for 1h at RT in a rocking platform. Then, membranes were washed 3 times with 1X wash buffer (10 min at RT, each time) and incubated with 1X Streptavidin-HRP for 30min at RT in a rocking platform. Finally, membranes were washed 3 times with 1X wash buffer (10 min at RT, each time), transferred to a plastic sheet protector, and the Chemi Reagent Mix was added to each membrane. Excess liquid was removed, mem-

branes were incubated for 1 min and Chemiluminescence was detected using a ChemiDoc XRS+ Universal Hood II (Bio-Rad, USA). Then, the average pixel density from the duplicate spots was calculated after subtracting the background signal.

For hPCLS, a fold change (30Gy/0Gy) was calculated and the cytokines with a fold change ≥ 1.3 were used for enrichment analysis in R (Team, 2008) using the ClusterProfiler package for gene ontology (biological processes) and disease ontology enrichment analysis (Team, 2008). I used the tools InteractiVenn and Draw Venn Diagram (<https://bioinformatics.psb.ugent.be/webtools/Venn/>) to determine the overlap of cytokines among different time points (Heberle et al., 2015). A table of upregulated cytokines in at least one of the time points was generated (Table 6.2)) and plotted in a heatmap using GraphPad Prism 9.5.1. For BALF samples a fold change (IPF/Donor) was calculated and the cytokines with a fold change ≥ 1.3 were plotted as raw intensities in a heatmap using GraphPad Prism 9.5.1.

3.20 Senolytics treatment on PCLS

hPCLS were plated in 96-wells, irradiated with 0 or 30 Gray (Gy), and cultured for 5 days in DMEM-F12 supplemented with 0.1% FCS, 1% penicillin/streptomycin and 1% amphotericin B. Then, senolytic treatment and control diluent solutions were freshly prepared by diluting them to the working concentration (Table 3.4) on the culture medium described above. Treatments were then added and samples were collected after 48h.

Table 3.4: Senolytic treatment on PCLS.

Reagent	Stock concentration	Working concentration	Diluent control
ABT-263	10mM	5 μ M	DMSO
Dasatinib	200mM	0.2mM	DMSO
Quercetin	100mM	50 μ M	DMSO

3.21 Cripto-1 treatment on cells and PCLS

Recombinant human Cripto-1 protein was reconstituted to 10 μ g/ml in 0.1% BSA in 1X DPBS. PCLS were prepared and after 24h, treatment or diluent control was added (Working concentration: 100ng/ml in culture medium). Treatment was replenished every 48h, and samples were collected after 4 days of sequential treatments. Primary human Fibroblasts (50.000 per 6-well) were seeded using DMEM-F12 supplemented with 10% FCS and 1% penicillin/streptomycin. After 24h, cells were starved using DMEM-F12 supplemented with 0.1% FCS and 1% peni-

cillin/streptomycin overnight. The next day, cells were treated with diluent control or recombinant human Cripto-1 (rhCripto1) (Working concentration: 100ng/ml in culture medium) and cells were stopped for RT-qPCR at 48h. For the transdifferentiation assay were seeded in triplicates (15000 cells/ well) in 96-well plates, starved after 24 h, and treated with only medium, rhCripto1 (Working concentration: 100ng/ml in culture medium) or TGF- β 1 (Working concentration: 1ng/ml). Cells were stopped after 72 h for IF.

Chapter 4

Results

4.1 Validation of radiation-induced senescence in murine and human PCLS

4.1.1 IR induces DNA damage response in PCLS

DNA damage response is induced by IR and it is also increased in senescent cells (Pospelova et al., 2009). Therefore, the expression of γ H2Ax, one marker for DDR, was evaluated by IF 1 hour after exposure to different doses of IR: 0, 30, 60, and 120 Gy (Fig. 4.1A). Fresh mPCLS and FFPE sections from hPCLS were stained for γ H2Ax. Then, the percentage of double-positive nuclei (DAPI and γ H2Ax) was quantified with ImageJ. In mPCLS a general increase in the nuclear recruitment of γ H2Ax as early as 1-hour post-irradiation with all doses was found, however, the effect was only statistically significant after exposure to 30Gy and 60Gy (Fig. 4.1B, C). Similarly, hPCLS showed significant induction of nuclear γ H2Ax expression as early as 1 hour after exposure to 30 Gy (4.1B, C). In both lung tissues, the injury was uniformly distributed covering all different locations in the lung, suggesting that this dose targets several cell types. In conclusion, 30Gy are sufficient to induce DNA damage in murine and human PCLS.

4.1.2 IR does not reduce metabolic activity or viability of PCLS

To find the effective dose to induce senescence with limited cell death, hPCLS and mPCLS were irradiated with different doses (0, 30, 60, 120Gy) and culture up to 7 dpi. For mPCLS, supernatants were collected at 1, 3, and 7 dpi and for hPCLS at 1, 4, and 7 dpi. First, these supernatants were used for a water-Soluble Tetrazolium 1 (WST-1) assay in order to determine

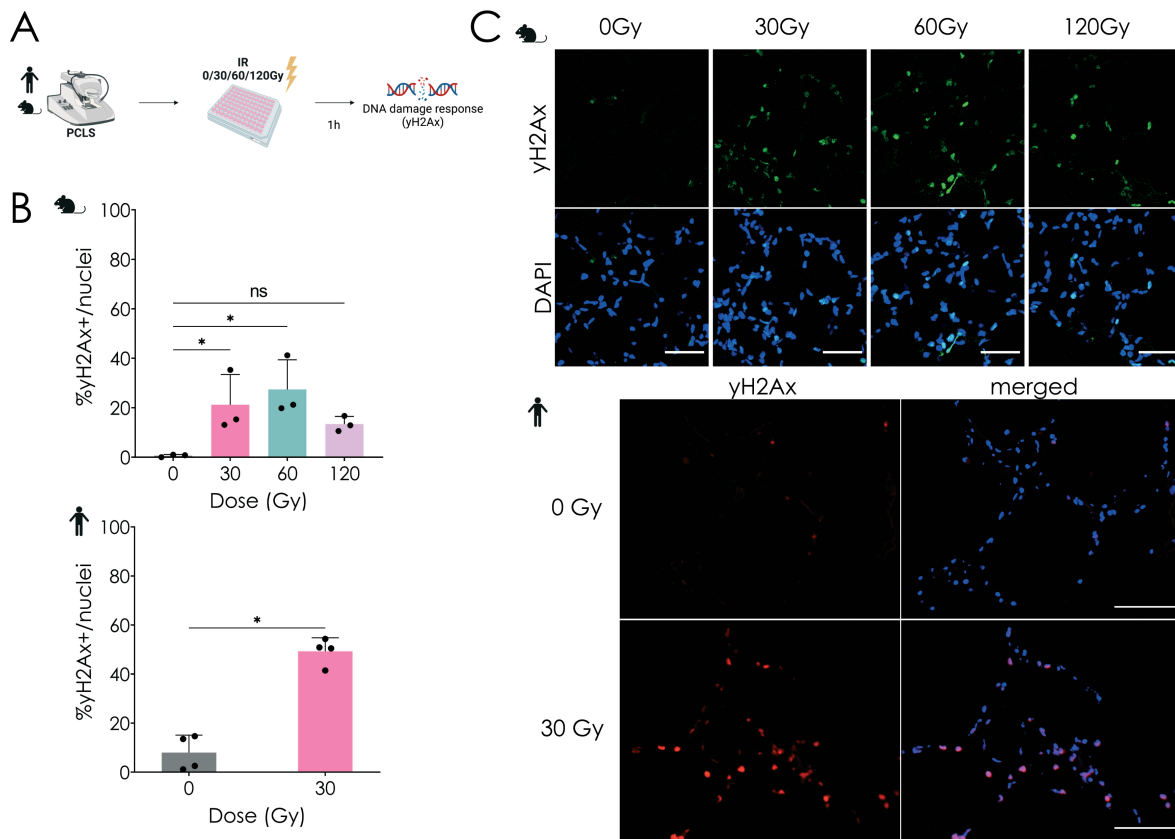


Figure 4.1: Induction of DNA damage response after ionizing radiation of PCLS. A. Experimental design. PCLS from murine and human lung tissue were generated and exposed to 0, 30, 60, or 120 Gy. After one hour, tissue was fixed and stained for the DDR-related protein: γ H2Ax. Created with BioRender.com. B. Quantification of γ H2Ax+ nuclei in mPCLS and hPCLS. Means + SD are shown in bars. Single points represent independent biological replicates (n=3-4). *-p-values < 0.05 after one-way ANOVA (mPCLS) or Mann-Whitney test (hPCLS), followed by Dunnet's multiple comparisons tests. C. Representative images of mPCLS and hPCLS stained for γ H2Ax. Scale bar: 50 μ m.

metabolic activity after IR (Fig.4.2A). Both murine and human PCLS showed a dose-dependent reduction in metabolic activity during the culturing time, however, this was not significantly different from the non-irradiated controls (Fig. 4.2C). Since the lowest dose (30 Gy) showed significant induction of DNA damage (Fig.4.1B, C) without significantly reducing metabolic activity (Fig. 4.2C), I tested cytotoxicity via two independent methods using only 30Gy in both murine and human PCLS. On one hand, supernatants were used for a lactate Dehydrogenase (LDH) release assay. IR-PCLS remained viable after 7 days with no significant difference in comparison to the non-irradiated controls (Fig.4.2D). On the other hand, tissue was fixed with 4%PFA, embedded in paraffin, and stained for CC3, an indicative marker for apoptosis. Here, I did not observe any significant changes in CC3 expression in irradiated PCLS, when compared to controls (Fig.4.2B, E). Therefore, 30Gy was selected as the dose to establish and characterize

IR-induced senescence ex vivo.

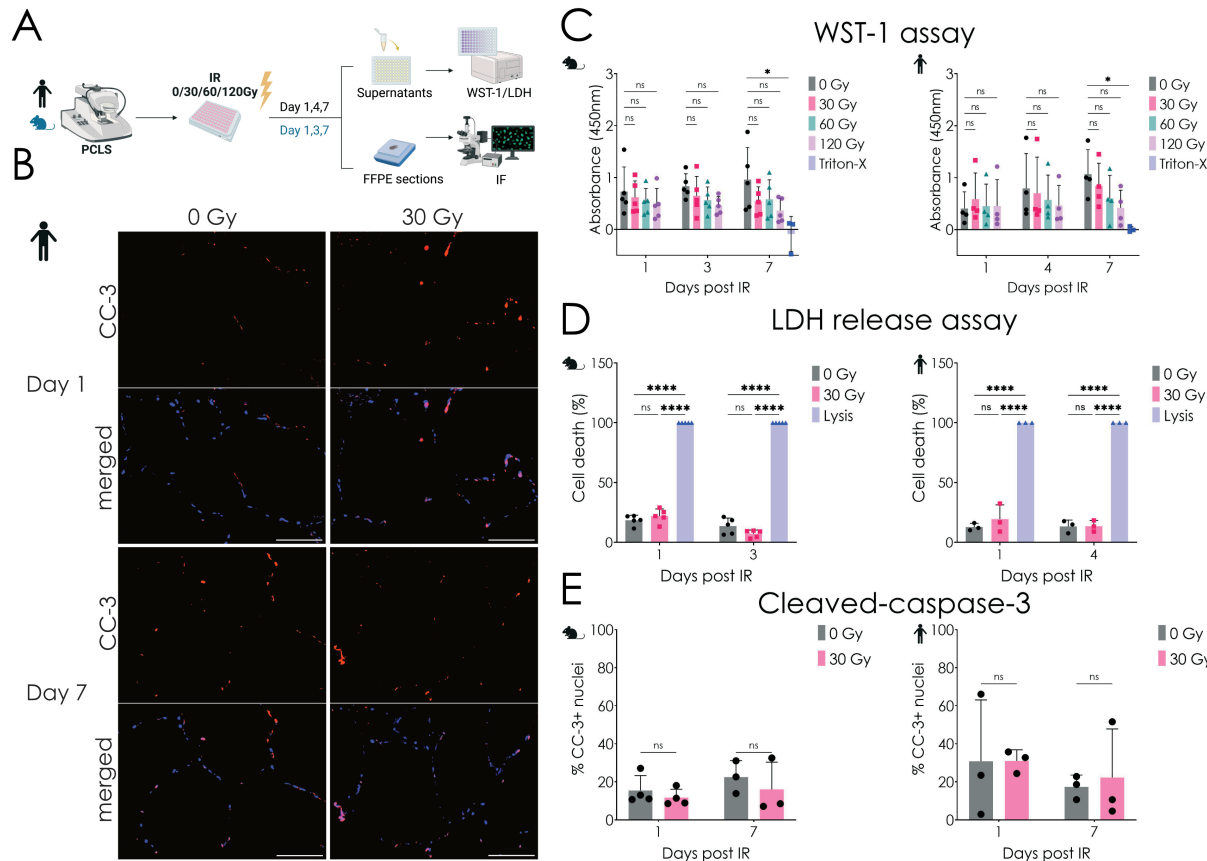


Figure 4.2: Assessment of viability and metabolic activity in IR-PCLS. A. Experimental design. PCLS from murine and human lung tissue were generated and exposed to 0, 30, 60, or 120 Gy. After different time points, supernatants from mPCLS and hPCLS were collected and used for WST-1 and LDH release assay. Fresh tissue was fixed, embedded in paraffin, and FFPE sections were stained for CC3. Created with [BioRender.com](https://biorender.com). B. Representative images of hPCLS stained for CC3 after 1 and 7 dpi. Scale bar: 50 μm. C. Absorbance values after WST-1 assay on mPCLS and hPCLS at different times after IR. D. Cytotoxicity determined by LDH release assay on supernatants from mPCLS and hPCLS at different times after IR. E. Quantification of CC3 nuclear expression in mPCLS and hPCLS at 1 and 7 dpi. Means + SD are shown in bars. Single points represent data from at least 3 independent biological replicates. *-p-values < 0.05 after Two-way ANOVA (mPCLS), followed by Sidak's multiple comparisons tests.

4.1.3 IR induces P21-dependent cell cycle arrest in PCLS

Senescent cells are characterized by being in a stable cell cycle arrest (Chaib et al., 2022; González-Gualda et al., 2021). Therefore, I used RT-qPCR and IF to determine the expression of the cell cycle inhibitors *CDKN1A*/P21 and *CDKN2A*/P16 in mPCLS and hPCLS at different time points after exposure to IR (Fig.4.3). In mPCLS, a significant increase of *CDKN1A*/P21 gene expression at 7 dpi was found for all doses, while at protein level this was only significant after exposure

to 30Gy as determined by IF (Fig.4.3A, B). For hPCLS, I observed a consistent increase in gene expression of *CDKN1A*/P21 for all doses already from 1 dpi that was sustained until 7dpi (Fig.4.3A, B). This was also confirmed at the protein level after exposure to 30Gy as shown by the IF staining and quantification on Fig.4.3B, C. This also revealed that the induction of *CDKN1A*/P21 was homogeneously distributed in the whole tissue, suggesting that the chosen dose is enough to induce cell cycle arrest dependent on the *CDKN1A*/P21 pathway ex vivo in both murine and human lung tissue (Fig.4.3C). On the *CDKN2A*/P16 axis, I observed a tendency to increase at 7dpi only for hPCLS but this effect did not reach statistical significance for either mPCLS or hPCLS (Fig. 4.3A). In conclusion, IR induces a *CDKN1A*/P21-dependent cell cycle arrest in PCLS that is sustained after 7 dpi.

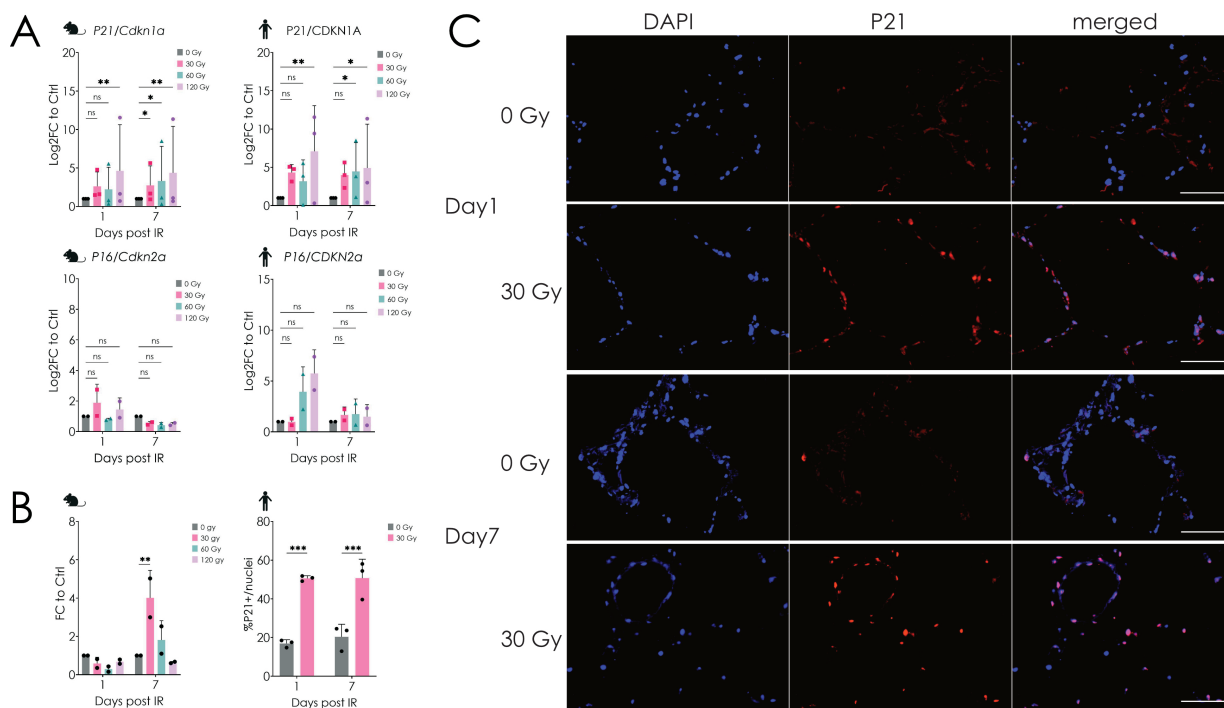


Figure 4.3: Characterization of cell cycle arrest induction over time after IR. A. Gene expression assessed by RT-qPCR of the cell cycle inhibitors: *CDKN1A*/P21 and *CDKN2A*/P16 in mPCLS and hPCLS at 1 and 7 dpi. B. Quantification of nuclear expression of *CDKN1A*/P21 for both murine and human PCLS after IF. Means + SD are shown in bars. Single dots represent independent biological replicates (n=3). * p-value< 0.05 after two-way ANOVA, followed by Sidak's multiple comparisons tests. FC: Fold change (30Gy/0Gy). C. Representative IF images of hPCLS stained for *CDKN1A*/P21 after 1 and 7 dpi. Scale bar: 50 μ m.

4.1.4 Senescence-Associated β -Galactosidase activity is increased in IR-PCLS

Then, I tested whether the SA- β -gal activity was increased after IR as commonly used to identify senescent cells (B. Y. Lee et al., 2006). For this, I established a protocol to stain fresh human and murine PCLS with the commercially available fluorogenic probe SPiDER- β -gal at 7 dpi (Dojindo, USA). For this, fresh tissue was incubated for 1 hour at 37°C in culturing medium supplemented with BafA1. BafA1 induces lysosomal alkalinization to selectively detect SA- β -gal activity, which is detectable at a pH of 6 in senescent cells (Kurz et al., 2000). Then, PCLS were incubated for 30 min at 37°C, with culturing medium containing both BafA1 and the fluorogenic probe. Finally, PCLS were washed with PBS, counter-stained with Hoechst-dye for nuclear detection, and directly imaged in a confocal microscope (Fig. 4.4A). Here, we observed an upward trend in MFI for both murine and human PCLS, although this did not reach statistical significance (Fig. 4.4B, C). In conclusion, exposure to 30Gy induces SA- β -gal activity in murine and human PCLS.

4.1.5 IR-PCLS have a distinct senescence-associated secretory phenotype

After 7 days, I observed a complete senescent phenotype in IR-PCLS assessed by different well-accepted markers of cellular senescence (Liao et al., 2021). Therefore, I used a cytokine array and enzyme-linked immunosorbent assay (ELISA) to characterize the SASP on supernatants from mPCLS and hPCLS from day 7 on (Fig. 4.5A). Here, I found that each model had a distinct SASP profile, characterized by the secretion of different cytokines and growth factors. For mPCLS, I found an increase in the secretion of pro-inflammatory cytokines such as IL-6, C-C Motif Chemokine Ligand 20 (CCL20), CCL2, CXCL1 as well as previously described senescence-related proteins such as dipeptidyl peptidase 4 (DPP4) (K. M. Kim et al., 2017) (Fig. 4.5B). For hPCLS, I observed increased secretion of pro-inflammatory mediators such as TNF-a, thrombospondin 1 (THBS1), and C-X-C motif chemokine 11 (CXCL11), which have been linked to immune modulation and induction of paracrine senescence (Maciel-Barón et al., 2016; Meijles et al., 2017) (Fig. 4.5B). Notably, both mPCLS and hPCLS showed higher levels of Myeloperoxidase (MPO) and IFN γ after IR (Fig. 4.5B). Finally, ELISA confirmed a significantly increased secretion of the well-known SASP factor; GDF-15, in human IR-PCLS at 7 and 9 dpi (Fig. 4.5C). In conclusion, IR induces core senescence-related hallmarks such as increased DDR, stable cell cycle arrest, and SA- β -galactosidase activity. Moreover, irradiated PCLS secrete a combination of pro-inflammatory and growth factors, which composition changes depending on the species.

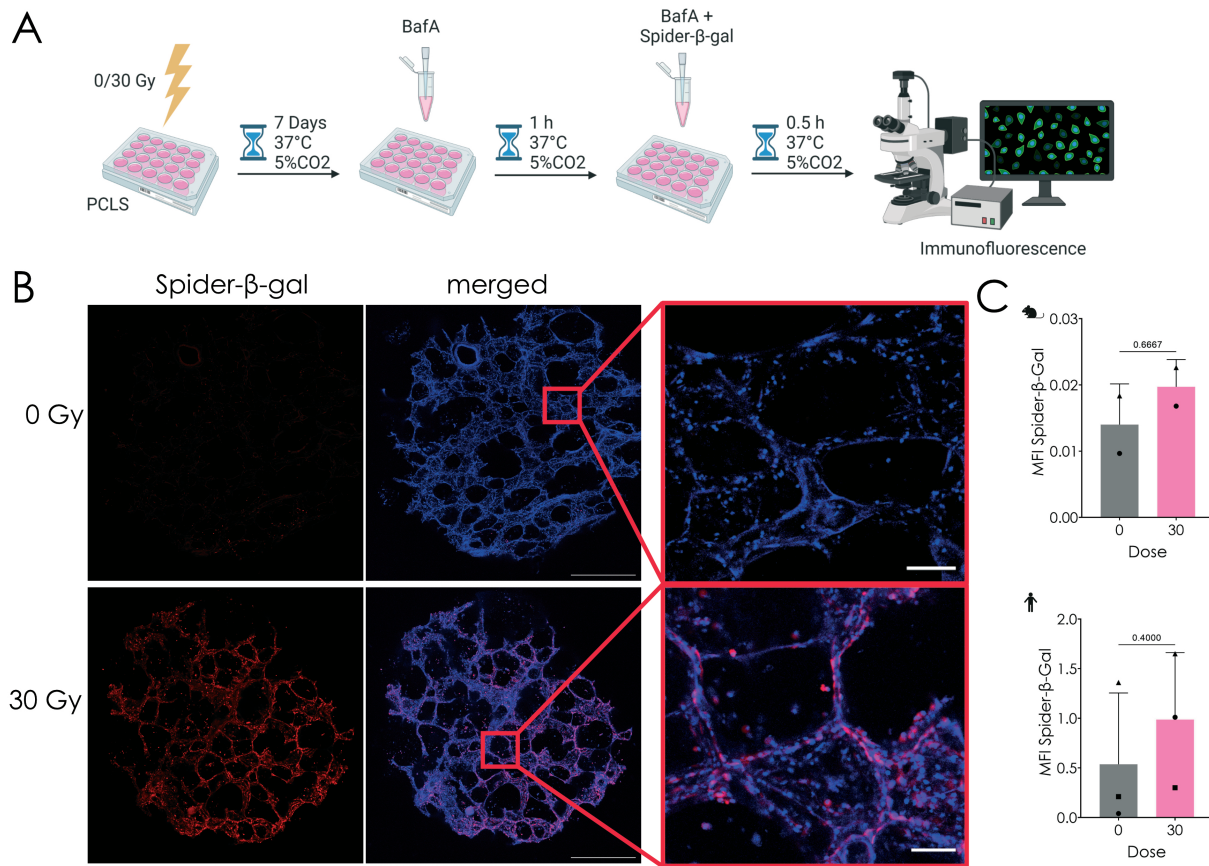


Figure 4.4: Induction of SA- β -Galactosidase activity in IR-PCLS. A. Protocol to stain fresh lung tissue with the fluorogenic probe SPiDER- β -gal for detection of SA- β -gal. PCLS were generated, exposed to IR and cultured for 7 days. Then, PCLS were incubated for 1h with BafA1, stained for SPiDER- β -gal for 0.5h, and imaged in a confocal microscope. Created with [BioRender.com](https://biorender.com). B. Representative images of irradiated and control hPCLS stained for SPiDER- β -gal. Nuclei were counter-stained with Hoechst-dye. Scale bar: 100 μ m. C. Quantification of the MFI for murine and human PCLS at 7dpi. Means + SD are shown in bars. Single points represent independent biological replicates (n=2-3). *p-values < 0.05 after Mann-Whitney test, followed by Dunnet's multiple comparisons tests.

4.2 Characterization of radiation-induced cellular senescence in human PCLS

4.2.1 Transcriptomics reveal a premature aging phenotype in IR-hPCLS

To characterize our human ex vivo model I used unbiased bulk-RNA sequencing and determine differentially expressed genes (DEG) and regulated pathways in IR-PCLS in comparison to non-irradiated controls at 7 dpi. First, I found a conserved response to treatment in all donors as

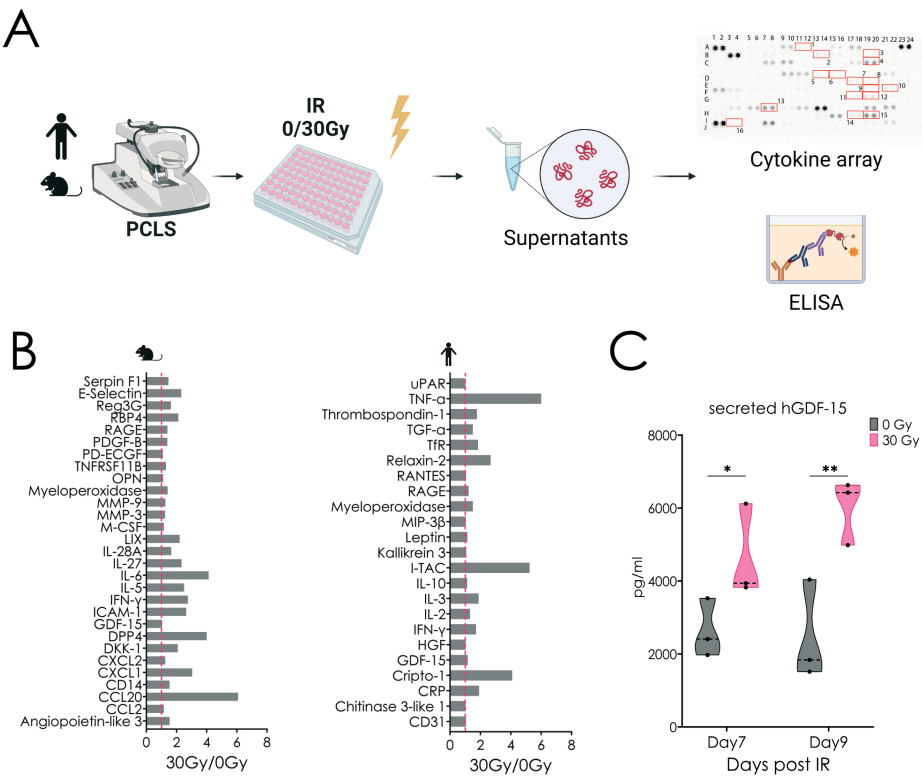


Figure 4.5: Profiling the senescence-Associated secretory phenotype of IR-PCLS. A. Experimental design. PCLS were irradiated and supernatants were collected after 7 and 9 dpi and used for cytokine arrays or ELISA. Created with [BioRender.com](https://biorender.com). B. Bar graph with upregulated cytokines in murine and human IR-PCLS at 9 dpi (n=1). C. Concentration of secreted GDF-15 in supernatants derived from human control or IR-PCLS measured by ELISA. Single dots represent biological replicates (n=3). *p-value< 0.05 after two-way ANOVA, followed by Sidak's multiple comparisons test.

observed after principal component analysis (PCA) (Fig. 4.6). Differential expression analysis revealed a total of 1457 upregulated and 1711 down-regulated genes after IR ($\log_{2}FC > 0$ and $p\text{-adj-val} < 0.05$) as shown in the Volcano plot. Then, I performed a Gene set enrichment analysis using the Hallmarks dataset on the Molecular Signatures Database (MSigDB) based on the DEG after IR (Liberzon et al., 2015; Liberzon et al., 2011). Here, I found a significant upregulation in interferon- and KRAS- signaling pathways, as well as inflammatory and TP53-dependent pathways (Fig.4.6C). On the other hand, pathways related to mitotic cell cycle progression were significantly downregulated (Fig.4.6C). Gene ontology enrichment analysis showed significant upregulation of processes involved in T and B cell activation and proliferation and down-regulation of biological processes involved in cell division and cell cycle progression (Fig.4.6D). Interestingly, epithelial cell markers were deregulated in as shown by strong upregulation of KRT17 and down-regulation of EpCAM (Suppl. Table 6.1), suggesting epithelial reprogramming in response to IR ex vivo. Finally, I run an enrichment analysis using previously published datasets related to cel-

lular senescence: Mayo-Senescence, REACTOME-SASP, and FRIDMANN-SENESCENCE-UP and DOWN (Fridman and Tainsky, 2008; Saul et al., 2022), as well as the list of upregulated cytokines in our secretome analysis (SASP-hPCLS) (Fig.4.6E). I found all these pathways to be positively enriched in our model, however, this did not reach statistical significance (Fig.4.6E). In conclusion, I showed for the first time that IR induces premature aging phenotype in hPCLS, characterized by stable cell cycle arrest, pro-inflammatory signaling, and epithelial reprogramming, recapitulating changes previously described *in vivo* during biological aging.

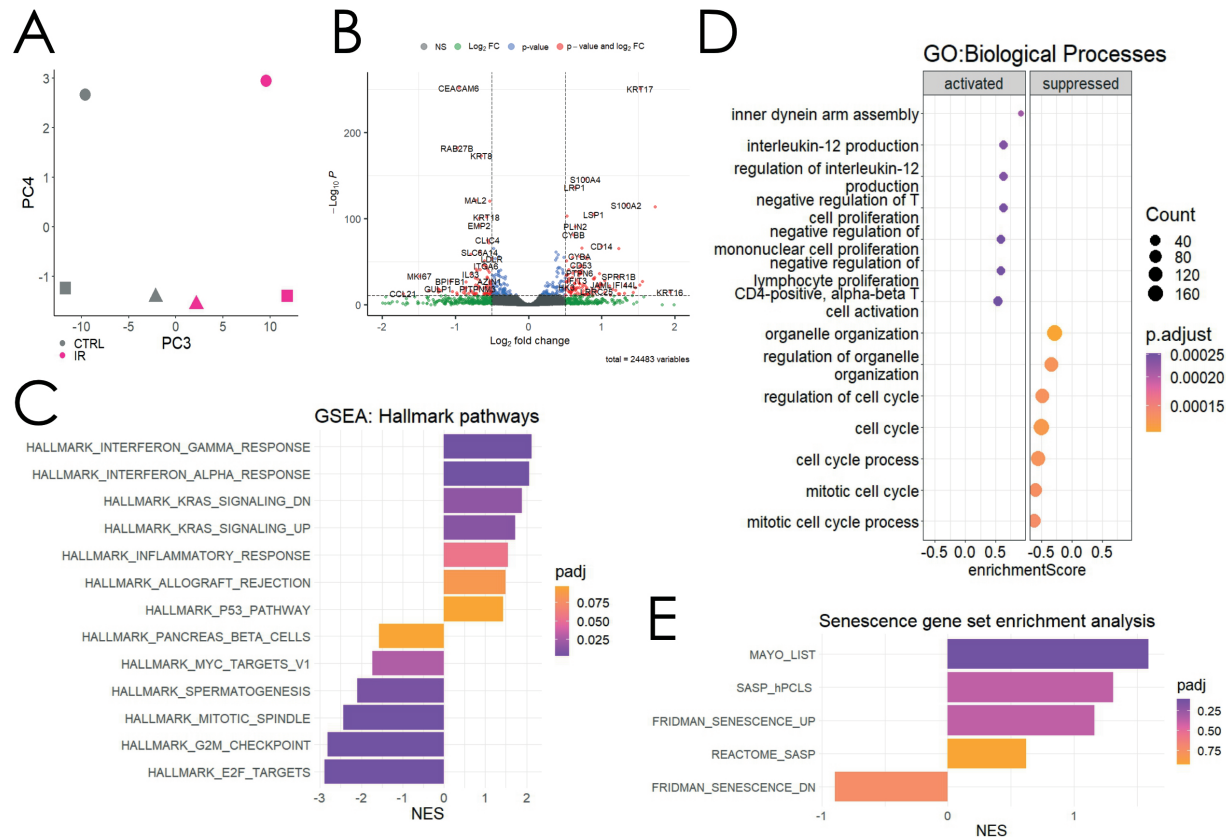


Figure 4.6: Transcriptional changes in IR-PCLS. A. Bulk-RNA seq was performed in control and IR-PCLS at 7dpi (n=3). After quality control, a PCA was performed. B. Volcano plot of differentially expressed genes (DEG) after IR. C. Gene set enrichment analysis of DEG for general hallmarks pathways. D. Gene set enrichment analysis of DEG for the gene ontology: Biological processes. E. Gene set enrichment analysis of DEG for senescence-related pathways. Bar colors show adjusted p-value.

4.2.2 IR induces epithelial cellular senescence in hPCLS

PCLS preserve both the cellular composition and architecture of the lung tissue (Gerckens et al., 2019; Lang et al., 2022). Therefore, it offers a unique platform to study global and specific cellular responses after an insult. Therefore, I evaluated which were the main cellular comp-

ments showing a senescent phenotype in IR-hPCLS. To test this, I co-stained FFPE sections for *CDKN1A*/P21 and markers for specific cell populations: AT1 cells (podoplanin (PDPN)), AT2 cells (SFTPC), and fibroblasts (alpha Smooth Muscle Actin (α -SMA)) at 1 and 7 dpi (Fig. 4.7A). Here, I found that hPCLS have a significantly increased *CDKN1A*/P21 expression in the alveolar epithelium (PDPN+ and SFTPC+ cells), whereas the expression of *CDKN1A*/P21 on fibroblasts did not significantly increase after IR (Fig. 4.7A, B). Accordingly, I also observed that 50% of SFTPC+ cells showed expression of γ H2Ax in IR-hPCLS (Fig. 4.7C, D). This together indicates that ex vivo, IR induces injury mostly in AT2 cells promoting DNA-damage-induced cellular senescence in the alveolar epithelium, which has previously been implicated in the pathogenesis of IPF.

4.2.3 Stem cell potential of epithelial lung progenitors is reduced in IR-hPCLS

The regeneration potential in the alveolar epithelium after injury is drastically reduced with aging and therefore, has been linked to the pathobiology of chronic lung diseases like IPF (Barkauskas et al., 2013; Lehmann et al., 2020; C. Yao et al., 2019). Since we observed a predominantly epithelial senescence phenotype in IR-hPCLS, I evaluated whether our model also recapitulates stem cell dysfunction ex vivo. To this end, I isolated primary EpCAM+ cells from human PCLS at 5 dpi and co-cultured them with primary lung fibroblasts in an organoid assay for 10 days (Fig.4.8A). To our knowledge, I showed for the first time that distal epithelial cells derived from PCLS can still form organoids, which indicates that these cells conserve their progenitor capacity, even after 5 days of culture in tissue explants as observed in the bright field images (Fig.4.8B). Immunofluorescence was used to determine the expression of typical markers for AT2 cells (SFTPC+), airway epithelium (Acetylated tubulin (ACT)+), and transitional AT2 cells (Keratin-8 (K8)+). Cells derived from IR-hPCLS showed an upward trend in the expression for K8 and SFTPC in comparison with the organoid forming cells derived from control PCLS (Suppl. Fig. 6.1). Notably, AT2 cells derived from IR-PCLS showed a significant reduction in both size and colony formation efficiency in comparison with non-irradiated AT2 cells (Fig.4.8 C), suggesting an impaired progenitor capacity after IR. This stem cell dysfunction was also observed for EpCAM+ cells derived from irradiated mPCLS after 14 days of organoid culture (Suppl. Fig. 6.2). Interestingly, the small organoids or cell agglomerates formed by progenitor cells derived from IR-hPCLS had high expression of γ H2Ax and *CDKN1A*/P21, both markers for cellular senescence (Fig.4.8D). In conclusion, I showed for the first time that the cellular niche present in PCLS supports the stem cell function of primary murine and human alveolar epithelial progenitor cells ex vivo. Moreover, cellular intrinsic changes induced by IR impairs their function as stem cell progenitors as described for aged and diseased lungs.

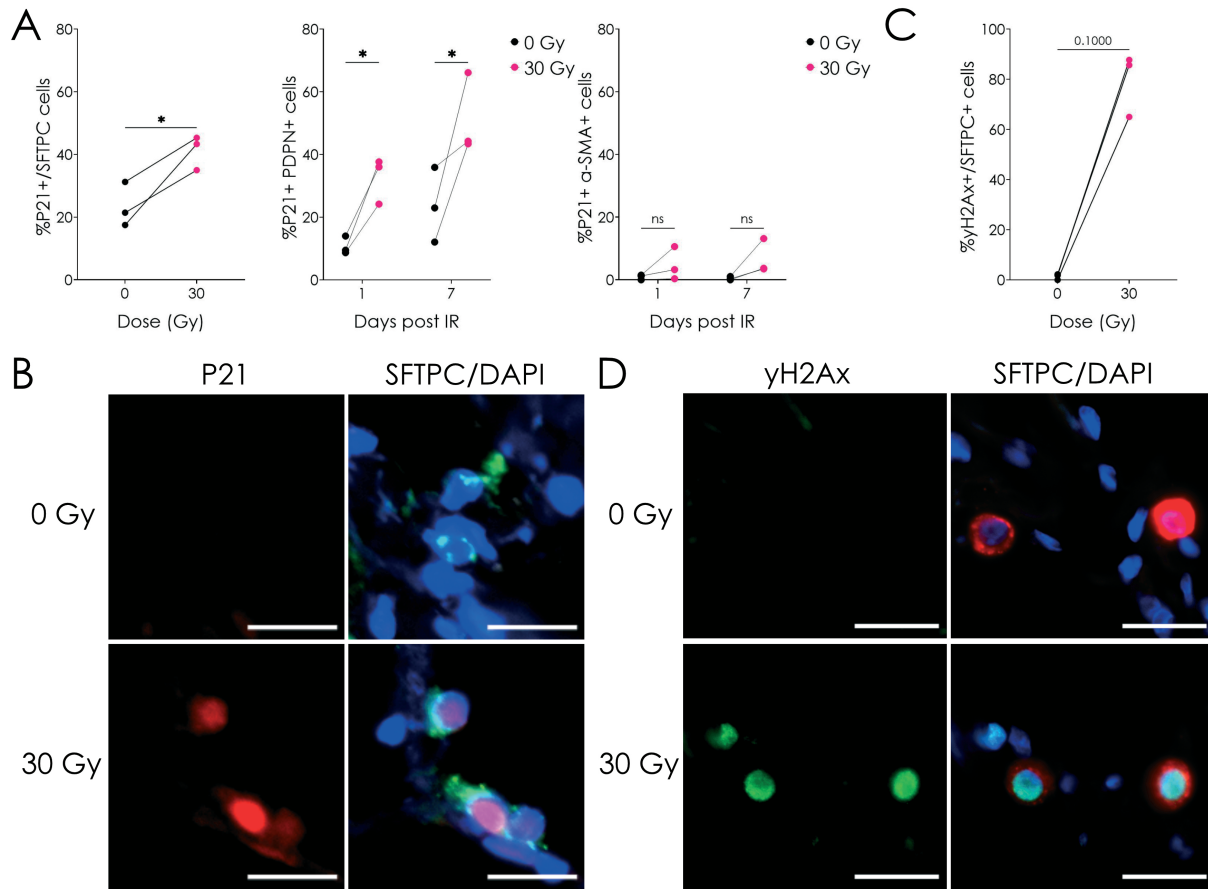


Figure 4.7: Epithelial cellular senescence in IR-hPCLS. A. Quantification of *CDKN1A*/P21+ expression in different cellular compartments at 1dpi for SFTPC+ cells and day 1 and 7 dpi for α-SMA+ and PDPN+ cells. Single points represent independent biological replicates (n=3). *-p-values < 0.05 after Mann-Whitney test (left) or two-way ANOVA (middle and right), followed by Sidak's multiple comparisons tests. B. Representative image of *CDKN1A*/P21 stained AT2 cells in control and irradiated PCLS at 1dpi. Scale bar: 20μm. C. Quantification of γH2Ax+ AT2 (SFTPC+) cells at 1h after IR. Single points represent independent biological replicates (n=3). *-p-values < 0.05 after Mann-Whitney test. D Representative image of γH2Ax stained AT2 cells in control and irradiated PCLS after 1-hour post IR. Scale bar: 20μm.

4.2.4 SASP from IR-PCLS is temporally dynamic and induces immune response modulation via inflammatory mediators

Detrimental effects by persistent senescent cells in the lung have been related to their ability to modulate their niche via active secretion of pro-inflammatory cytokines and growth factors known as the SASP (Chaib et al., 2022; Coppé et al., 2008). Here, I used a cytokine array to longitudinally characterize the SASP of IR-PCLS (Fig.4.9A). For this, supernatants were collected at 3, 5, 7, and 9 dpi from PCLS derived from 3 different donors and pulled together for each cytokine array. Then, chemiluminescent signals were quantified and analyzed (Fig.4.9A).

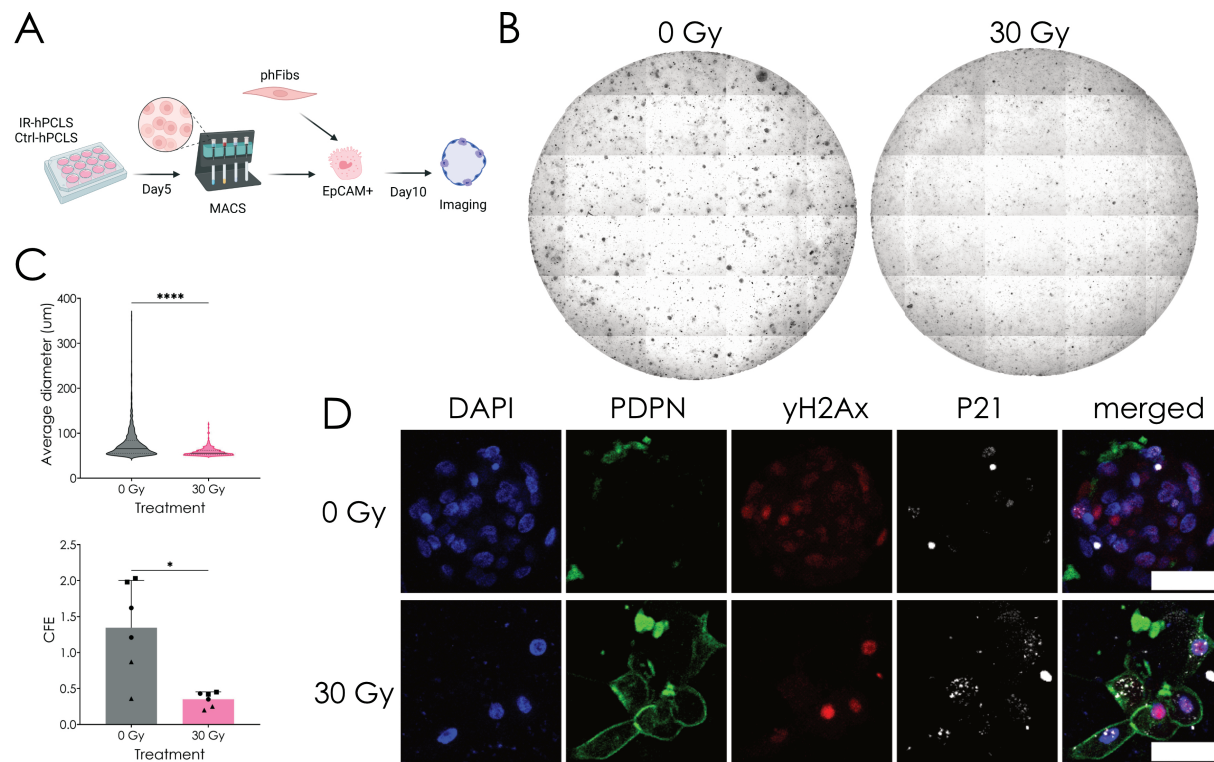


Figure 4.8: Stem cell capacity of alveolar progenitors in IR-hPCLS. A. Isolation of alveolar progenitors from hPCLS for organoid assay. PCLS were sliced, exposed to IR and after 5 days, a single cell suspension was prepared from them. EpCAM+ cells were isolated by MACS sorting and co-cultured with primary human Fibroblasts (phFibs) for 10 days. Created with [BioRender.com](https://biorender.com). B. Representative whole well images from a live cell microscope. C. Organoid size and colony formation efficiency (CFE) were determined for organoids bigger than $50\mu\text{m}$. Single points with the same form represent technical replicates from three independent biological replicates. * p-value < 0.05 after unpaired t-test (size) or Mann-Whitney test (CFE). D. Representative images of single organoids from control and IR-PCLS stained for Podoplanin (PDPN), γ H2Ax, and *CDKN1A*/P21. Scale bar: $50\mu\text{m}$.

In general, secretion of cytokines and growth factors previously described for senescent cells such as GDF-15, insulin-like growth factor-binding protein 3 (IGFBP-3), and IL-6, as well as, cytokines upregulated in pulmonary fibrosis like serpin Family F Member 1 (SERPINF1), transforming Growth Factor Alpha (TGF α), and stromal cell-derived factor 1 (SDF-1 α) (Fig.4.9B, D) was detected. To better characterize the SASP, a fold-change to the control (30Gy/0Gy) was calculated (Suppl. Table 6.2). Then, I compared the upregulated cytokines at the different time points and found that the SASP is highly dynamic over time, with very low overlapping cytokines among the analyzed time points (Fig.4.9B, D). Cytokines that had an upregulation of at least 1.3 times after IR were used for gene set enrichment analysis using the publicly available gene sets at the Molecular Signatures Database (MSigDB) for Gene ontology: Biological Processes (Liberzon et al., 2015; Liberzon et al., 2011) (Fig.4.9E). Here, I found an initial inflammatory

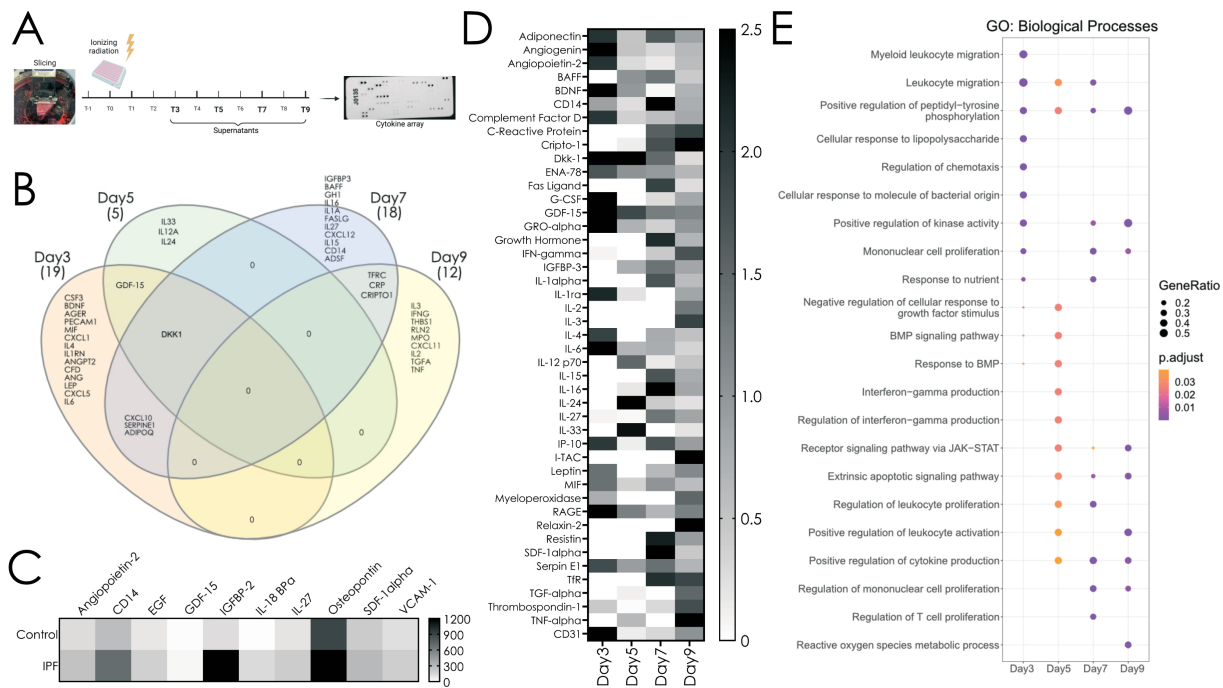


Figure 4.9: Longitudinal temporal characterization of SASP from IR-PCLS. A. Experimental design. Supernatants from control and irradiated hPCLS derived from 3 different patients were collected and pooled together for cytokine array. Created with [BioRender.com](https://biorender.com). B. Venn diagram of upregulated cytokines (Fold change 30Gy/0Gy > 1.3) at different points after IR. C. Heatmap of upregulated cytokines in BALF from 5 different Donor and IPF patients (Fold change IPF/Donor > 1.3). D. Heatmap of upregulated cytokines (Fold change 30Gy/0Gy > 1.3) at different points after IR. E. Gene Ontology enrichment analysis of upregulated cytokines at different time points.

response involved in the recruitment of immune cells (day 3) that was followed by the upregulation of interferon-related signaling pathways on day 5 (Fig.4.9E). Then, from day 7, pathways related to immune cell proliferation and activation were enriched as well as pathways involved in the extrinsic regulation of apoptosis (Fig.4.9E). These secretory changes correlate with the upregulated processes showed by Bulk-RNA sequencing analysis.

Then, I focus on cytokines that appeared late after IR, since, at this moment is when I observed a complete senescent phenotype ex vivo. Here, I found that there were only three secreted factors commonly found for both late time points: Transferrin Receptor (TFRC), C-Reactive Protein (CRP), and CRIPTO1 (Fig.4.9B, D). CRIPTO1 is a member of the epidermal growth factor family that participates in development and tumorigenesis. However, not much is known about this protein with aging or in CLDs. Next, I performed a disease ontology enrichment analysis using all the time points to evaluate the medical relevance of our model. This showed the upregulation of pathways linked to interstitial lung disease in all time points (Suppl. Fig.6.3). Therefore, I used the same cytokine array on BALF samples from Donor and IPF patients (Fig.4.9C). Interestingly,

BALF from IPF patients showed increased secretion of some proteins that we also found to be upregulated in our ex vivo model. Namely, angiopoietin-2 (ANGPT-2), cluster of differentiation 14 (CD14), GDF-15, and SDF-1 α (Fig.4.9C). However, I could not detect CRIPTO1 on the BALF samples (Fig.4.9C). In conclusion, the SASP from IR-PCLS is temporally dynamic and is enriched in pro-inflammatory and immunomodulatory factors. Moreover, this approach allowed us the discovery of novel secreted factors that might have a role in aging and pulmonary fibrosis.

4.3 Characterization of radiation-induced fibrotic-like changes in human PCLS

4.3.1 IR-PCLS have an upregulation in pro-fibrotic markers and ECM deposition

Senescent cells accumulate in the lungs of IPF patients and their SASP has been shown to be pro-fibrotic (Aversa et al., 2023; Ptasiński et al., 2021; Schafer et al., 2017). Therefore, I tested whether induction of senescence would lead to an increase in fibrotic-related markers ex vivo. First, I used RT-qPCR to determine the gene expression of well-known markers at 7 dpi. I found an upward trend in the gene expression of GDF-15, COL1A1, alpha-1 Type III Collagen (COL3A1), FN1, and ACTA2 (Fig.4.10A). Moreover, I found a significant increase in TGF- β 1 and PAI-1 gene expression at 7 dpi (Fig.4.10A). Interestingly, I also found a significant upregulation in the gene expression of the novel senescent-related secreted factor: CRIPTO1 (Fig.4.10A). Finally, I also found an enrichment of a publicly available gene set for fibrosis (Liberzon et al., 2015; Liberzon et al., 2011) based on the DEG defined in our model at 7 dpi, although this did not reach statistical significance (Suppl. Fig.6.4).

Then, I used ELISA and IF to evaluate the secretion and expression of ECM-related markers as well as CRIPTO1. Here, I found that IR-PCLS have a tendency to release more PIIINP than the non-irradiated controls (Fig.4.10B), however, protein levels of mature COL3A1 did not change (Fig. 4.10C). Moreover, I observed an upward trend in COL1A1 expression as shown by MFI quantification of IF staining at 7 dpi (Fig. 4.10C). Furthermore, protein levels of CRIPTO1 are significantly increased in IR-hPCLS (Fig. 4.10C, D). However, the secreted levels of CRIPTO1 did not change after IR as shown by ELISA on supernatants at 7dipi (Fig. 4.10B). In conclusion, I found that accumulation of senescence cells in irradiated hPCLS leads to activation of the TGF- β 1 signaling pathway as well as other early pro-fibrotic changes involved in ECM deposition.

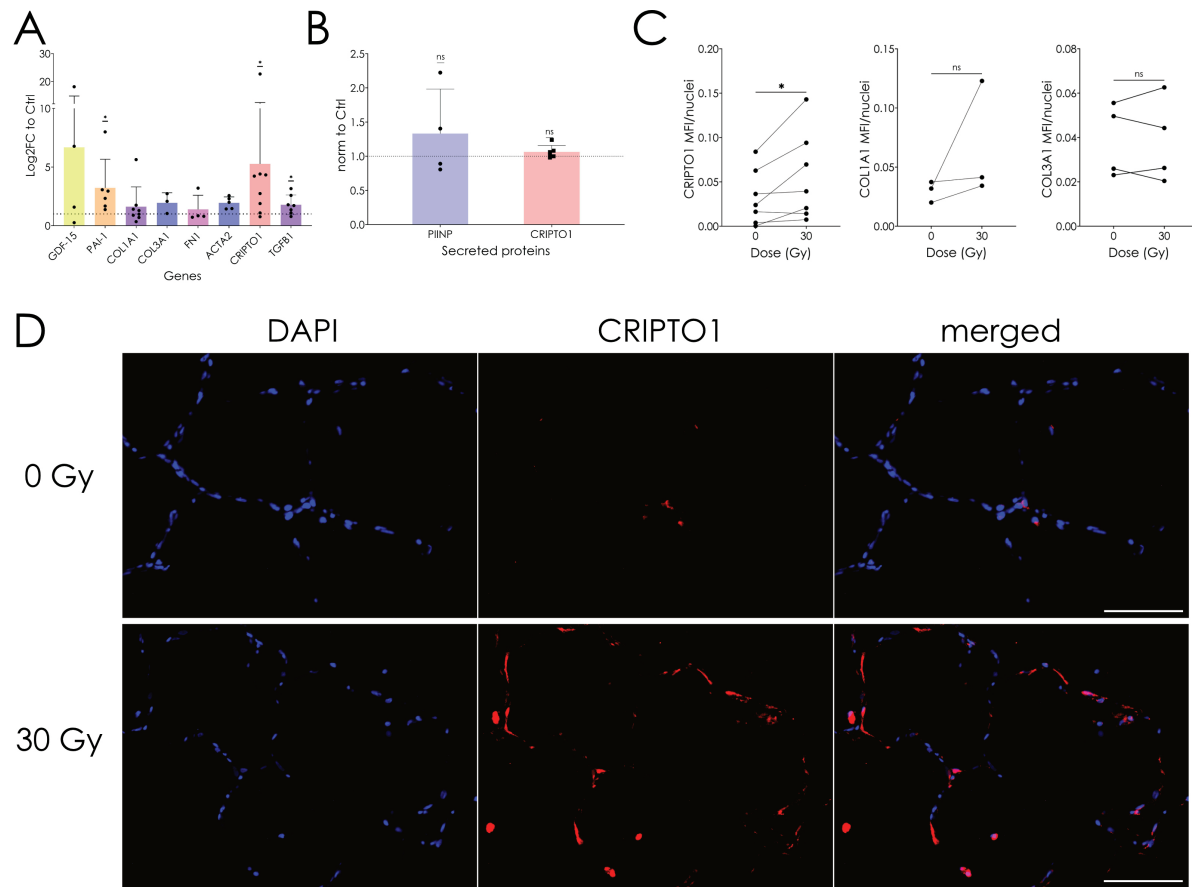


Figure 4.10: Expression of pro-fibrotic markers and ECM deposition in IR-hPCLS. A. Gene expression determined by RT-qPCR of fibrosis-related markers at 7dpi. Means + SD are shown by bars. Data points represent log-2-fold change (Log2FC) normalized to each control from at least 3 independent biological replicates. *p-value< 0.05 after one sample Wilcoxon test. B. ELISA for PIIINP and CRIPTO1 on supernatants from IR-PCLS at 7 dpi. Means + SD are shown by bars. Single points represent protein concentration normalized to control (30Gy/0Gy) from different biological replicates. *p-value< 0.05 after one sample Wilcoxon test. C. Quantification of CRIPTO1 and COL3A1 expression in control and irradiated hPCLS at 7 dpi after IF. Data points represent MFI normalized to nuclei number determined by DAPI from at least 3 independent biological replicates. *p-value< 0.05 after Wilcoxon matched-pairs rank test. D. Representative images of IF for CRIPTO1 on hPCLS at 7 dpi. Scale bar: 50 μ m.

4.4 Pre-clinical testing of senolytics

4.4.1 Senolytics reduce senescence and fibrotic burden in IR-PCLS

Removal of senescent cells has been previously shown to be beneficial and reduce the burden of aging-related diseases like pulmonary fibrosis (Schafer et al., 2017). Therefore, I used senolytics (DQ, and ABT-263) to test the effect of senescent cell depletion ex vivo. For this, human PCLS

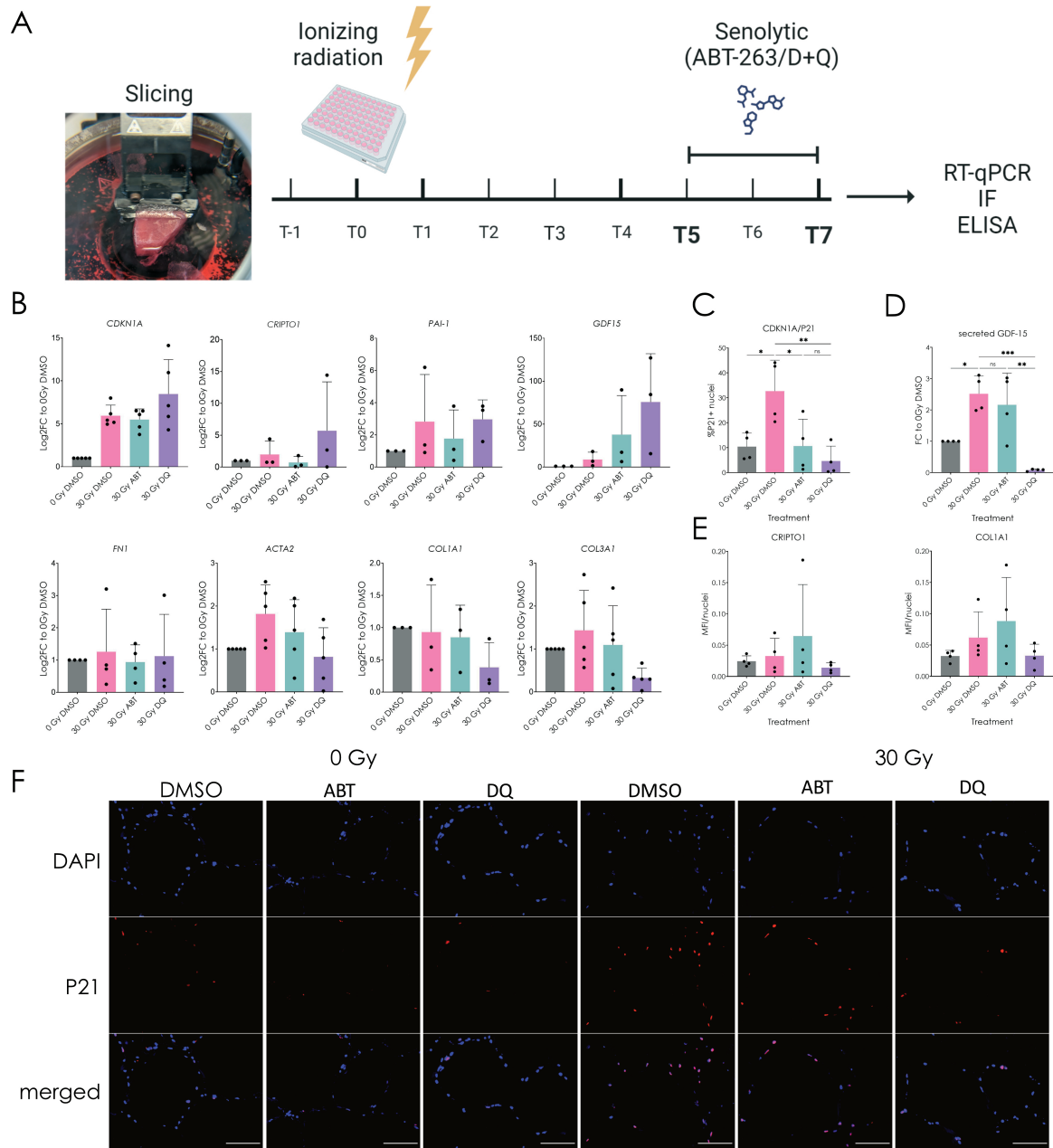


Figure 4.11: Reduction of senescence- and fibrotic-related markers on IR-PCLS after treatment with senolytics. A. Experimental design. PCLS were obtained, irradiated, and cultured for 5 days. Then, senolytic treatment (ABT-263 or DQ) was added for 2 more days. Samples were then used for RT-qPCR, ELISA, and IF. Created with [BioRender.com](https://biorender.com). B. RT-qPCR of senescence- and fibrosis-related markers at 7dpi. C. Immunofluorescence quantification for *CDKN1A*/P21+ nuclei after senolytic treatment. D. Quantification of secreted GDF-15 measured by ELISA in supernatants. E. Mean fluorescence intensity values normalized to nuclei number (DAPI) for *CRYPTO1*, and *COL1A1* after senolytic treatment. Means + SD are shown by bars. Single points represent independent biological replicates (n=3-5). F. Representative images of IF staining for *CDKN1A*/P21 in hPCLS after senolytic treatment. Scale bar: 50 μ m.

were irradiated and at 5 dpi, senolytic treatment was started and kept until 7 dpi (Fig. 4.11A). Irradiated PCLS upregulated gene expression of *CDKN1A*/P21 (Fig. 4.7). Surprisingly, at the transcriptional level, none of the treatments significantly decreased the global expression of *CDKN1A*/P21 in these PCLS (Fig. 4.11B). However, I did observe a significant decrease in *CDKN1A*/P21 protein levels as shown by IF in senescent hPCLS treated with DQ, and ABT-263 (Fig. 4.11C, F).

Then I assessed whether this reduction in *CDKN1A*/P21 expressing cells would modulate the expression of other senescence- and fibrosis-related markers at both transcriptional as well as protein level. Here, I found that the gene expression of the fibrotic markers FN1, ACTA2, COL1A1, and COL3A1 had a downward trend in IR-PCLS (30 Gy) treated with both senolytics, with a stronger effect after DQ (Fig. 4.11B). Moreover, only ABT-263 treatment change gene CRIPTO1 expression, with similar expression levels that the non-irradiated control (Fig. 4.11B). Surprisingly, the expression of GDF-15 and CRIPTO1 was increased by DQ treatment (Fig. 4.11B). Contrary to this, I found that at the protein level, the expression of CRIPTO1 (Fig. 4.11E) and the secretion of GDF-15 (Fig. 4.11D) were only reduced after DQ treatment. The protein levels of COL1A1 also decreased after DQ treatment (Fig. 4.11E). In conclusion, senolytic treatment significantly reduced *CDKN1A*/P21 expression and GDF-15 secretion together with a decreasing trend of pro-fibrotic markers.

4.5 Discovery of potential biomarkers and therapeutic targets

4.5.1 Novel secreted factor CRIPTO1 is pro-fibrotic in hPCLS

Previous results showed a significant increase in the expression of CRIPTO1 in our ex vivo model that shows features of premature aging and early pro-fibrotic changes. Moreover, the expression of CRIPTO1 could be modulated by senolytic treatment. Therefore, I hypothesized that CRIPTO1 could mediate the senescence-induced fibrotic changes we observed in irradiated hPCLS. To test this, human PCLS were prepared, and after 24h, PCLS were treated with recombinant human CRIPTO1 protein. Treatment was replenished every 48h and PCLS were harvested after 4 days (Fig. 4.12A). RT-qPCR showed that CRIPTO1 treatment activated the TGF- β 1 signaling pathway as shown by upregulation of the downstream factor PAI-1 (Fig. 4.12B). Since CRIPTO1 is also a member of the Wnt-signaling pathway (Bianco et al., 2010; Morkel et al., 2003), I evaluated the expression of a downstream protein axis inhibition protein 2 (AXIN2) but the gene expression of this protein was not changed by CRIPTO1 (Fig. 4.12B). This suggests that CRIPTO1 effect is mainly TGF- β 1-mediated. Then, I determined the expression of some of the

fibrotic markers that we found to be upregulated in our model. Here, I found a significant increase in ACTA2 accompanied by an upward trend in the expression of FN1 and COL1A1 (Fig. 4.12B). Finally, CRIPTO1 alone did not induce *CDKN1A*/P21 gene expression ex vivo (Fig. 4.12B). In conclusion, I found that the SASP-related factor CRIPTO1 has a pro-fibrotic effect in hPCLS that activates the TGF- β 1 signaling pathway, as previously observed in IR-hPCLS.

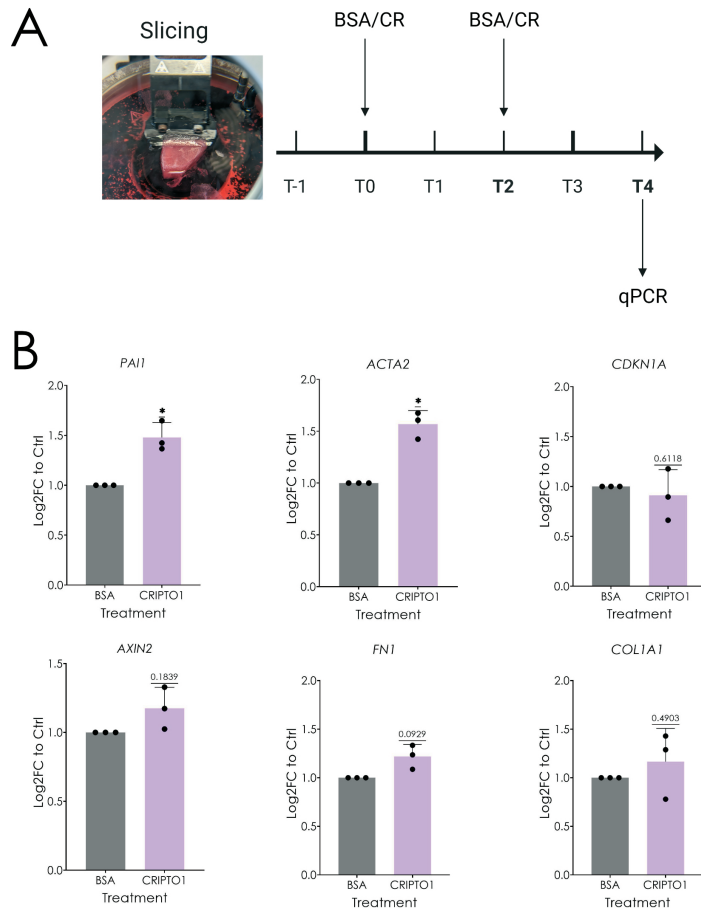


Figure 4.12: Assessment of pro-fibrotic changes after CRIPTO1 treatment on hPCLS. A. Experimental design. hPCLS were obtained and after 24h treated with BSA or CRIPTO1 (100ng/ml). After 2 days treatment was replenished and samples were collected for RT-qPCR after 2 more days. Created with [BioRender.com](https://biorender.com). B. RT-qPCR to evaluate gene expression of senescence- and fibrosis-related markers at day 4 post-treatment. Single points represent Log2Fold-change normalized to control from independent biological replicates (n=3). *p-value< 0.05 after one sample t-test.

4.5.2 Novel secreted factor CRIPTO1 activates primary lung fibroblasts in vitro

Preliminary data using primary alveolar epithelial cells showed an upregulation in CRIPTO1 gene expression after IR (Data not shown). Moreover, I observed that the alveolar epithelium

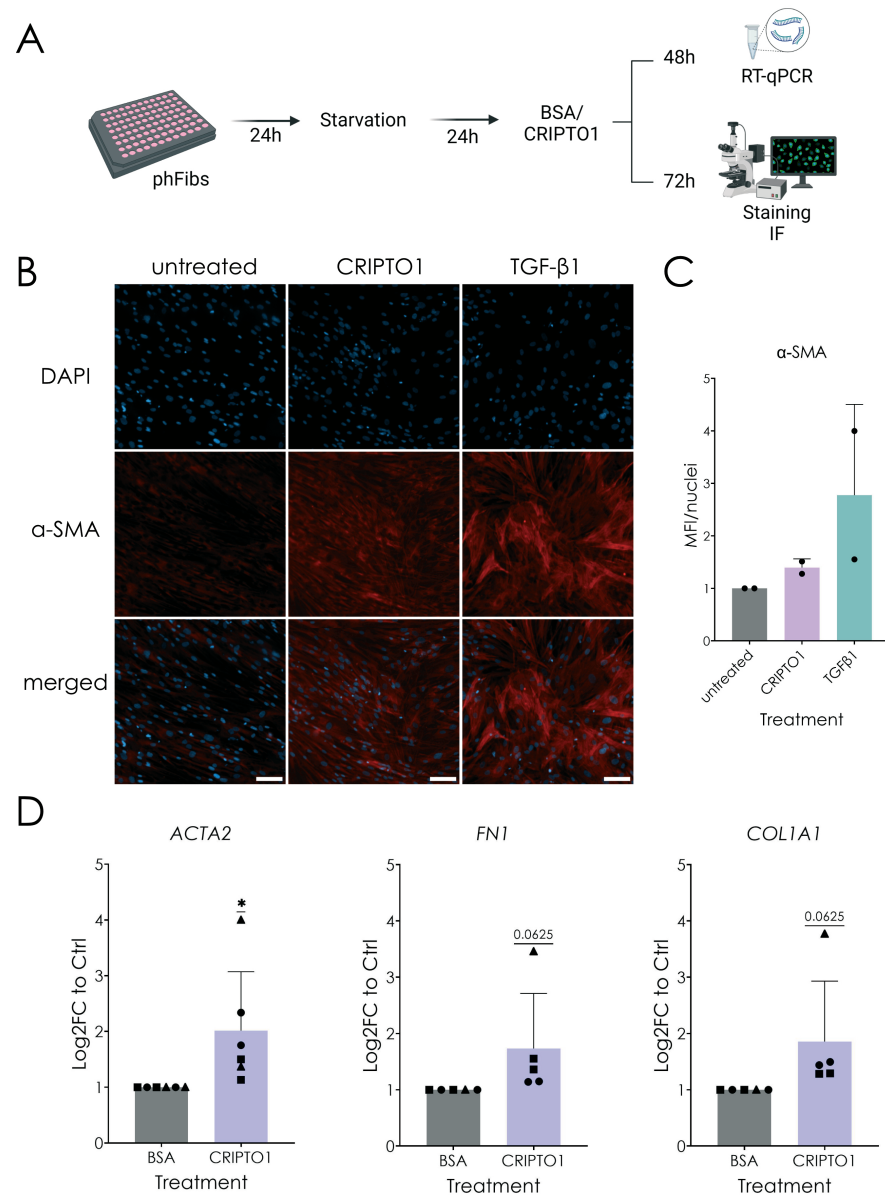


Figure 4.13: Assessment of pro-fibrotic changes after CRIPTO1 treatment on primary human lung fibroblasts. A. Experimental design. Primary human lung fibroblasts were seeded, starved, and treated with BSA or CRIPTO1 (100ng/ml). Samples from 6-wells were collected after 48h for RT-qPCR. 96-well plates were used for transdifferentiation assay, in which after 72h of treatment cells were fixed and stained for ACTA2. Created with [BioRender.com](https://biorender.com). B. Representative images of transdifferentiation assay. Scale bar: 100 μ m C. Quantification of MFI normalized to cell number (DAPI). Means + SD are shown by bars. Single points represent the average of 3 technical replicates from independent biological replicates (n=2). D. RT-qPCR to evaluate gene expression of ACTA2, FN1 and COL1A1 after 48h. Means + SD are shown by bars. Single points with different shapes represent independent biological replicates (n=3). Points with the same shape represent technical replicates done with different passages of the same pHLF donor.

expressed CRIPTO1 in irradiated hPCLS (Fig. 4.10). Therefore, I hypothesized that the upregulation of CRIPTO1 on the epithelium might promote fibroblast activation, leading finally to the upregulation of the pro-fibrotic markers observed in our model. Therefore, a transdifferentiation assay was used to determine the expression of ACTA2 after 72h of CRIPTO1 treatment in comparison to the negative (BSA) and positive (TGF- β 1) controls (Fig. 4.13A). Here, I found an increase in ACTA2 expression in comparison to the negative control but the effect was smaller than the observed after TGF- β 1 treatment (Fig. 4.13B, C). Moreover, I treated phLF with CRIPTO1 for 48h and assessed gene expression by RT-qPCR (Fig. 4.13A). Here, I found a significant increase in ACTA2 (Fig. 4.13D), as observed in the whole tissue treatment. Moreover, FN1 and COL1A1 expression was also upregulated although this did not reach statistical significance (Fig. 4.13D). In conclusion, the SASP-related factor CRIPTO1 induces activation of phLF leading to increased ACTA2 expression.

Chapter 5

Discussion

Senescent cells have an important role in homeostatic tissue regeneration, development, and tumor suppression (Basisty et al., 2020; Kumari and Jat, 2021). However, during aging and in chronic lung diseases, senescent cells accumulate, promoting inflammation and hampering tissue regeneration (Basisty et al., 2020; Bramey et al., 2023; Kumari and Jat, 2021). Therefore, the characterization and classification of senescent cells have become very relevant in the last years. Furthermore, understanding how senescent cells modulate their microenvironment in homeostasis and disease is of vital importance to being able to target pathogenic senescence as a therapeutic application for CLDs. Previous studies, performed on specific cell types *in vitro* or in animal models, have shown that senescence can be artificially induced after exposure to DNA-damaging agents like ionizing radiation (Campisi and d'Adda di Fagagna, 2007; Coppé et al., 2008; Di Micco et al., 2021), reactive oxygen species or bleomycin (Bramey et al., 2023). In the lung, IR-induced cellular senescence promotes a chronic inflammatory response that in some cases leads to pulmonary fibrosis (Beach et al., 2017). Similarly, the natural accumulation of senescent cells with aging has been linked to the onset and progression of IPF (Aversa et al., 2023; Ptasiński et al., 2021; Schafer et al., 2017). Therefore, current drug development has been focused on targeting senescent cells with senolytics or modulating their pro-inflammatory SASP using senomorphics (L. Zhang et al., 2023). Early-phase safety studies have shown some benefits after senolytic treatment in IPF patients (Justice et al., 2019; Nambiar et al., 2023). However, the current accepted and used therapies for pulmonary fibrosis remain nintedanib and pirfenidone, which unfortunately only slow down disease progression but do not stop the fibrotic process or reverse the induced tissue damage (Flaherty et al., 2019; King et al., 2014). Therefore, the development of novel models to study the pathobiology of IPF and discover additional therapeutical options have gained importance. In this regard, this project aimed to establish a clinically relevant human

ex vivo of premature aging by exposing hPCLS to ionizing radiation. In this way, I hypothesized that the accelerated aging caused by IR would lead to pro-fibrotic changes ex vivo. Furthermore, this model should serve as a platform for biomarker discovery and pre-clinical testing of current and novel therapies for age-related lung diseases such as pulmonary fibrosis.

5.1 Induction of cellular senescence in lung tissue ex vivo

Models to study the role of cellular senescence in pulmonary fibrosis have been mainly developed *in vitro*, using specific single cell types, or *in vivo* using mouse models. Here, I present for the first time a human ex vivo model of radiation-induced cellular senescence using PCLS. Given the complex composition of the lung with more than 40 different cell types (Adams et al., 2020), PCLS offer a unique opportunity to study the response to injury at global (tissue) and local (cell) levels. However, this also means that any treatment has to be adjusted according to specific cellular susceptibilities. For example, previous studies have shown that lung fibroblasts become senescent after exposure to just 5 Gy (Mukherjee et al., 2021), however, exploratory experiments from our group using primary lung epithelial progenitors, revealed that these cells need higher doses (above 60 Gy) to undergo senescence (data not shown). Therefore, to establish our models, I tested DNA damage induction, metabolic activity, and cytotoxicity after exposure to doses of IR ranging from 30 Gy to 120 Gy in both murine and human PCLS. Here, I found that 30 Gy were sufficient to induce a DDR based on γ H2Ax detection (early as 1 h after IR) without this being cytotoxic or significantly reducing metabolic activity of the primary lung tissue. Moreover, γ H2Ax expression was homogeneously distributed in the whole lung tissue, suggesting that with this dose different cell types were targeted. Transcriptomics analysis revealed that at 7 dpi, irradiated hPCLS have a very distinct phenotype when compared to non-irradiated controls, characterized by up-regulation of pathways related to inflammation and DNA damage response. Moreover, IR-hPCLS down-regulate pathways involved in mitotic cell cycle progression and cell division. Finally, genes involved in the activation of T cells and the negative regulation of immune cell proliferation were also upregulated after 7 dpi. This together indicated global transcriptional changes in human PCLS after IR that are linked to cellular senescence. This was also confirmed by enrichment analysis using publicly available senescence-related gene sets.

Therefore, classical hallmarks of cellular senescence were evaluated in our models (González-Gualda et al., 2021). First, the gene expression of the cell cycle inhibitors *CDKN1A*/P21 and *CDKN2A*/P16 was assessed by RT-qPCR. IR-PCLS showed a significant upregulation of *CDKN1A*/P21, whereas the expression of *CDKN2A*/P16 was not significantly changes. This cor-

relates with recent studies that have shown that *CDKN1A*/P21 is the main driver of IR-induced senescence (A. Chandra et al., 2022). Moreover, it is important to remark that these two cell cycle inhibitors have distinct temporal functions, *CDKN1A*/P21 being important for senescence induction while *CDKN2A*/P16 has a role in sustaining senescence in the long term (W. Huang et al., 2022; Kumari and Jat, 2021). Since IR-PCLS were cultured for 7 dpi, significant up-regulation of *CDKN2A*/P16, to sustain permanent senescence, might occur later in our models. Next, the induction of SA- β -gal after IR was assessed. Classical biochemistry-based detection and quantification of SA- β -gal is commonly used to identify senescent cells *in vitro* (Bramey et al., 2023). However, this approach was very challenging for lung explants given the 3D structure and the technical limitations related to the low optical resolution of bright-field microscopy for PCLS. Therefore, I established an *ex vivo* detection method based on the fluorogenic probe SPiDER- β -gal, in which SA- β -gal (active at pH 6 in senescent cells) can be selectively detected after inhibition of the acidic β -galactosidase activity (pH 4) with BafA1. Despite a high variability, I observed an upward trend in SA- β -gal activity in our models after IR, further validating the induction of a senescent phenotype. Finally, a cytokine array was used for an unbiased characterization of the SASP in IR-PCLS. Here, a specific SASP was found for each species with only two common cytokines (MPO and IFN γ). This could be explained by inter-species differences in the SASP composition described by other authors in the past (Basisty et al., 2020). Several senescence-related cytokines such as IL-6 or CXCL1 were identified in supernatants from murine IR-PCLS. hPCLS showed increased secretion of TNF-a, THBS1, and CXCL11, which have also been previously linked to cellular senescence (Maciel-Barón et al., 2016; Meijles et al., 2017; Pan et al., 2017). Moreover, ELISA-based protein quantification showed a significant upregulation in the secretion of GDF-15 by IR-hPCLS at 7 and 9dpi. GDF-15 has been shown to be mainly secreted by senescent lung epithelial cells (Y. Zhang et al., 2019), again validating the induction of cellular senescence after exposure to IR in our models. Unbiased secretome analysis based on cytokines arrays is a good option to initially described changes in the SASP composition. However, it is a semi-quantitative approach and the detected cytokines are limited to the commercially available panels. In conclusion, I showed for the first time that IR induces a senescent phenotype in the lung *ex vivo* and that the core hallmarks of senescence are preserved among different species with differences in the SASP composition.

5.2 Identification of the main senescent cellular compartments in IR-hPCLS

Several cellular and molecular changes have been described and used as a guide for the identification of senescent cells (González-Gualda et al., 2021). However, it is still challenging to

characterize and study senescence given its heterogeneity and the low prevalence of senescent cells *in vivo* (Gasek et al., 2021; Tang et al., 2019; Wiley et al., 2017). Therefore, there is a need for systems in which traditional canonical senescence markers can be detected and combined with readouts that add spatial resolution at a single-cell level. Therefore, we used IR to simultaneously target several cell types present in PCLS and characterize their response in their natural 3D localization and cellular niche. Then, IF or flow cytometry was used to identify the main senescent cellular compartments in our novel models. Flow cytometry-based quantification of fluorescent SA- β -gal in single suspensions from murine PCLS revealed enrichment of senescent cells in the epithelial compartment (EpCAM+) in comparison with the immune (protein tyrosine phosphatase receptor type C (CD45)+) or the mesenchymal (cluster of Differentiation 90 (CD90)+) compartments (data not shown). For this reason, control and irradiated human PCLS were co-stained *in situ* for the canonical senescence marker *CDKN1A/P21* and cell-specific markers for mesenchymal (ACTA2) cells and alveolar epithelial populations: AT1 (PDPN+) and AT2 (SFTPC+) cells. Here, I found that mainly distal epithelial cells had a senescent phenotype in IR-PCLS as shown by high levels of γ H2Ax and *CDKN1A/P21* in AT2 cells. Since senescent AT2 cells have been shown to accumulate in IPF lungs and display features of stem cell dysfunction, I evaluated whether the stem cell progenitor capacity of the distal lung epithelium was altered in IR-hPCLS. Indeed colony formation efficiency and organoid size were significantly reduced in epithelial progenitors derived from senescent PCLS. Interestingly, preliminary characterization of these organoids, showed that the single or clustered cells derived from IR-hPCLS displayed high levels of *CDKN1A/P21* and γ H2Ax. This all together correlates with previous studies that showed that AT2 cells are the main susceptible cell type in the lung to undergo IR-induced cellular senescence (Pan et al., 2017) and have a reduced stem progenitor capacity linked to high levels of *CDKN1A/P21* expression (Lv et al., 2022). In conclusion, IR induces a distal epithelial senescent phenotype in PCLS, mimicking the accumulation of senescent and dysfunctional stem cell progenitors described as main drivers of RIPF and IPF pathogenesis (Lv et al., 2022; Zhou et al., 2022).

5.3 Characterization of senescence-induced pro-fibrotic signaling in IR-hPCLS

Together with the intrinsic cellular changes that cells undergo with senescence, senescent cells also secrete a complex and highly dynamic combination of growth factors, chemokines, and cytokines (SASP) that define their beneficial or detrimental role in their micro-environment (Basisty et al., 2020; Deursen and M, 2014). Therefore, using again an unbiased approach the SASP from human senescent PCLS was longitudinally characterized with cytokine arrays. In this way, as previously

described (Hernandez-Segura et al., 2017), profound temporal changes were found in SASP profile of senescent hPCLS with a small overlap in the secreted factors across all the time points tested. The early SASP (Day3-5) was predominantly composed of cytokines related to stress response, inflammation, and chemotaxis. The late SASP (Day7-9) included secreted factors involved in the activation of the adaptive immune response. As shown above, IR-hPCLS displayed a full senescent phenotype from day 7, characterized by increased secretion of GDF-15, a cytokine mainly secreted by senescent epithelial cells in the lung (Y. Zhang et al., 2019). Therefore, I was interested in determining other secreted factors that appeared to be shared between day 7 and day 9. Here, I only found three common secreted factors: TFRC, a receptor involved in receptor-dependent iron uptake, CRP, a member of the pentraxin family involved in complement activation in response to tissue injury and inflammation, and CRIPTO1, an epidermal growth factor-related protein mainly involved in development and tumorigenesis. Although little is known about these factors in pulmonary fibrosis, a gene set enrichment analysis showed that the SASP from senescent hPCLS was enriched in interstitial lung diseases. Therefore, I compared the secreted factors present in BALF samples from donor and IPF patients with the SASP from IR-hPCLS. Here, I could confirm that next to GDF-15, which has been shown to have a pro-fibrotic activity related to the activation of fibroblasts and M2 macrophages (Radwanska et al., 2022; Takenouchi et al., 2020), other secreted factors increased in IR-hPCLS such as CD14, Angiopoietin 2 (ANGPT2), and SDF-1 α are also upregulated in BALF samples from IPF patients. This demonstrates that the senescence phenotype induced by IR in our model recapitulates some of the pro-fibrotic signaling found in IPF.

To further characterize the senescence-induced pro-fibrotic changes *ex vivo*, the gene expression of well-known fibrotic markers as well as of the novel senescence-related secreted factor (CRIPTO1) was assessed by RT-qPCR. Here, I found a significant upregulation of the fibrotic markers TGF- β 1 and PAI-1. Moreover, there was an increasing tendency in the expression of other well-known ECM-related markers described in fibrotic lungs ((Pan et al., 2017; Schafer et al., 2017)) such as ACTA2, FN1, COL3A1, and COL1A1. Confirming the secretome results, the gene expression of GDF-15 also showed an upward trend in IR-PCLS. Next, I used ELISA to determine the secretion of a marker involved in collagen synthesis and deposition: PIIINP. Here, I observed an increased release of PIIINP in supernatants from human IR-PCLS, although this effect did not reach statistical significance. Interestingly, the protein expression of the mature COL3A1 did not change after IR. This might indicate that our model resembles early steps in fibrosis pathogenesis since PIIINP is an intermediate product from the conversion of type III pro-collagen to the mature COL3A1 form and high levels of PIIINP has been found in BALF samples from IPF patients (Su et al., 2017). In conclusion, IR induces early pro-fibrotic changes in human lung explants, which can be used to discover novel secreted factors involved in senescence-mediated fibrotic changes.

5.4 Discovery of a novel senescence-related secreted factor with pro-fibrotic activity in the lung

Given the limited availability of IPF derived tissue and the fact that these samples already represent an end stage of the disease, the development of disease-relevant human models is very important for biomarker and drug discovery. In this study, I present a novel human *ex vivo* model that recapitulates features of premature aging and early fibrotic changes. Moreover, this model led to the discovery of a novel secreted factor that is upregulated in premature aged hPCLS and might have a role in the pathogenesis of pulmonary fibrosis. CRIPTO1 is a GPI-anchored epidermal growth factor that is found both in the cellular membrane as well as a secreted protein (Karkampouna et al., 2021). It is involved during early development and usually is silenced postnatally (Karkampouna et al., 2021). However, the expression of this protein has been shown to be reactivated in several cancer types (Karkampouna et al., 2021), in which it mainly promotes epithelial–mesenchymal transition (EMT) of epithelial cells (Arnouk et al., 2021; Karkampouna et al., 2021). Notably, CRIPTO1 is part of different signaling pathways such as Wnt and TGF- β 1 (Bianco et al., 2010; Morkel et al., 2003), which are known to be aberrantly activated in senescence and pulmonary fibrosis (Degryse et al., 2011; Lehmann et al., 2020; Selman et al., 2008). Moreover, a recent study showed that CRIPTO1 expression is upregulated in liver and heart fibrosis (Karkampouna et al., 2021), however, little is known about its role in the pathogenesis of pulmonary fibrosis.

Since our results revealed an increased secretion and expression of CRIPTO1 after IR and senolytic treatment showed a reduction in this and other fibrotic markers, I hypothesized that CRIPTO1 could mediate the senescence-related pro-fibrotic changes observed in our model. To test this, I treated hPCLS with recombinant CRIPTO1 protein for 4 days. Then, the gene expression of proteins downstream of the Wnt- and the TGF- β 1-signaling pathways was determined. Here, a significant induction of PAI-1 gene expression was observed, suggesting that CRIPTO1 activity observed *ex vivo* might be mediated via TGF- β 1-signaling. This is also supported by the significant upregulation of TGF- β 1 and PAI-1 observed in IR-hPCLS. PAI-1 is a well-known pro-fibrotic protein and its down-regulation was linked to decreased expression of ACTA2 in fibroblasts thereby reducing interstitial fibrosis in the kidney (L. Yao et al., 2019). Moreover, PAI-1 has been shown to be upregulated in both AT2 cells and lung fibroblasts with age and to be implicated in the modulation of apoptosis-resistance phenotype involved in the pathogenesis of IPF (Jiang et al., 2021). Therefore, I also assessed the expression of ACTA2 and other pro-fibrotic markers found to be upregulated in irradiated hPCLS after CRIPTO1 treatment. Notably, CRIPTO1 treatment significantly increased the gene expression of ACTA2 and induced an upward trend for COL1A1 and FN1 gene expression, supporting again a link between CRIPTO1

and fibroblast activation in the lung.

IF showed that CRIPTO1 is mainly expressed in the alveolar epithelium in hPCLS and exploratory experiments revealed that irradiated primary alveolar epithelial cells also increase CRIPTO1 gene expression after 7 days of culture (data not shown). Therefore, I hypothesized that IR-induced senescence upregulates the secretion of CRIPTO1 by the alveolar epithelium thereby promoting fibroblast activation. To test this, phLF were treated with recombinant CRIPTO1, and the gene expression of markers linked to fibroblast activation was evaluated. Accordingly with the phenotype observed in the whole lung, CRIPTO1 treatment significantly upregulated ACTA2 phLF. Moreover, the expression of other markers (FN1 and COL1A1) related to fibroblast activation were also upregulated, although this did not reach statistical significance yet. Finally, a trans-differentiation assay based on IF, also showed an upward trend in ACTA2 expression after CRIPTO1 treatment on phLF. Further experiments will be performed to expand these observations using PCLS and other primary cells, given that due to limited tissue availability this could not be performed yet. In conclusion, our human ex vivo model of premature aging allowed the discovery of a novel secreted factor that seems to be involved in senescence-mediated pro-fibrotic changes in the lung and could serve as a potential biomarker or therapeutical target for IPF.

5.5 Pre-clinical testing of senolytics to target senescence-induced pro-fibrotic signaling in IR-hPCLS

The lung is a unique organ that undergoes several structural and cellular changes with aging (Meiners et al., 2015). Among them, cellular senescence is a common feature found in both chronological aging as well as after exposure to chronic damage related to the pathogenesis of CLDs such as IPF (Aghali et al., 2022; Aversa et al., 2023; Meiners et al., 2015; Ptasiński et al., 2021; Schafer et al., 2017). Upon damage, AT2 are the main stem cells in the distal lung responsible for the regeneration of the epithelial lining by proliferating and differentiating into AT1 cells (Barkauskas et al., 2013; Lehmann et al., 2020; C. Yao et al., 2019). Recent studies have shown that in IPF, AT2 cells failed to differentiate into AT1 and instead enter an intermediate state known as aberrant basaloid cells. These cells display gene signatures characteristic of basal cells together with mesenchymal markers and are localized near myofibroblasts foci in IPF lungs (Adams et al., 2020; Habermann et al., 2020). Interestingly, these cells also upregulate classical markers of cellular senescence such as *CDKN1A/P21*, *CDKN2A/P16*, and GDF-15 and secrete pro-inflammatory and pro-fibrotic mediators such as TGF- β 1. Therefore, the persistence of this senescent and activated epithelial cell population has been proposed as a driver of impaired alveolar regeneration and myofibroblast activation observed in IPF lungs (Adams et al., 2020; Khan et al., 2022). However, cellular senescence also has beneficial roles during homeostatic tissue

repair. In this way, signals from the injured epithelium activate fibroblasts, which upregulate ACTA2 expression, proliferate, and secrete ECM components until the wound is healed. Once this happens, myofibroblasts undergo senescence reducing ECM secretion and thereby, limiting fibrosis (Lin and Xu, 2020). However, in IPF these senescent myofibroblasts accumulate in the distal lung promoting aberrant ECM deposition and perpetuating pro-fibrotic signaling in the lung (Bramey et al., 2023; Schafer et al., 2017). This dual role of cellular senescence highlights the importance of understanding how good and bad senescence occurs in the lung and how only the pathogenic cellular senescence can be targeted as a therapeutical option for IPF.

hPCLS have been used to model early molecular and cellular changes linked to pulmonary fibrosis, for example, by exposing them to a fibrotic cocktail composed of pro-fibrotic and inflammatory cytokines (Alsafadi et al., 2017). Despite the increase in some fibrotic-related markers and epithelial reprogramming observed in this model, the role of cellular senescence or other age-related changes in the onset of those fibrotic changes was not specifically addressed. In the present study, we established for the first time a human system that combines both features of premature aging as well as activation of fibrotic pathways like TGF- β 1. However, contrary to fibrotic cocktail-treated hPCLS (Alsafadi et al., 2017), we did not observe a strong deposition of COL1A1 or COL3A1 but initial changes of collagen biogenesis as shown by the higher release of PIIINP. ECM deposition induced by IR has been described to occur after several weeks in animal models of pulmonary fibrosis and has been linked to an active immune response after injury (Beach et al., 2017). Therefore, longer culturing times or co-culture with circulatory immune cells could be used to enhance collagen deposition in IR-hPCLS. Interestingly, our novel human ex vivo model shows a significant increase in senescence markers (*CDKN1A/P21*, GDF-15) in the distal epithelium along with markers related to epithelial reprogramming as shown by strong upregulation of KRT17, downregulation of EpCAM, and stem cell dysfunction of the distal lung progenitors. All these features have been linked to the pathogenic role of cellular senescence in the aged and diseased lung (Aghali et al., 2022; Aversa et al., 2023; Ptasinski et al., 2021; Schafer et al., 2017) and therefore, this model offers a novel platform based on the human system to study mechanisms involved in senescence-induced fibrotic changes, discover novel biomarkers and test potential new drugs for IPF.

Therefore, I used this novel platform to evaluate whether targeting senescent cells with senolytics would lead to a reduced fibrotic burden ex vivo. For this, senescent hPCLS were treated with DQ and ABT-263 for 48 h. Here, I found that both treatments significantly reduced *CDKN1A/P21* protein levels in IR-hPCLS, as previously described for aged human and murine lung tissue (Cho et al., 2023; Hickson et al., 2019; Kirkland and Tchkonia, 2020; Zhu et al., 2015). These results also correlate with previous data showing that ABT-263 decreases *CDKN1A/P21* expression in a mouse model of radiation-induced lung injury (RILF) (Pan et al., 2017). Moreover, the secretion

of the senescence-related and pro-fibrotic marker GDF-15 was significantly reduced after DQ treatment as previously shown in mice (Thadathil et al., 2022). Surprisingly, RT-qPCR showed an upward trend in the gene expression of GDF-15 after senolytic treatment in IR-PCLS. This could indicate that in this context senolytics do not reduce gene expression but might modulate post-transcriptional modifications involved in the secretion of GDF-15. Notably, confirming previous findings on fibrotic PCLS (Lehmann et al., 2017; Schafer et al., 2017), I observed a decreasing tendency in the gene expression of all tested fibrotic markers after senolytic treatment when compared with premature aged hPCLS. Moreover, at the protein level, DQ treatment decreased CRIPTO1 expression in IR-PCLS. Interestingly, DQ treatment showed a stronger effect than ABT-263 in the negative modulation of fibrotic markers. These differences in effectiveness could be partially explained by the working mechanisms of these senolytic treatments. For example, the senolytic effect of ABT-263 relays on the upregulation of several BCL-2 family members (Vogler et al., 2009) whereas DQ targets both the BCL-2 as well as Src kinases (Belsches-Jablonski et al., 2001). This could, for instance, allow DQ to target multiple populations of senescent cells in comparison with ABT-263. This would lead to a shift in the cellular composition after treatment due to the removal of certain senescent populations showing unexpected changes in the global gene expression. Therefore, future studies including single-cell transcriptomics could be used to further elucidate which senescent populations are depleted by ABT-263 and DQ and for example, improve currently available therapies to target specific senescent populations.

In conclusion, our novel ex vivo human model resembles senescence-mediated fibrotic changes that can be reversed by senolytic treatment. Moreover, DQ treatment also modulated the expression of the novel potential biomarker, CRIPTO1. This might indicate that the upregulation of fibrotic markers observed in our ex vivo model is partially mediated by the accumulation of senescence cells and their elevated CRIPTO1 expression. However, a comprehensive transcriptomic analysis after senolytic treatment ex vivo as well as experiments to specifically target CRIPTO1, will provide a better understanding of the mechanism behind CRIPTO1 increased expression by senescent cells and the fibrotic changes observed in our model. Further experiments to evaluate the expression of CRIPTO1 in blood or lung tissue on IPF or RILF patient cohorts and its modulation after senolytic or antifibrotic therapy could help to establish this as a biomarker relevant for clinical applications. On top of this, this model can be used to test the efficacy of other compounds based on transcript and protein changes as shown in this study for two already known senolytics: ABT-263 and DQ.

5.6 Limitations and conclusions

As shown in this study, PCLS offer a unique opportunity to study cellular processes in the native 3D structure and cellular composition of the human lung. However, scientists in this field

still face some practical and technical challenges in their usage. On the practical side, human lung tissue is very scarce, and therefore, there is a need for optimizing sample preparation and collection for low and medium-throughput applications. In this project, tissue availability had strong temporal fluctuations linked among other factors to the COVID-pandemic, which limited the planning and performance of the different experiments. Therefore, prioritization of some experiments needed to be done in order to address all the milestones proposed initially. From the technical point of view, most of the traditional and novel functional methods for senescence characterization were not previously established for PCLS in our institute, therefore, initially, this project focused on developing and validating these methods for our *ex vivo* models. Moreover, optimization of tissue usage was done, for example, by adjusting the amount of tissue needed for readouts such as RT-qPCR or bulk-RNA. This allowed us to study the effect of different treatments or perform longitudinal analysis. However, this also led to a small sample size for some readouts, which together with the intrinsic high variability linked to the work with primary tissue, limited the statistical power of the downstream analysis. This highlights the importance of standardizing the preparation, culture, treatment, and downstream readouts to establish PCLS as a high-throughput platform for drug discovery and testing. Moreover, the validation of these results on other patient cohorts or clinical samples such as blood or fixed lung tissue from IPF patients together with adjustment for patient-derived variables such as age, smoking history, or gender, could help to extrapolate our findings for clinical applications.

Despite technical limitations linked to the usage of primary human tissue, this study addressed all the milestones presented initially and future plans will be focused on understanding the role of the novel secreted factor CRIPTO1 in IR-induced senescence and fibrosis in the lung and its application as a clinical biomarker. For this, mechanistic studies evaluating upstream and downstream regulation of CRIPTO1 in specific cell types such as the alveolar epithelium, circulatory immune cells, or fibroblasts will be expanded. For example, by treating these cells with CRIPTO1 or inhibiting CRIPTO1 activity *in vitro*. Moreover, future steps include the optimization of detection methods for CRIPTO1 in clinical samples. Furthermore, we are currently using state-of-art technologies such as single-nuclei transcriptomics to better characterize the cellular heterogeneity of the senescence phenotype induced in our model and to extrapolate our findings to available transcriptomics atlases for the aged and diseased lung. Finally, we will use untargeted metabolomics from both tissue and PCLS supernatants to validate the premature aging in our model to the changes observed during aging and in IPF.

In summary, this study presents a novel human *ex vivo* model that recapitulates features of premature aging such as increased epithelial senescence, reduced stem cell capacity, and dysregulated immune activation. Moreover, the accumulation of senescent cells after IR induced early fibrotic changes related to ECM deposition and secretion of pro-fibrotic factors, which could be reversed

by senolytics treatment. Finally, this model allowed the discovery of a novel senescence-induced factor with pro-fibrotic activity in whole lung tissue and primary lung fibroblasts that could be potentially used as a biomarker for pulmonary fibrosis.

Chapter 6

Supplementary Material

6.1 Supplementary Figures

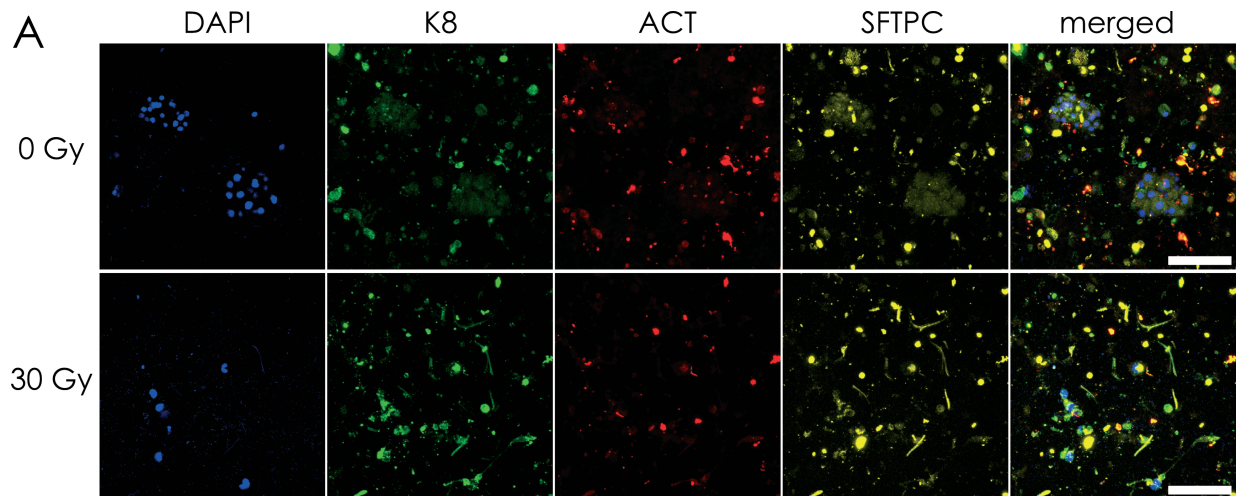


Figure 6.1: Immunofluorescence of hPCLS-derived organoids.. A. Representative confocal images from single organoids from control and irradiated hPCLS. Organoids were fixed with Methanol and stained for typical markers for AT2 cells (SFTPC), transitional AT2 cells (K8), and airway epithelial cells (ACT).

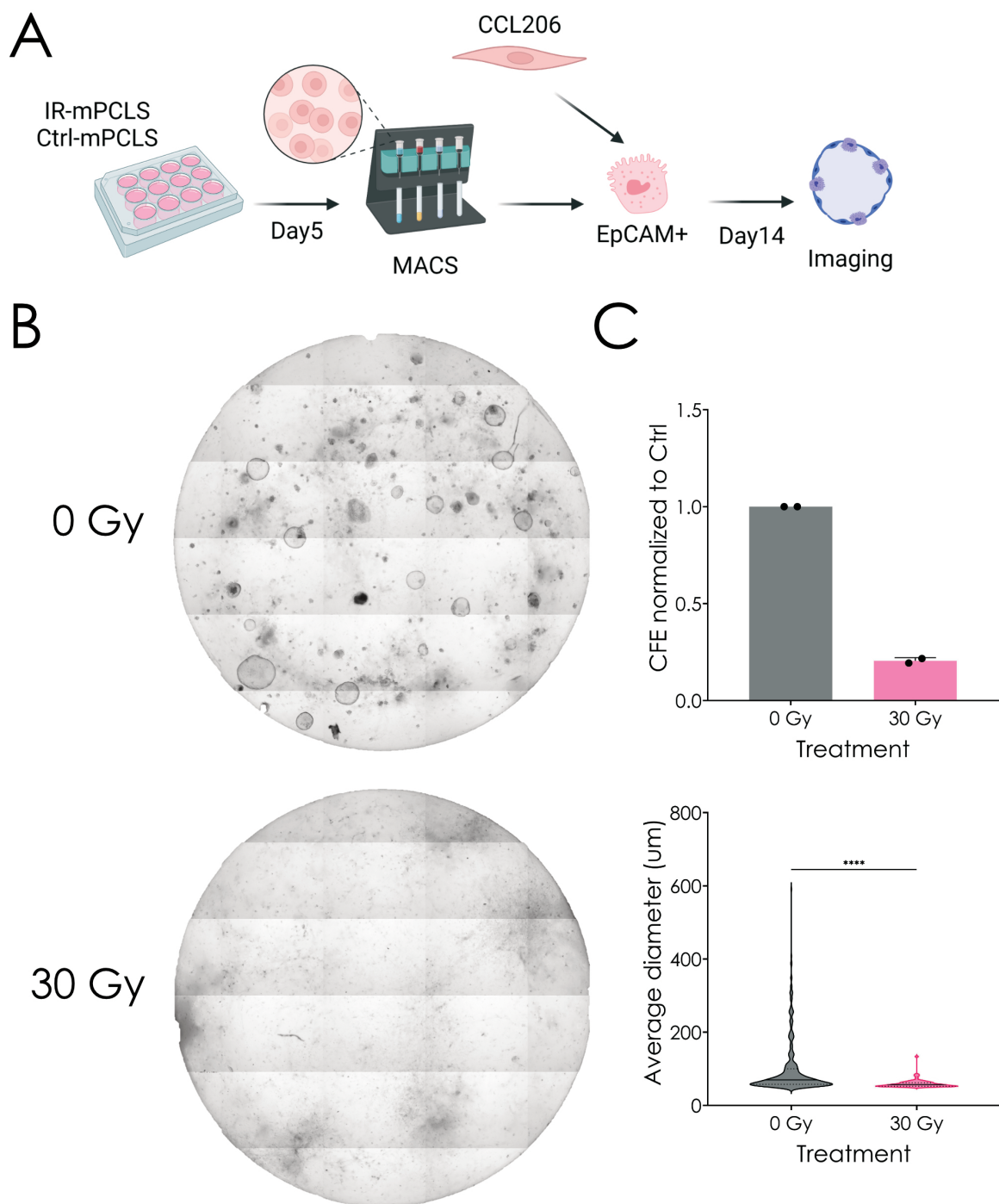


Figure 6.2: Organoid assay from mPCLS. A. Experimental design. Mouse PCLS were generated and irradiated. After 5 days, a single cell suspension was prepared and EpCAM+ cells were isolated by MACS sorting. These cells were then co-cultured with CCL206 lung fibroblasts for 14 days in an organoid assay. Created with [BioRender.com](https://biorender.com). B. Representative bright-field images. C. Colony formation efficiency (CFE) and organoid size at day 14. Single points represent biological replicates.

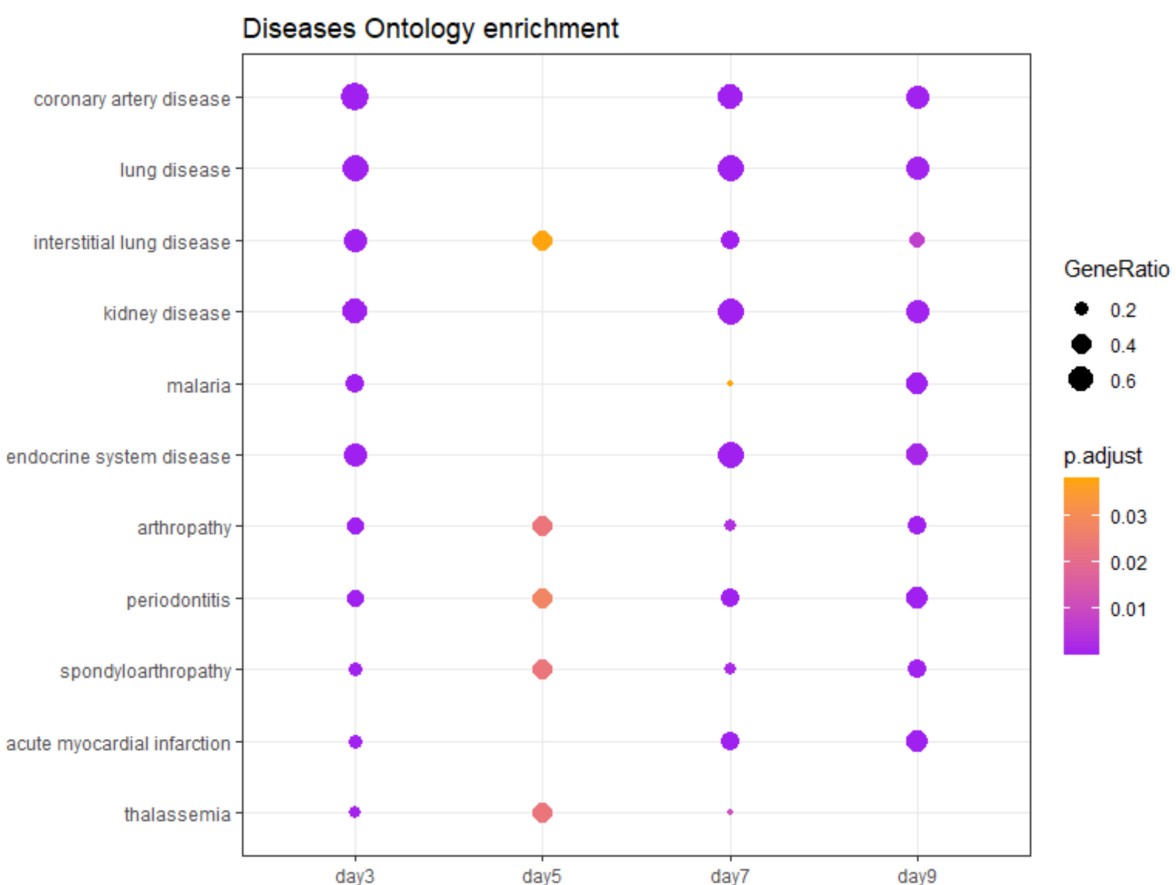


Figure 6.3: Longitudinal characterization of SASP from IR-PCLS. Diseases Ontology enrichment analysis of upregulated cytokines (Fold Change 30Gy/0Gy) at different time points.

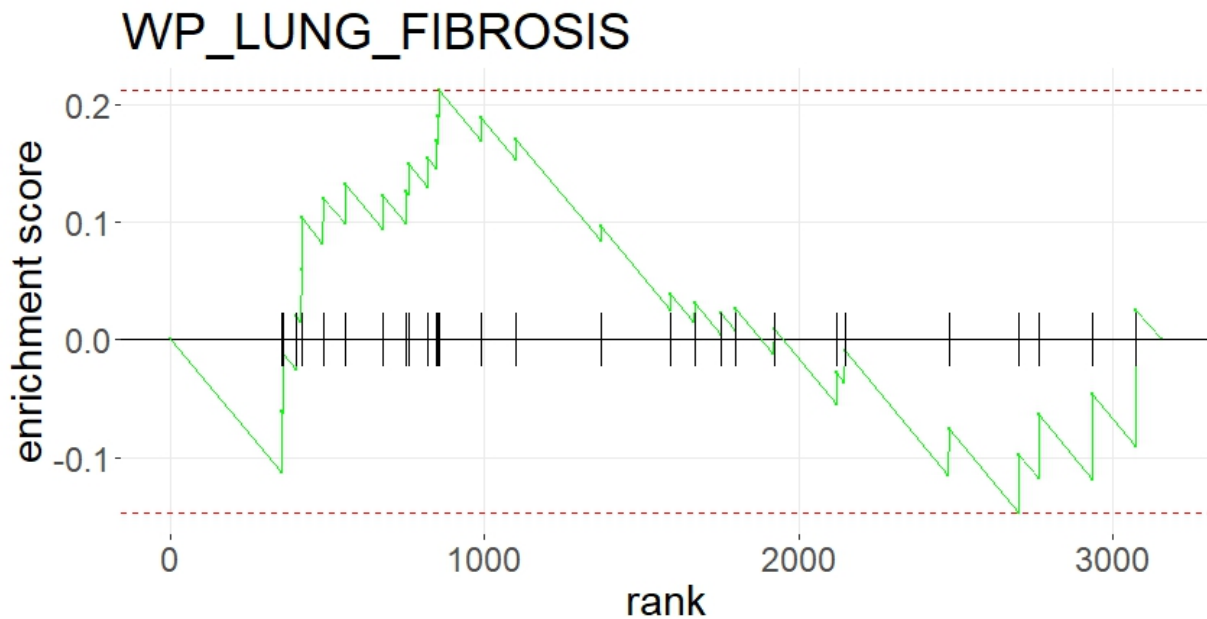


Figure 6.4: Gene set enrichment for the fibrosis-related gene set: WP-lung-fibrosis.

6.2 Supplementary Tables

Table 6.1: Top 50 differentially expressed genes in hPCLS at 7dpi. DEG were defined as the genes with a $\log_{2}FC > 0$ and $p\text{-adj-val} < 0.05$. Then, the top 50 DEG genes were filtered based on the $p\text{-adj-value}$.

HGNC_SYMBOL	ENTREZ_ID	baseMean	Log2FC	lfcSE	pvalue	padj
SCGB1A1	7356	2421.53	1.73	0.08	1.95E-117	1.40E-114
KRT17	3872	5197.41	1.53	0.04	1.12E-255	6.83E-252
S100A2	6273	2953.27	1.33	0.06	1.60E-119	1.33E-116
PIGR	5284	1563.85	1.23	0.07	8.43E-69	3.00E-66
CD14	929	1689.90	1.00	0.06	1.68E-71	6.55E-69
LSP1	4046	3659.08	0.89	0.04	1.42E-108	1.01E-105
CD163	9332	2094.80	0.80	0.05	7.18E-57	1.57E-54
S100A4	6275	8353.86	0.78	0.03	7.92E-150	1.24E-146
LGALS9	3965	2426.38	0.76	0.05	5.49E-59	1.36E-56
ITGAM	3684	2035.07	0.74	0.05	4.35E-47	6.79E-45

HGNC_SYMBOL	ENTREZ_ID	baseMean	Log2FC	lfcSE	pvalue	padj
FCER1G	2207	3366.84	0.73	0.04	3.10E-69	1.15E-66
CD53	963	2251.55	0.72	0.05	4.06E-49	7.20E-47
CYBA	1535	3052.81	0.70	0.04	1.75E-59	4.64E-57
GLIPR2	152007	2343.49	0.69	0.05	6.81E-48	1.13E-45
PLIN2	123	7339.01	0.64	0.03	2.00E-94	9.76E-92
LRP1	4035	17208.45	0.63	0.03	2.59E-140	3.22E-137
CYBB	1536	6994.92	0.61	0.03	1.11E-84	5.09E-82
SLC11A1	6556	3080.28	0.61	0.04	6.74E-47	1.07E-44
IL1RN	3557	4435.65	0.60	0.04	1.21E-58	4.77E-56
MT-ND4L	4539	18369.00	0.53	0.02	1.05E-106	6.84E-104
RNASE1	6035	5900.92	0.52	0.03	3.61E-54	7.05E-52
CD24	100133941	8788.09	0.48	0.03	1.45E-58	5.56E-56
GRINA	2907	7746.23	0.43	0.03	7.02E-46	1.04E-43
ITGB2	3689	9504.47	0.41	0.03	1.66E-46	2.57E-44
CSTB	1476	16474.69	0.41	0.02	1.07E-61	4.86E-59
GSN	2934	17745.52	0.39	0.02	3.88E-58	1.44E-55
MT-ND5	4540	69094.41	0.37	0.02	1.25E-64	3.95E-62
SFTPA1	653509	20765.88	0.37	0.02	3.77E-55	7.75E-53
COL3A1	1281	15616.66	-0.40	0.03	2.03E-59	5.75E-57
ASPH	444	9297.07	-0.45	0.03	1.15E-56	3.99E-54
GLS	2744	10990.22	-0.48	0.03	8.29E-69	3.00E-66
LDLR	3949	6822.26	-0.50	0.03	1.89E-56	3.99E-54
MMP1	4312	28849.55	-0.53	0.02	4.87E-124	4.53E-121
PEG10	23089	8362.91	-0.54	0.03	1.83E-75	7.34E-73
CLIC4	25932	8020.14	-0.56	0.03	1.39E-78	5.86E-76
KRT18	3875	12638.52	-0.57	0.03	1.23E-105	7.80E-103
ITGA6	3655	3634.62	-0.58	0.04	5.71E-48	1.01E-45
CRIM1	51232	3430.76	-0.58	0.04	4.24E-46	1.04E-43
TSPAN1	10103	3456.22	-0.60	0.04	2.90E-49	5.39E-47
ANXA3	306	3908.24	-0.60	0.04	1.85E-54	5.97E-52
EPCAM	4072	3174.15	-0.62	0.04	3.61E-49	7.20E-47
KRT8	3856	24868.02	-0.64	0.02	3.57E-177	7.33E-174
SLC6A14	11254	3835.23	-0.67	0.04	1.54E-64	7.53E-62

HGNC_SYMBOL	ENTREZ_ID	baseMean	Log2FC	lfcSE	pvalue	padj
HIF1A	3091	7448.72	-0.67	0.03	2.73E-104	1.60E-101
EMP2	2013	6330.53	-0.68	0.03	1.84E-95	9.32E-93
MAL2	114569	7946.28	-0.72	0.03	1.58E-125	1.85E-122
STEAP4	79689	2399.22	-0.79	0.05	9.99E-62	2.76E-59
CEACAM6	4680	31733.89	-0.95	0.02	0.00E+00	0.00E+00
RAB27B	5874	6365.87	-0.97	0.03	2.32E-186	5.89E-183
PI15	51050	245.93	-2.19	0.15	2.33E-49	8.08E-47

Table 6.2: Cytokines upregulated in IR-PCLS in at least one of the analyzed time points.

Name	Symbol	Day3	Day5	Day7	Day9
Adiponectin	ADIPOQ	2,051282051	0,491525424	1,633333333	0,864197531
Angiogenin	ANG	2,659685864	0,502857143	0,305882353	0,632013201
Angiopoietin-2	ANGPT2	2,05	0,276595745	0,148148148	0,59352518
BAFF	BAFF		1,03030303	1,325581395	0,4375
BDNF	BDNF	6,75	0,973684211	0,047619048	0,69047619
CD14	CD14	0,9	0,252873563	2,52173913	0,747747748
CD31	PECAM1	3,363636364	0,133333333	0,306451613	1,048888889
Complement Factor D	CFD	2,028169014	0,376811594	0,563291139	0,804384486
C-Reactive Protein	CRP			1,571428571	1,909090909
Cripto-1	TDGF1		0,120689655	1,727272727	4,090909091
Dkk-1	DKK1	4,097744361	3,819852941	1,467345716	0,268398268
ENA-78	CXCL5	1,68615257	1,043052838	0,965909091	0,656736939
Fas Ligand	FASLG			1,9	0,25974026
G-CSF	CSF3	3,086956522		0,272727273	0,822222222
GDF-15	GDF15	9,443262411	1,825599184	1,264440186	1,16684435
GRO-alpha	CXCL1	8,657142857	0,704663212	0,379227053	0,991786448
Growth Hormone	GH1			2,12	0,657142857
IFN-gamma	IFNG	0,068965517		0,442857143	1,714285714
IGFBP-3	IGFBP3		0,75	1,363636364	0,840517241
IL-1ra	IL1RN	2,16	0,219512195		0,851919561
IL-2	IL2				1,314285714
IL-3	IL3				1,882352941
IL-4	IL4	1,894736842		0,775862069	0,534883721
IL-6	IL6	2,521349862	0,661840745	0,764611044	0,326951399
IL-12 p70	IL12A		1,5	0,15	0,481481481

Name	Symbol	Day3	Day5	Day7	Day9
IL-15	IL15			1,6875	0,769230769
IL-16	IL16		0,166666667	7,333333333	0,836734694
IL-24	IL24		2,666666667	0,426666667	0,233333333
IL-27	IL27	0,075471698	0,045454545	1,35	0,857142857
IL-33	IL33		2,347826087		0,2
IP-10	CXCL10	2	0,125	1,692307692	0,928571429
I-TAC	CXCL11				5,235294118
Leptin	LEP	1,388888889		0,633333333	1,142857143
MIF	MIF	1,387931034	0,369426752	1,018181818	0,590604027
Myeloperoxidase	MPO	0,75			1,5
RAGE	AGER	3,145896657	1,237288136	0,668493151	1,222222222
Relaxin-2	RLN2				2,666666667
Resistin	ADSF			2,235294118	0,9375
Serpin E1	SERPINE1	1,785234899	0,931138857	1,398382749	0,657894737
TfR	TFRC			2,083333333	1,84375
TGF-alpha	TGFA		0,108695652		1,5
Thrombospondin-1	THBS1	0,444444444	0,011494253	0,290322581	1,769230769
TNF-alpha	TNF		0,62745098		6

List of Abbreviations

H_2O_2	oxygen peroxide
α -SMA	alpha Smooth Muscle Actin
γ H2Ax	phosphorylated H2A histone family member X
<i>CDKN1A</i> /P21	cyclin dependent kinase inhibitor 1A
<i>CDKN2A</i> /P16	cyclin dependent kinase inhibitor 2A
ABT-263	Navitoclax
ACT	Acetylated tubulin
ACTA2	smooth Muscle Actin Alpha 2
AKT	protein kinase B
ANGPT-2	angiopoietin-2
ANGPT2	Angiopoietin 2
AT1	alveolar type I
AT2	alveolar type II
ATM	ataxia telangiectasia-mutated protein
AXIN2	axis inhibition protein 2
BafA1	bafilomycin A1
Bak	BCL2 Antagonist/Killer
BALF	bronchoalveolar lavage fluid
Bax	BCL2-like protein 4
Bcl-w	bcl-2-like protein 2
Bcl-xL	B-cell lymphoma-extra large
BCL-2	B-cell lymphoma 2
BRCA1	breast cancer gene 1
BSA	bovine serum albumin
C_{12} FDG	5-dodecanoylaminofluorescein-di- β -D-galactopyranoside
CC3	cleaved-caspase 3
CCL2	C-C Motif Chemokine Ligand 2

CCL20	C-C Motif Chemokine Ligand 20
CCL3	C-C Motif Chemokine Ligand 3
CD14	cluster of differentiation 14
CD45	protein tyrosine phosphatase receptor type C
CD90	cluster of Differentiation 90
CEBP β	CCAAT Enhancer Binding Protein Beta
CLDs	chronic lung diseases
COL1A1	alpha-1 Type I Collagen
COL3A1	alpha-1 Type III Collagen
COPD	Chronic Obstructive Pulmonary Disease
CRYPTO1	teratocarcinoma-derived growth factor 1
CRP	C-Reactive Protein
CXCL1	C-X-C Motif Chemokine Ligand 1
CXCL11	C-X-C motif chemokine 11
CXCL2	Chemokine (C-X-C motif) ligand 2
DAPI	4,6-diamidino-2-phenylindole
DDR	DNA-damage response
DEG	differentially expressed genes
DNA-SCARS	DNA segments with chromatin alterations reinforcing senescence
dpi	days post irradiation
DPP4	dipeptidyl peptidase 4
DQ	Dasatinib + Quercetin
DSBs	DNA double-strand breaks
ECM	extracellular matrix
ELISA	enzyme-linked immunosorbent assay
EMT	epithelial–mesenchymal transition
EpCAM	epithelial cell adhesion molecule
FCS	fetal calf serum
FDA	Food and Drug Administration
FFPE	formalin-fixed paraffin-embedded
FN1	fibronectin 1
GDF-15	growth Differentiation Factor 15
Gy	Gray
H3K9me3	tri-methylated 9th lysine residue of the histone H3 protein

HP1	heterochromatin protein 1
hPCLS	Human Precision-cut lung slices
HUVECs	human umbilical vein endothelial cell
ICAM-1	intercellular Adhesion Molecule 1
IF	immunofluorescence
IFN γ	interferon Gamma
IGFBP-3	insulin-like growth factor-binding protein 3
IL-8	interleukin 8
IL-15	interleukin 15
IL-1 α	interleukin 1 Alpha
IL-6	interleukin 6
ILDs	interstitial lung diseases
IMR90	human fetal lung fibroblasts
IPF	Idiopathic Pulmonary Fibrosis
IR	ionizing radiation
IR-hPCLS	irradiated human PCLS
IR-PCLS	irradiated precision-cut lung slices
K8	Keratin-8
KRT17	Keratin 17
LDH	lactate Dehydrogenase
LFC	log-fold change
LPA	lipoprotein A
MeOH	methanol
MFI	mean fluorescence intensity
mPCLS	murine Precision-cut lung slices
MPO	Myeloperoxidase
NF- κ B	nuclear factor kappa B
PAI-1	plasminogen Activator Inhibitor 1
PBST	triton X-100 in 1X PBS
PCA	principal component analysis
PCLS	precision-cut lung slices
PDGF-AB	platelet-derived growth factor
PDGFR-AB	platelet-derived growth factor receptor
PDPN	podoplanin
PFA	paraformaldehyde

phLF	primary human lung fibroblasts
PI3K	phosphoinositide 3-kinase
PIIINP	collagen type III N-terminal propeptide
pmAT2	primary murine AT2 cells
PRB	phosphorylated Retinoblastoma protein
rhCripto1	recombinant human Cripto-1
RILF	radiation-induced lung injury
RIPF	radiation-induced pulmonary fibrosis
ROS	reactive oxygen species
SA- β -gal	senescence-associated β -Galactosidase
SAHFs	senescence-associated heterochromatin foci
SAPs	senescent anti-apoptotic pathways
SASP	senescence-Associated Secretory Phenotype
SDF-1 α	stromal cell-derived factor 1
SERPINF1	serpin Family F Member 1
SERPINs	serine protease inhibitors
SFTPC	surfactant protein C
Tert	telomerase reverse transcriptase
TFRC	Transferrin Receptor
TGF α	transforming Growth Factor Alpha
TGF- β 1	transforming Growth Factor Beta
THBS1	thrombospondin 1
TNF-a	tumor necrosis factor alpha
TP53	tumor Suppressor P53
VEGFA	vascular Endothelial Growth Factor A
WST-1	water-Soluble Tetrazolium 1
X-gal	5-bromo-4-chloro-3-indoyl-d-galactopyranoside

References

Acosta, J. C., Banito, A., Wuestefeld, T., Georgilis, A., Janich, P., Morton, J. P., Athineos, D., Kang, T.-W., Lasitschka, F., Andrulis, M., Pascual, G., Morris, K. J., Khan, S., Jin, H., Dharmalingam, G., Snijders, A. P., Carroll, T., Capper, D., Pritchard, C., ... Gil, J. (2013). A complex secretory program orchestrated by the inflammasome controls paracrine senescence. *Nature cell biology*, 15(8), 978–990. <https://doi.org/10.1038/ncb2784>

Adams, T. S., Schupp, J. C., Poli, S., Ayaub, E. A., Neumark, N., Ahangari, F., Chu, S. G., Raby, B. A., DeIuliis, G., Januszyk, M., Duan, Q., Arnett, H. A., Siddiqui, A., Washko, G. R., Homer, R., Yan, X., Rosas, I. O., & Kaminski, N. (2020). Single-cell RNA-seq reveals ectopic and aberrant lung-resident cell populations in idiopathic pulmonary fibrosis [Publisher: American Association for the Advancement of Science]. *Science Advances*, 6(28), eaba1983. <https://doi.org/10.1126/sciadv.aba1983>

Adamson, I. Y. R., & Bowden, D. H. (1974). The Pathogenesis of Bleomycin-Induced Pulmonary Fibrosis in Mice. *The American Journal of Pathology*, 77(2), 185–198. Retrieved June 11, 2023, from <https://www.ncbi.nlm.nih.gov/pmc/articles/PMC1910906/>

Aghali, A., Koloko Ngassie, M. L., Pabelick, C. M., & Prakash, Y. S. (2022). Cellular Senescence in Aging Lungs and Diseases. *Cells*, 11(11), 1781. <https://doi.org/10.3390/cells11111781>

Aimo, A., Spitaleri, G., Nieri, D., Tavanti, L. M., Meschi, C., Panichella, G., Lupón, J., Pistelli, F., Carrozza, L., Bayes-Genis, A., & Emdin, M. (2022). Pirfenidone for Idiopathic Pulmonary Fibrosis and Beyond. *Cardiac Failure Review*, 8, e12. <https://doi.org/10.15420/cfr.2021.30>

Alessio, N., Del Gaudio, S., Capasso, S., Di Bernardo, G., Cappabianca, S., Cipollaro, M., Peluso, G., & Galderisi, U. (2014). Low dose radiation induced senescence of human

mesenchymal stromal cells and impaired the autophagy process. *Oncotarget*, 6(10), 8155–8166. Retrieved June 21, 2023, from <https://www.ncbi.nlm.nih.gov/pmc/articles/PMC4480742/>

Alsafadi, H. N., Staab-Weijnitz, C. A., Lehmann, M., Lindner, M., Peschel, B., Königshoff, M., & Wagner, D. E. (2017). An ex vivo model to induce early fibrosis-like changes in human precision-cut lung slices. *American Journal of Physiology. Lung Cellular and Molecular Physiology*, 312(6), L896–L902. <https://doi.org/10.1152/ajplung.00084.2017>

Anderson, R., Lagnado, A., Maggiorani, D., Walaszczuk, A., Dookun, E., Chapman, J., Birch, J., Salmonowicz, H., Ogródniak, M., Jurk, D., Proctor, C., Correia-Melo, C., Victorelli, S., Fielder, E., Berlinguer-Palmini, R., Owens, A., Greaves, L. C., Kolsky, K. L., Parini, A., . . . Passos, J. F. (2019). Length-independent telomere damage drives post-mitotic cardiomyocyte senescence. *The EMBO Journal*, 38(5), e100492. <https://doi.org/10.15252/embj.2018100492>

Arnouk, H., Yum, G., & Shah, D. (2021). Cripto-1 as a Key Factor in Tumor Progression, Epithelial to Mesenchymal Transition and Cancer Stem Cells [Number: 17 Publisher: Multidisciplinary Digital Publishing Institute]. *International Journal of Molecular Sciences*, 22(17), 9280. <https://doi.org/10.3390/ijms22179280>

Aversa, Z., Atkinson, E. J., Carmona, E. M., White, T. A., Heeren, A. A., Jachim, S. K., Zhang, X., Cummings, S. R., Chiarella, S. E., Limper, A. H., & LeBrasseur, N. K. (2023). Biomarkers of cellular senescence in idiopathic pulmonary fibrosis. *Respiratory Research*, 24(1), 101. <https://doi.org/10.1186/s12931-023-02403-8>

Baker, D. J., Wijshake, T., Tchkonia, T., LeBrasseur, N. K., Childs, B. G., van de Sluis, B., Kirkland, J. L., & van Deursen, J. M. (2011). Clearance of p16 Ink4a -positive senescent cells delays ageing-associated disorders [Number: 7372 Publisher: Nature Publishing Group]. *Nature*, 479(7372), 232–236. <https://doi.org/10.1038/nature10600>

Baptista, D., Moreira Teixeira, L., Barata, D., Tahmasebi Birgani, Z., King, J., van Riet, S., Pasman, T., Poot, A. A., Stamatialis, D., Rottier, R. J., Hiemstra, P. S., Carlier, A., van Blitterswijk, C., Habibović, P., Giselbrecht, S., & Truckenmüller, R. (2022). 3D Lung-on-Chip Model Based on Biomimetically Microcurved Culture Membranes [Publisher: American Chemical Society]. *ACS Biomaterials Science & Engineering*, 8(6), 2684–2699. <https://doi.org/10.1021/acsbiomaterials.1c01463>

Barkauskas, C. E., Cronce, M. J., Rackley, C. R., Bowie, E. J., Keene, D. R., Stripp, B. R., Randell, S. H., Noble, P. W., & Hogan, B. L. M. (2013). Type 2 alveolar cells are

stem cells in adult lung [Publisher: American Society for Clinical Investigation]. *The Journal of Clinical Investigation*, 123(7), 3025–3036. <https://doi.org/10.1172/JCI68782>

Basisty, N., Kale, A., Jeon, O. H., Kuehnemann, C., Payne, T., Rao, C., Holtz, A., Shah, S., Sharma, V., Ferrucci, L., Campisi, J., & Schilling, B. (2020). A proteomic atlas of senescence-associated secretomes for aging biomarker development [Publisher: Public Library of Science]. *PLOS Biology*, 18(1), e3000599. <https://doi.org/10.1371/journal.pbio.3000599>

Beach, T. A., Johnston, C. J., Groves, A. M., Williams, J. P., & Finkelstein, J. N. (2017). Radiation Induced Pulmonary Fibrosis as a Model of Progressive Fibrosis: Contributions of DNA Damage, Inflammatory Response and Cellular Senescence Genes. *Experimental lung research*, 43(3), 134–149. <https://doi.org/10.1080/01902148.2017.1318975>

Beauséjour, C. M., Krtolica, A., Galimi, F., Narita, M., Lowe, S. W., Yaswen, P., & Campisi, J. (2003). Reversal of human cellular senescence: Roles of the p53 and p16 pathways. *The EMBO Journal*, 22(16), 4212–4222. <https://doi.org/10.1093/emboj/cdg417>

Belsches-Jablonski, A. P., Biscardi, J. S., Peavy, D. R., Tice, D. A., Romney, D. A., & Parsons, S. J. (2001). Src family kinases and HER2 interactions in human breast cancer cell growth and survival [Number: 12 Publisher: Nature Publishing Group]. *Oncogene*, 20(12), 1465–1475. <https://doi.org/10.1038/sj.onc.1204205>

Bianco, C., Rangel, M. C., Castro, N. P., Nagaoka, T., Rollman, K., Gonzales, M., & Salomon, D. S. (2010). Role of Cripto-1 in Stem Cell Maintenance and Malignant Progression. *The American Journal of Pathology*, 177(2), 532–540. <https://doi.org/10.2353/ajpath.2010.100102>

Boots, A. W., Veith, C., Albrecht, C., Bartholome, R., Drittij, M.-J., Claessen, S. M. H., Bast, A., Rosenbruch, M., Jonkers, L., van Schooten, F.-J., & Schins, R. P. F. (2020). The dietary antioxidant quercetin reduces hallmarks of bleomycin-induced lung fibrogenesis in mice. *BMC Pulmonary Medicine*, 20(1), 112. <https://doi.org/10.1186/s12890-020-1142-x>

Bramey, N., Melo-Narvaez, M. C., See, F., Ballester-Llobell, B., Steinchen, C., Jain, E., Hafner, K., Yildirim, A. Ö., Königshoff, M., & Lehmann, M. (2023). Primary human lung fibroblasts exhibit trigger- but not disease-specific cellular senescence and

impair alveolar epithelial cell progenitor function [Pages: 2023.07.24.550385 Section: New Results]. <https://doi.org/10.1101/2023.07.24.550385>

Bukas, C. (2022). HelmholtzAI-Consultants-Munich/napari-organoid-counter: Latest versions of dependencies. <https://doi.org/10.5281/zenodo.7065206>

Campisi, J., & d'Adda di Fagagna, F. (2007). Cellular senescence: When bad things happen to good cells [Number: 9 Publisher: Nature Publishing Group]. *Nature Reviews Molecular Cell Biology*, 8(9), 729–740. <https://doi.org/10.1038/nrm2233>

Canman, C. E., Lim, D.-S., Cimprich, K. A., Taya, Y., Tamai, K., Sakaguchi, K., Appella, E., Kastan, M. B., & Siliciano, J. D. (1998). Activation of the ATM Kinase by Ionizing Radiation and Phosphorylation of p53 [Publisher: American Association for the Advancement of Science]. *Science*, 281(5383), 1677–1679. <https://doi.org/10.1126/science.281.5383.1677>

Chaib, S., Tchkonia, T., & Kirkland, J. L. (2022). Cellular senescence and senolytics: The path to the clinic [Number: 8 Publisher: Nature Publishing Group]. *Nature Medicine*, 28(8), 1556–1568. <https://doi.org/10.1038/s41591-022-01923-y>

Chanda, D., Otoupalova, E., Smith, S. R., Volckaert, T., De Langhe, S. P., & Thannickal, V. J. (2019). Developmental Pathways in the Pathogenesis of Lung Fibrosis. *Molecular aspects of medicine*, 65, 56–69. <https://doi.org/10.1016/j.mam.2018.08.004>

Chandra, A., Lagnado, A. B., Farr, J. N., Doolittle, M., Tchkonia, T., Kirkland, J. L., LeBrasseur, N. K., Robbins, P. D., Niedernhofer, L. J., Ikeno, Y., Passos, J. F., Monroe, D. G., Pignolo, R. J., & Khosla, S. (2022). Targeted clearance of p21-but not p16-positive senescent cells prevents radiation-induced osteoporosis and increased marrow adiposity. *Aging Cell*, 21(5), e13602. <https://doi.org/10.1111/acel.13602>

Chandra, T., & Narita, M. (2013). High-order chromatin structure and the epigenome in SAHFs. *Nucleus*, 4(1), 23–28. <https://doi.org/10.4161/nucl.23189>

Chen, Z., Cao, K., Xia, Y., Li, Y., Hou, Y., Wang, L., Li, L., Chang, L., & Li, W. (2019). Cellular senescence in ionizing radiation (Review) [Publisher: Spandidos Publications]. *Oncology Reports*, 42(3), 883–894. <https://doi.org/10.3892/or.2019.7209>

Childs, B. G., Gluscevic, M., Baker, D. J., Laberge, R.-M., Marques, D., Dananberg, J., & van Deursen, J. M. (2017). Senescent cells: An emerging target for diseases of ageing. *Nature reviews. Drug discovery*, 16(10), 718–735. <https://doi.org/10.1038/nrd.2017.116>

Cho, S. J., Pronko, A., Yang, J., & Stout-Delgado, H. (2023). Impact of Senolytic Treatment on Gene Expression in Aged Lung [Number: 8 Publisher: Multidisciplinary Digital Publishing Institute]. *International Journal of Molecular Sciences*, 24(8), 7628. <https://doi.org/10.3390/ijms24087628>

Cooley, J. C., Javkhlan, N., Wilson, J. A., Foster, D. G., Edelman, B. L., Ortiz, L. A., Schwartz, D. A., Riches, D. W., & Redente, E. F. (2023). Inhibition of antiapoptotic BCL-2 proteins with ABT-263 induces fibroblast apoptosis, reversing persistent pulmonary fibrosis. *JCI insight*, 8(3), e163762. <https://doi.org/10.1172/jci.insight.163762>

Coppé, J.-P., Desprez, P.-Y., Krtolica, A., & Campisi, J. (2010). The senescence-associated secretory phenotype: The dark side of tumor suppression. *Annual Review of Pathology*, 5, 99–118. <https://doi.org/10.1146/annurev-pathol-121808-102144>

Coppé, J.-P., Patil, C. K., Rodier, F., Sun, Y., Muñoz, D. P., Goldstein, J., Nelson, P. S., Desprez, P.-Y., & Campisi, J. (2008). Senescence-Associated Secretory Phenotypes Reveal Cell-Nonautonomous Functions of Oncogenic RAS and the p53 Tumor Suppressor [Publisher: Public Library of Science]. *PLOS Biology*, 6(12), e301. <https://doi.org/10.1371/journal.pbio.0060301>

Curras-Alonso, S., Soulier, J., Defard, T., Weber, C., Heinrich, S., Laporte, H., Leboucher, S., Lameiras, S., Dutreix, M., Favaudon, V., Massip, F., Walter, T., Mueller, F., Londoño-Vallejo, J.-A., & Fouillade, C. (2023). An interactive murine single-cell atlas of the lung responses to radiation injury [Number: 1 Publisher: Nature Publishing Group]. *Nature Communications*, 14(1), 2445. <https://doi.org/10.1038/s41467-023-38134-z>

Debacq-Chainiaux, F., Erusalimsky, J. D., Campisi, J., & Toussaint, O. (2009). Protocols to detect senescence-associated beta-galactosidase (SA-gal) activity, a biomarker of senescent cells in culture and in vivo [Number: 12 Publisher: Nature Publishing Group]. *Nature Protocols*, 4(12), 1798–1806. <https://doi.org/10.1038/nprot.2009.191>

Degryse, A. L., Tanjore, H., Xu, X. C., Polosukhin, V. V., Jones, B. R., Boomershine, C. S., Ortiz, C., Sherrill, T. P., McMahon, F. B., Gleaves, L. A., Blackwell, T. S., & Lawson, W. E. (2011). TGF signaling in lung epithelium regulates bleomycin-induced alveolar injury and fibroblast recruitment. *American Journal of Physiology - Lung Cellular and Molecular Physiology*, 300(6), L887–L897. <https://doi.org/10.1152/ajplung.00397.2010>

Degryse, A. L., Tanjore, H., Xu, X. C., Polosukhin, V. V., Jones, B. R., McMahon, F. B., Gleaves, L. A., Blackwell, T. S., & Lawson, W. E. (2010). Repetitive intratracheal bleomycin models several features of idiopathic pulmonary fibrosis. *American Journal of Physiology - Lung Cellular and Molecular Physiology*, 299(4), L442–L452. <https://doi.org/10.1152/ajplung.00026.2010>

de Mera-Rodríguez, J. A., Álvarez-Hernán, G., Gañán, Y., Martín-Partido, G., Rodríguez-León, J., & Francisco-Morcillo, J. (2021). Is Senescence-Associated -Galactosidase a Reliable in vivo Marker of Cellular Senescence During Embryonic Development? *Frontiers in Cell and Developmental Biology*, 9. Retrieved July 12, 2023, from <https://www.frontiersin.org/articles/10.3389/fcell.2021.623175>

DePianto, D. J., Heiden, J. A. V., Morshead, K. B., Sun, K.-H., Modrusan, Z., Teng, G., Wolters, P. J., & Arron, J. R. (2021). Molecular mapping of interstitial lung disease reveals a phenotypically distinct senescent basal epithelial cell population [Publisher: American Society for Clinical Investigation]. <https://doi.org/10.1172/jci.insight.143626>

Deursen, V., & M, J. (2014). The role of senescent cells in ageing [Number: 7501 Publisher: Nature Publishing Group]. *Nature*, 509(7501), 439–446. <https://doi.org/10.1038/nature13193>

Di Micco, R., Krizhanovsky, V., Baker, D., & d'Adda di Fagagna, F. (2021). Cellular senescence in ageing: From mechanisms to therapeutic opportunities. *Nature reviews. Molecular cell biology*, 22(2), 75–95. <https://doi.org/10.1038/s41580-020-00314-w>

Dimri, G. P., Lee, X., Basile, G., Acosta, M., Scott, G., Roskelley, C., Medrano, E. E., Linskens, M., Rubelj, I., & Pereira-Smith, O. (1995). A biomarker that identifies senescent human cells in culture and in aging skin in vivo. *Proceedings of the National Academy of Sciences of the United States of America*, 92(20), 9363–9367. Retrieved June 18, 2023, from <https://www.ncbi.nlm.nih.gov/pmc/articles/PMC40985/>

Ding, N.-H., Li, J. J., & Sun, L.-Q. (2013). Molecular Mechanisms and Treatment of Radiation-Induced Lung Fibrosis. *Current drug targets*, 14(11), 1347–1356. Retrieved July 14, 2023, from <https://www.ncbi.nlm.nih.gov/pmc/articles/PMC4156316/>

Doura, T., Kamiya, M., Obata, F., Yamaguchi, Y., Hiyama, T. Y., Matsuda, T., Fukamizu, A., Noda, M., Miura, M., & Urano, Y. (2016). Detection of LacZ-Positive Cells in

Living Tissue with Single-Cell Resolution. *Angewandte Chemie (International Ed. in English)*, 55(33), 9620–9624. <https://doi.org/10.1002/anie.201603328>

Du, K., Zhu, Y., Mao, R., Qu, Y., Cui, B., Ma, Y., Zhang, X., & Chen, Z. (2022). Medium-long term prognosis prediction for idiopathic pulmonary fibrosis patients based on quantitative analysis of fibrotic lung volume. *Respiratory Research*, 23(1), 372. <https://doi.org/10.1186/s12931-022-02276-3>

Dulić, V., Beney, G.-E., Frebourg, G., Drullinger, L. F., & Stein, G. H. (2000). Uncoupling between Phenotypic Senescence and Cell Cycle Arrest in Aging p21-Deficient Fibroblasts. *Molecular and Cellular Biology*, 20(18), 6741–6754. Retrieved June 18, 2023, from <https://www.ncbi.nlm.nih.gov/pmc/articles/PMC86196/>

Flaherty, K. R., Wells, A. U., Cottin, V., Devaraj, A., Walsh, S. L., Inoue, Y., Richeldi, L., Kolb, M., Tetzlaff, K., Stowasser, S., Coeck, C., Clerisme-Beaty, E., Rosenstock, B., Quaresma, M., Haeufel, T., Goeldner, R.-G., Schlenker-Herceg, R., & Brown, K. K. (2019). Nintedanib in Progressive Fibrosing Interstitial Lung Diseases [Publisher: Massachusetts Medical Society _eprint: <https://doi.org/10.1056/NEJMoa1908681>]. *New England Journal of Medicine*, 381(18), 1718–1727. <https://doi.org/10.1056/NEJMoa1908681>

Freund, A., Laberge, R.-M., Demaria, M., & Campisi, J. (2012). Lamin B1 loss is a senescence-associated biomarker. *Molecular Biology of the Cell*, 23(11), 2066–2075. <https://doi.org/10.1091/mbc.E11-10-0884>

Fridman, A. L., & Tainsky, M. A. (2008). Critical pathways in cellular senescence and immortalization revealed by gene expression profiling. *Oncogene*, 27(46), 5975–5987. <https://doi.org/10.1038/onc.2008.213>

Gasek, N. S., Kuchel, G. A., Kirkland, J. L., & Xu, M. (2021). Strategies for targeting senescent cells in human disease [Number: 10 Publisher: Nature Publishing Group]. *Nature Aging*, 1(10), 870–879. <https://doi.org/10.1038/s43587-021-00121-8>

Gerckens, M., Alsafadi, H. N., Wagner, D. E., Lindner, M., Burgstaller, G., & Königshoff, M. (2019). Generation of Human 3D Lung Tissue Cultures (3D-LTCs) for Disease Modeling. *JoVE (Journal of Visualized Experiments)*, (144), e58437. <https://doi.org/10.3791/58437>

Gerckens, M., Schorpp, K., Pelizza, F., Wögrath, M., Reichau, K., Ma, H., Dworsky, A.-M., Sengupta, A., Stoleriu, M. G., Heinzelmann, K., Merl-Pham, J., Irmler, M., Alsafadi, H. N., Trenkenschuh, E., Sarnova, L., Jirouskova, M., Frieß, W., Hauck, S. M., Beckers, J., ... Burgstaller, G. (2021). Phenotypic drug screening in a human fibrosis

model identified a novel class of antifibrotic therapeutics. *Science Advances*, 7(52), eabb3673. <https://doi.org/10.1126/sciadv.abb3673>

Glass, D. S., Grossfeld, D., Renna, H. A., Agarwala, P., Spiegler, P., DeLeon, J., & Reiss, A. B. (2022). Idiopathic pulmonary fibrosis: Current and future treatment [eprint: <https://onlinelibrary.wiley.com/doi/pdf/10.1111/crj.13466>]. *The Clinical Respiratory Journal*, 16(2), 84–96. <https://doi.org/10.1111/crj.13466>

González-Gualda, E., Baker, A. G., Fruk, L., & Muñoz-Espín, D. (2021). A guide to assessing cellular senescence in vitro and in vivo. *The FEBS Journal*, 288(1), 56–80. <https://doi.org/10.1111/febs.15570>

Habermann, A. C., Gutierrez, A. J., Bui, L. T., Yahn, S. L., Winters, N. I., Calvi, C. L., Peter, L., Chung, M.-I., Taylor, C. J., Jetter, C., Raju, L., Roberson, J., Ding, G., Wood, L., Sucre, J. M. S., Richmond, B. W., Serezani, A. P., McDonnell, W. J., Mallal, S. B., ... Kropski, J. A. (2020). Single-cell RNA sequencing reveals profibrotic roles of distinct epithelial and mesenchymal lineages in pulmonary fibrosis. *Science Advances*, 6(28), eaba1972. <https://doi.org/10.1126/sciadv.aba1972>

Heberle, H., Meirelles, G. V., da Silva, F. R., Telles, G. P., & Minghim, R. (2015). InteractiVenn: A web-based tool for the analysis of sets through Venn diagrams. *BMC Bioinformatics*, 16(1), 169. <https://doi.org/10.1186/s12859-015-0611-3>

Hecker, L., Logsdon, N. J., Kurundkar, D., Kurundkar, A., Bernard, K., Hock, T., Meldrum, E., Sanders, Y. Y., & Thannickal, V. J. (2014). Reversal of persistent fibrosis in aging by targeting Nox4-Nrf2 redox imbalance. *Science Translational Medicine*, 6(231), 231ra47. <https://doi.org/10.1126/scitranslmed.3008182>

Hernandez-Segura, A., de Jong, T. V., Melov, S., Guryev, V., Campisi, J., & Demaria, M. (2017). Unmasking Transcriptional Heterogeneity in Senescent Cells. *Current biology : CB*, 27(17), 2652–2660.e4. <https://doi.org/10.1016/j.cub.2017.07.033>

Hernandez-Segura, A., Nehme, J., & Demaria, M. (2018). Hallmarks of Cellular Senescence. *Trends in Cell Biology*, 28(6), 436–453. <https://doi.org/10.1016/j.tcb.2018.02.001>

Hesse, C., Beneke, V., Konzok, S., Diefenbach, C., Bülow Sand, J. M., Rønnow, S. R., Karsdal, M. A., Jonigk, D., Sewald, K., Braun, A., Leeming, D. J., & Wollin, L. (2022). Nintedanib modulates type III collagen turnover in viable precision-cut lung slices from bleomycin-treated rats and patients with pulmonary fibrosis. *Respiratory Research*, 23(1), 201. <https://doi.org/10.1186/s12931-022-02116-4>

Hickson, L. J., Prata, L. G. P. L., Bobart, S. A., Evans, T. K., Giorgadze, N., Hashmi, S. K., Herrmann, S. M., Jensen, M. D., Jia, Q., Jordan, K. L., Kellogg, T. A.,

Khosla, S., Koerber, D. M., Lagnado, A. B., Lawson, D. K., LeBrasseur, N. K., Lerman, L. O., McDonald, K. M., McKenzie, T. J., ... Kirkland, J. L. (2019). Senolytics decrease senescent cells in humans: Preliminary report from a clinical trial of Dasatinib plus Quercetin in individuals with diabetic kidney disease [Publisher: Elsevier]. *eBioMedicine*, 47, 446–456. <https://doi.org/10.1016/j.ebiom.2019.08.069>

Huang, B.-W., & Gao, J.-Q. (2018). Application of 3D cultured multicellular spheroid tumor models in tumor-targeted drug delivery system research. *Journal of Controlled Release: Official Journal of the Controlled Release Society*, 270, 246–259. <https://doi.org/10.1016/j.jconrel.2017.12.005>

Huang, W., Hickson, L. J., Eirin, A., Kirkland, J. L., & Lerman, L. O. (2022). Cellular senescence: The good, the bad and the unknown [Number: 10 Publisher: Nature Publishing Group]. *Nature Reviews Nephrology*, 18(10), 611–627. <https://doi.org/10.1038/s41581-022-00601-z>

Huh, D., Matthews, B. D., Mammoto, A., Montoya-Zavala, M., Hsin, H. Y., & Ingber, D. E. (2010). Reconstituting organ-level lung functions on a chip. *Science (New York, N.Y.)*, 328(5986), 1662–1668. <https://doi.org/10.1126/science.1188302>

Jiang, C., Liu, G., Cai, L., Deshane, J., Antony, V., Thannickal, V. J., & Liu, R.-M. (2021). Divergent Regulation of Alveolar Type 2 Cell and Fibroblast Apoptosis by Plasminogen Activator Inhibitor 1 in Lung Fibrosis. *The American Journal of Pathology*, 191(7), 1227–1239. <https://doi.org/10.1016/j.ajpath.2021.04.003>

Jin, H., Yoo, Y., Kim, Y., Kim, Y., Cho, J., & Lee, Y.-S. (2020). Radiation-Induced Lung Fibrosis: Preclinical Animal Models and Therapeutic Strategies [Number: 6 Publisher: Multidisciplinary Digital Publishing Institute]. *Cancers*, 12(6), 1561. <https://doi.org/10.3390/cancers12061561>

Justice, J. N., Nambiar, A. M., Tchkonia, T., LeBrasseur, N. K., Pascual, R., Hashmi, S. K., Prata, L., Masternak, M. M., Kritchevsky, S. B., Musi, N., & Kirkland, J. L. (2019). Senolytics in idiopathic pulmonary fibrosis: Results from a first-in-human, open-label, pilot study. *EBioMedicine*, 40, 554–563. <https://doi.org/10.1016/j.ebiom.2018.12.052>

Kang, T.-W., Yevsa, T., Woller, N., Hoenicke, L., Wuestefeld, T., Dauch, D., Hohmeyer, A., Gereke, M., Rudalska, R., Potapova, A., Iken, M., Vucur, M., Weiss, S., Heikenwalder, M., Khan, S., Gil, J., Bruder, D., Manns, M., Schirmacher, P., ... Zender, L. (2011). Senescence surveillance of pre-malignant hepatocytes limits liver cancer development. *Nature*, 479(7374), 547–551. <https://doi.org/10.1038/nature10599>

Karkampouna, S., van der Helm, D., Scarpa, M., van Hoek, B., Verspaget, H. W., Goumans, M.-J., Coenraad, M. J., Kruithof, B. P. T., & Kruithof-de Julio, M. (2021). Oncofetal Protein CRIPTO Is Involved in Wound Healing and Fibrogenesis in the Regenerating Liver and Is Associated with the Initial Stages of Cardiac Fibrosis [Number: 12 Publisher: Multidisciplinary Digital Publishing Institute]. *Cells*, 10(12), 3325. <https://doi.org/10.3390/cells10123325>

Khan, P., Roux, J., Blumer, S., Knudsen, L., Jonigk, D., Kuehnel, M. P., Tamm, M., & Hostettler, K. E. (2022). Alveolar Basal Cells Differentiate towards Secretory Epithelial- and Aberrant Basaloid-like Cells In Vitro. *Cells*, 11(11), 1820. <https://doi.org/10.3390/cells11111820>

Kim, K. M., Noh, J. H., Bodogai, M., Martindale, J. L., Yang, X., Indig, F. E., Basu, S. K., Ohnuma, K., Morimoto, C., Johnson, P. F., Biragyn, A., Abdelmohsen, K., & Gorospe, M. (2017). Identification of senescent cell surface targetable protein DPP4. *Genes & Development*, 31(15), 1529–1534. <https://doi.org/10.1101/gad.302570.117>

Kim, S.-H., Lee, J. Y., Yoon, C. M., Shin, H. J., Lee, S. W., Rosas, I., Herzog, E., Cruz, C. D., Kaminski, N., & Kang, M.-J. (2021). MAVS is crucial for the development of pulmonary fibrosis and is inhibited by proapoptotic BH3 mimetics. *The European respiratory journal*, 57(4), 2000652. <https://doi.org/10.1183/13993003.00652-2020>

Kim, S., & Kim, C. (2021). Transcriptomic Analysis of Cellular Senescence: One Step Closer to Senescence Atlas. *Molecules and Cells*, 44(3), 136–145. <https://doi.org/10.14348/molcells.2021.2239>

King, T. E., Bradford, W. Z., Castro-Bernardini, S., Fagan, E. A., Glaspole, I., Glassberg, M. K., Gorina, E., Hopkins, P. M., Kardatzke, D., Lancaster, L., Lederer, D. J., Nathan, S. D., Pereira, C. A., Sahn, S. A., Sussman, R., Swigris, J. J., & Noble, P. W. (2014). A Phase 3 Trial of Pirfenidone in Patients with Idiopathic Pulmonary Fibrosis. *New England Journal of Medicine*, 370(22), 2083–2092. <https://doi.org/10.1056/NEJMoa1402582>

Kirkland, J. L., & Tchkonia, T. (2020). Senolytic drugs: From discovery to translation. *Journal of Internal Medicine*, 288(5), 518–536. <https://doi.org/10.1111/joim.13141>

Klee, S., Picart-Armada, S., Wenger, K., Birk, G., Quast, K., Veyel, D., Rist, W., Violet, C., Luippold, A., Haslinger, C., Thomas, M., Fernandez-Albert, F., & Kästle, M. (2023). Transcriptomic and proteomic profiling of young and old mice in the bleomycin model reveals high similarity [Publisher: American Physiological Society]. *American*

Journal of Physiology-Lung Cellular and Molecular Physiology, 324(3), L245–L258. <https://doi.org/10.1152/ajplung.00253.2021>

Kumari, R., & Jat, P. (2021). Mechanisms of Cellular Senescence: Cell Cycle Arrest and Senescence Associated Secretory Phenotype. *Frontiers in Cell and Developmental Biology*, 9. Retrieved July 14, 2023, from <https://www.frontiersin.org/articles/10.3389/fcell.2021.645593>

Kurz, D. J., Decary, S., Hong, Y., & Erusalimsky, J. D. (2000). Senescence-associated -galactosidase reflects an increase in lysosomal mass during replicative ageing of human endothelial cells. *Journal of Cell Science*, 113(20), 3613–3622. <https://doi.org/10.1242/jcs.113.20.3613>

Lang, N., Ansari, M., Porras-Gonzalez, D., Agami, A., Kashani, B. H., Zhou, S., Yang, L., Gerckens, M., Wei, X., Mayr, C. H., Schniering, J., Stoleriu, M.-G., Hatz, R., Behr, J., Burgstaller, G., & Schiller, H. B. (2022). Ex vivo modelling of human lung fibrogenesis and drug mode of action screens using single-cell RNA-seq in precision-cut lung slices [Publisher: European Respiratory Society Section: Mechanisms of lung injury and repair]. *ERJ Open Research*, 8(suppl 8). <https://doi.org/10.1183/23120541.LSC-2022.72>

Lee, B. Y., Han, J. A., Im, J. S., Morrone, A., Johung, K., Goodwin, E. C., Kleijer, W. J., DiMaio, D., & Hwang, E. S. (2006). Senescence-associated beta-galactosidase is lysosomal beta-galactosidase. *Aging Cell*, 5(2), 187–195. <https://doi.org/10.1111/j.1474-9726.2006.00199.x>

Lee, S., Islam, M. N., Boostanpour, K., Aran, D., Jin, G., Christenson, S., Matthay, M. A., Eckalbar, W. L., DePianto, D. J., Arron, J. R., Magee, L., Bhattacharya, S., Matsumoto, R., Kubota, M., Farber, D. L., Bhattacharya, J., Wolters, P. J., & Bhattacharya, M. (2021). Molecular programs of fibrotic change in aging human lung [Number: 1 Publisher: Nature Publishing Group]. *Nature Communications*, 12(1), 6309. <https://doi.org/10.1038/s41467-021-26603-2>

Lehmann, M., Buhl, L., Alsafadi, H. N., Klee, S., Hermann, S., Mutze, K., Ota, C., Lindner, M., Behr, J., Hilgendorff, A., Wagner, D. E., & Königshoff, M. (2018). Differential effects of Nintedanib and Pirfenidone on lung alveolar epithelial cell function in ex vivo murine and human lung tissue cultures of pulmonary fibrosis. *Respiratory Research*, 19(1), 175. <https://doi.org/10.1186/s12931-018-0876-y>

Lehmann, M., Hu, Q., Hu, Y., Hafner, K., Costa, R., van den Berg, A., & Königshoff, M. (2020). Chronic WNT/-catenin signaling induces cellular senescence in lung

epithelial cells. *Cellular Signalling*, 70, 109588. <https://doi.org/10.1016/j.cellsig.2020.109588>

Lehmann, M., Korfei, M., Mutze, K., Klee, S., Skronska-Wasek, W., Alsafadi, H. N., Ota, C., Costa, R., Schiller, H. B., Lindner, M., Wagner, D. E., Günther, A., & Königshoff, M. (2017). Senolytic drugs target alveolar epithelial cell function and attenuate experimental lung fibrosis ex vivo [Publisher: European Respiratory Society Section: Original articles]. *European Respiratory Journal*, 50(2). <https://doi.org/10.1183/13993003.02367-2016>

Li, L., Story, M., & Legerski, R. J. (2001). Cellular responses to ionizing radiation damage. *International Journal of Radiation Oncology*Biology*Physics*, 49(4), 1157–1162. [https://doi.org/10.1016/S0360-3016\(00\)01524-8](https://doi.org/10.1016/S0360-3016(00)01524-8)

Liao, Z., Yeo, H. L., Wong, S. W., & Zhao, Y. (2021). Cellular Senescence: Mechanisms and Therapeutic Potential [Number: 12 Publisher: Multidisciplinary Digital Publishing Institute]. *Biomedicines*, 9(12), 1769. <https://doi.org/10.3390/biomedicines9121769>

Liberzon, A., Birger, C., Thorvaldsdóttir, H., Ghandi, M., Mesirov, J. P., & Tamayo, P. (2015). The Molecular Signatures Database (MSigDB) hallmark gene set collection. *Cell systems*, 1(6), 417–425. <https://doi.org/10.1016/j.cels.2015.12.004>

Liberzon, A., Subramanian, A., Pinchback, R., Thorvaldsdóttir, H., Tamayo, P., & Mesirov, J. P. (2011). Molecular signatures database (MSigDB) 3.0. *Bioinformatics*, 27(12), 1739–1740. <https://doi.org/10.1093/bioinformatics/btr260>

Lin, Y., & Xu, Z. (2020). Fibroblast Senescence in Idiopathic Pulmonary Fibrosis. *Frontiers in Cell and Developmental Biology*, 8, 593283. <https://doi.org/10.3389/fcell.2020.593283>

Liu, G., Betts, C., Cunoosamy, D. M., Åberg, P. M., Hornberg, J. J., Sivars, K. B., & Cohen, T. S. (2019). Use of precision cut lung slices as a translational model for the study of lung biology. *Respiratory Research*, 20(1), 162. <https://doi.org/10.1186/s12931-019-1131-x>

Liu, T., De Los Santos, F. G., & Phan, S. H. (2017). The Bleomycin Model of Pulmonary Fibrosis. In L. Rittié (Ed.), *Fibrosis: Methods and Protocols* (pp. 27–42). Springer. https://doi.org/10.1007/978-1-4939-7113-8_2

Livak, K. J., & Schmittgen, T. D. (2001). Analysis of Relative Gene Expression Data Using Real-Time Quantitative PCR and the 2^{CT} Method. *Methods*, 25(4), 402–408. <https://doi.org/10.1006/meth.2001.1262>

López-Otín, C., Blasco, M. A., Partridge, L., Serrano, M., & Kroemer, G. (2013). The Hallmarks of Aging. *Cell*, 153(6), 1194–1217. <https://doi.org/10.1016/j.cell.2013.05.039>

López-Otín, C., Blasco, M. A., Partridge, L., Serrano, M., & Kroemer, G. (2023). Hallmarks of aging: An expanding universe. *Cell*, 186(2), 243–278. <https://doi.org/10.1016/j.cell.2022.11.001>

Lujambio, A., Akkari, L., Simon, J., Grace, D., Tschaharganeh, D. F., Bolden, J. E., Zhao, Z., Thapar, V., Joyce, J. A., Krizhanovsky, V., & Lowe, S. W. (2013). Non-cell-autonomous tumor suppression by p53. *Cell*, 153(2), 449–460. <https://doi.org/10.1016/j.cell.2013.03.020>

Lv, X., Liu, C., Liu, S., Li, Y., Wang, W., Li, K., Hua, F., Cui, B., Zhang, X., Yu, J., Yu, J., & Hu, Z. (2022). The cell cycle inhibitor P21 promotes the development of pulmonary fibrosis by suppressing lung alveolar regeneration. *Acta Pharmaceutica Sinica B*, 12(2), 735–746. <https://doi.org/10.1016/j.apsb.2021.07.015>

Maciel-Barón, L. A., Morales-Rosales, S. L., Aquino-Cruz, A. A., Triana-Martínez, F., Galván-Arzate, S., Luna-López, A., González-Puertos, V. Y., López-Díazguerrero, N. E., Torres, C., & Königsberg, M. (2016). Senescence associated secretory phenotype profile from primary lung mice fibroblasts depends on the senescence induction stimuli. *Age*, 38(1), 26. <https://doi.org/10.1007/s11357-016-9886-1>

Mei, Q., Liu, Z., Zuo, H., Yang, Z., & Qu, J. (2022). Idiopathic Pulmonary Fibrosis: An Update on Pathogenesis. *Frontiers in Pharmacology*, 12. Retrieved June 24, 2023, from <https://www.frontiersin.org/articles/10.3389/fphar.2021.797292>

Meijles, D. N., Sahoo, S., Al Ghouleh, I., Amaral, J. H., Bienes-Martinez, R., Knupp, H. E., Attaran, S., Sembrat, J. C., Nouraie, S. M., Rojas, M. M., Novelli, E. M., Gladwin, M. T., Isenberg, J. S., Cifuentes-Pagano, E., & Pagano, P. J. (2017). The matricellular protein TSP1 promotes human and mouse endothelial cell senescence through CD47 and Nox1. *Science signaling*, 10(501), eaaj1784. <https://doi.org/10.1126/scisignal.aaj1784>

Meiners, S., Eickelberg, O., & Königshoff, M. (2015). Hallmarks of the ageing lung. *The European Respiratory Journal*, 45(3), 807–827. <https://doi.org/10.1183/09031936.00186914>

Melo-Narváez, M. C., Stegmayr, J., Wagner, D. E., & Lehmann, M. (2020). Lung regeneration: Implications of the diseased niche and ageing. *European Respiratory Review*:

An Official Journal of the European Respiratory Society, 29(157), 200222. <https://doi.org/10.1183/16000617.0222-2020>

Mercer, P. F., Woodcock, H. V., Eley, J. D., Platé, M., Sulikowski, M. G., Durrenberger, P. F., Franklin, L., Nanthakumar, C. B., Man, Y., Genovese, F., McAnulty, R. J., Yang, S., Maher, T. M., Nicholson, A. G., Blanchard, A. D., Marshall, R. P., Lukey, P. T., & Chambers, R. C. (2016). Exploration of a potent PI3 kinase/mTOR inhibitor as a novel anti-fibrotic agent in IPF. *Thorax, 71*(8), 701–711. <https://doi.org/10.1136/thoraxjnl-2015-207429>

Montecino-Rodriguez, E., Berent-Maoz, B., & Dorshkind, K. (2013). Causes, consequences, and reversal of immune system aging. *The Journal of Clinical Investigation, 123*(3), 958–965. <https://doi.org/10.1172/JCI64096>

Morkel, M., Huelsken, J., Wakamiya, M., Ding, J., van de Wetering, M., Clevers, H., Taketo, M. M., Behringer, R. R., Shen, M. M., & Birchmeier, W. (2003). -Catenin regulates Cripto- and Wnt3-dependent gene expression programs in mouse axis and mesoderm formation. *Development, 130*(25), 6283–6294. <https://doi.org/10.1242/dev.00859>

Mouratis, M. A., & Aidinis, V. (2011). Modeling pulmonary fibrosis with bleomycin. *Current Opinion in Pulmonary Medicine, 17*(5), 355. <https://doi.org/10.1097/MCP.0b013e328349ac2b>

Mukherjee, A., Epperly, M. W., Shields, D., Hou, W., Fisher, R., Hamade, D., Wang, H., Saiful Huq, M., Bao, R., Tabib, T., Monier, D., Watkins, S., Calderon, M., & Greenberger, J. S. (2021). Ionizing irradiation-induced Fgr in senescent cells mediates fibrosis [Number: 1 Publisher: Nature Publishing Group]. *Cell Death Discovery, 7*(1), 1–13. <https://doi.org/10.1038/s41420-021-00741-4>

Muñoz-Espín, D., & Serrano, M. (2014). Cellular senescence: From physiology to pathology. *Nature Reviews Molecular Cell Biology, 15*(7), 482–496. <https://doi.org/10.1038/nrm3823>

Nambiar, A., Kellogg, D., Justice, J., Goros, M., Gelfond, J., Pascual, R., Hashmi, S., Masternak, M., Prata, L., LeBrasseur, N., Limper, A., Kritchevsky, S., Musi, N., Tchkonia, T., & Kirkland, J. (2023). Senolytics dasatinib and quercetin in idiopathic pulmonary fibrosis: Results of a phase I, single-blind, single-center, randomized, placebo-controlled pilot trial on feasibility and tolerability [Publisher: Elsevier]. *eBioMedicine, 90*. <https://doi.org/10.1016/j.ebiom.2023.104481>

Noda, A., Hirai, Y., Hamasaki, K., Mitani, H., Nakamura, N., & Kodama, Y. (2012). Unrepairable DNA double-strand breaks that are generated by ionising radiation

determine the fate of normal human cells. *Journal of Cell Science*, 125(22), 5280–5287. <https://doi.org/10.1242/jcs.101006>

Ovadya, Y., Landsberger, T., Leins, H., Vadai, E., Gal, H., Biran, A., Yosef, R., Sagiv, A., Agrawal, A., Shapira, A., Windheim, J., Tsoory, M., Schirmbeck, R., Amit, I., Geiger, H., & Krizhanovsky, V. (2018). Impaired immune surveillance accelerates accumulation of senescent cells and aging. *Nature Communications*, 9, 5435. <https://doi.org/10.1038/s41467-018-07825-3>

Pan, J., Li, D., Xu, Y., Zhang, J., Wang, Y., Chen, M., Lin, S., Huang, L., Chung, E. J., Citrin, D. E., Wang, Y., Hauer-Jensen, M., Zhou, D., & Meng, A. (2017). Inhibition of Bcl-2/xl With ABT-263 Selectively Kills Senescent Type II Pneumocytes and Reverses Persistent Pulmonary Fibrosis Induced by Ionizing Radiation in Mice. *International Journal of Radiation Oncology, Biology, Physics*, 99(2), 353–361. <https://doi.org/10.1016/j.ijrobp.2017.02.216>

Pereira, B. I., Devine, O. P., Vukmanovic-Stejic, M., Chambers, E. S., Subramanian, P., Patel, N., Virasami, A., Sebire, N. J., Kinsler, V., Valdovinos, A., LeSaux, C. J., Passos, J. F., Antoniou, A., Rustin, M. H. A., Campisi, J., & Akbar, A. N. (2019). Senescent cells evade immune clearance via HLA-E-mediated NK and CD8+ T cell inhibition. *Nature Communications*, 10(1), 2387. <https://doi.org/10.1038/s41467-019-10335-5>

Plovins, A., Alvarez, A. M., Ibañez, M., Molina, M., & Nombela, C. (1994). Use of fluorescein-di-beta-D-galactopyranoside (FDG) and C12-FDG as substrates for beta-galactosidase detection by flow cytometry in animal, bacterial, and yeast cells. *Applied and Environmental Microbiology*, 60(12), 4638–4641. <https://doi.org/10.1128/aem.60.12.4638-4641.1994>

Pospelova, T. V., Demidenko, Z. N., Bukreeva, E. I., Pospelov, V. A., Gudkov, A. V., & Blagosklonny, M. V. (2009). Pseudo-DNA damage response in senescent cells. *Cell Cycle (Georgetown, Tex.)*, 8(24), 4112–4118. <https://doi.org/10.4161/cc.8.24.10215>

Ptasinski, V. A., Stegmayr, J., Belvisi, M. G., Wagner, D. E., & Murray, L. A. (2021). Targeting Alveolar Repair in Idiopathic Pulmonary Fibrosis. *American Journal of Respiratory Cell and Molecular Biology*, 65(4), 347–365. <https://doi.org/10.1165/rcmb.2020-0476TR>

Radwanska, A., Cottage, C. T., Piras, A., Overed-Sayer, C., Sihlbom, C., Budida, R., Wrench, C., Connor, J., Monkley, S., Hazon, P., Schluter, H., Thomas, M. J., Hogaboam, C. M., & Murray, L. A. (2022). Increased expression and accumulation

of GDF15 in IPF extracellular matrix contribute to fibrosis. *JCI insight*, 7(16), e153058. <https://doi.org/10.1172/jci.insight.153058>

Raghu, G., Remy-Jardin, M., Myers, J. L., Richeldi, L., Ryerson, C. J., Lederer, D. J., Behr, J., Cottin, V., Danoff, S. K., Morell, F., Flaherty, K. R., Wells, A., Martinez, F. J., Azuma, A., Bice, T. J., Bouros, D., Brown, K. K., Collard, H. R., Duggal, A., ... Wilson, K. C. (2018). Diagnosis of Idiopathic Pulmonary Fibrosis. An Official ATS/ERS/JRS/ALAT Clinical Practice Guideline [Publisher: American Thoracic Society - AJRCCM]. *American Journal of Respiratory and Critical Care Medicine*, 198(5), e44–e68. <https://doi.org/10.1164/rccm.201807-1255ST>

Richeldi, L., du Bois, R. M., Raghu, G., Azuma, A., Brown, K. K., Costabel, U., Cottin, V., Flaherty, K. R., Hansell, D. M., Inoue, Y., Kim, D. S., Kolb, M., Nicholson, A. G., Noble, P. W., Selman, M., Taniguchi, H., Brun, M., Le Mauff, F., Girard, M., ... Collard, H. R. (2014). Efficacy and Safety of Nintedanib in Idiopathic Pulmonary Fibrosis. <https://doi.org/10.1056/NEJMoa1402584>

Rodier, F., Muñoz, D. P., Teachenor, R., Chu, V., Le, O., Bhaumik, D., Coppé, J.-P., Campeau, E., Beauséjour, C. M., Kim, S.-H., Davalos, A. R., & Campisi, J. (2011). DNA-SCARS: Distinct nuclear structures that sustain damage-induced senescence growth arrest and inflammatory cytokine secretion. *Journal of Cell Science*, 124(1), 68–81. <https://doi.org/10.1242/jcs.071340>

Ruwanpura, S. M., Thomas, B. J., & Bardin, P. G. (2020). Pirfenidone: Molecular Mechanisms and Potential Clinical Applications in Lung Disease [Publisher: American Thoracic Society - AJRCMB]. *American Journal of Respiratory Cell and Molecular Biology*, 62(4), 413–422. <https://doi.org/10.1165/rcmb.2019-0328TR>

Sadhu, S., Decker, C., Sansbury, B. E., Marinello, M., Seyfried, A., Howard, J., Mori, M., Hosseini, Z., Arunachalam, T., Finn, A. V., Lamar, J. M., Jourd'heuil, D., Guo, L., MacNamara, K. C., Spite, M., & Fredman, G. (2021). Radiation-Induced Macrophage Senescence Impairs Resolution Programs and Drives Cardiovascular Inflammation. *The Journal of Immunology*, 207(7), 1812–1823. <https://doi.org/10.4049/jimmunol.2100284>

Saul, D., Kosinsky, R. L., Atkinson, E. J., Doolittle, M. L., Zhang, X., LeBrasseur, N. K., Pignolo, R. J., Robbins, P. D., Niedernhofer, L. J., Ikeno, Y., Jurk, D., Passos, J. F., Hickson, L. J., Xue, A., Monroe, D. G., Tchkonia, T., Kirkland, J. L., Farr, J. N., & Khosla, S. (2022). A new gene set identifies senescent cells and predicts senescence-

associated pathways across tissues. *Nature Communications*, 13(1), 4827. <https://doi.org/10.1038/s41467-022-32552-1>

Schafer, M. J., White, T. A., Iijima, K., Haak, A. J., Ligresti, G., Atkinson, E. J., Oberg, A. L., Birch, J., Salmonowicz, H., Zhu, Y., Mazula, D. L., Brooks, R. W., Fuhrmann-Stroissnigg, H., Pirtskhalava, T., Prakash, Y. S., Tchkonia, T., Robbins, P. D., Aubry, M. C., Passos, J. F., ... LeBrasseur, N. K. (2017). Cellular senescence mediates fibrotic pulmonary disease [Number: 1 Publisher: Nature Publishing Group]. *Nature Communications*, 8(1), 14532. <https://doi.org/10.1038/ncomms14532>

Schmauck-Medina, T., Molière, A., Lautrup, S., Zhang, J., Chlopicki, S., Madsen, H. B., Cao, S., Soendenbroe, C., Mansell, E., Vestergaard, M. B., Li, Z., Shiloh, Y., Opresko, P. L., Egly, J.-M., Kirkwood, T., Verdin, E., Bohr, V. A., Cox, L. S., Stevensner, T., ... Fang, E. F. (2022). New hallmarks of ageing: A 2022 Copenhagen ageing meeting summary. *Aging (Albany NY)*, 14(16), 6829–6839. <https://doi.org/10.18632/aging.204248>

Schneider, J. L., Rowe, J. H., Garcia-de-Alba, C., Kim, C. F., Sharpe, A. H., & Haigis, M. C. (2021). The aging lung: Physiology, disease, and immunity [Publisher: Elsevier]. *Cell*, 184(8), 1990–2019. <https://doi.org/10.1016/j.cell.2021.03.005>

Schroth, J., Thiemermann, C., & Henson, S. M. (2020). Senescence and the Aging Immune System as Major Drivers of Chronic Kidney Disease. *Frontiers in Cell and Developmental Biology*, 8. Retrieved June 17, 2023, from <https://www.frontiersin.org/articles/10.3389/fcell.2020.564461>

Sellarés, J., & Rojas, M. (2019). Quercetin in Idiopathic Pulmonary Fibrosis: Another Brick in the Senolytic Wall. *American Journal of Respiratory Cell and Molecular Biology*, 60(1), 3–4. <https://doi.org/10.1165/rccb.2018-0267ED>

Selman, M., Pardo, A., & Kaminski, N. (2008). Idiopathic Pulmonary Fibrosis: Aberrant Recapitulation of Developmental Programs? *PLoS Medicine*, 5(3), e62. <https://doi.org/10.1371/journal.pmed.0050062>

Stegmayr, J., Alsafadi, H. N., Langwiński, W., Niroomand, A., Lindstedt, S., Leigh, N. D., & Wagner, D. E. (2021). Isolation of high-yield and -quality RNA from human precision-cut lung slices for RNA-sequencing and computational integration with larger patient cohorts. *American Journal of Physiology-Lung Cellular and Molecular Physiology*, 320(2), L232–L240. <https://doi.org/10.1152/ajplung.00401.2020>

Stein, G. H., Drullinger, L. F., Soulard, A., & Dulić, V. (1999). Differential roles for cyclin-dependent kinase inhibitors p21 and p16 in the mechanisms of senescence and differ-

entiation in human fibroblasts. *Molecular and Cellular Biology*, 19(3), 2109–2117. <https://doi.org/10.1128/MCB.19.3.2109>

Strunz, M., Simon, L. M., Ansari, M., Kathiriya, J. J., Angelidis, I., Mayr, C. H., Tsidiridis, G., Lange, M., Mattner, L. F., Yee, M., Ogar, P., Sengupta, A., Kukhlevich, I., Schneider, R., Zhao, Z., Voss, C., Stoeger, T., Neumann, J. H. L., Hilgendorff, A., ... Schiller, H. B. (2020). Alveolar regeneration through a Krt8+ transitional stem cell state that persists in human lung fibrosis. *Nature Communications*, 11(1), 3559. <https://doi.org/10.1038/s41467-020-17358-3>

Su, Y., Gu, H., Weng, D., Zhou, Y., Li, Q., Zhang, F., Zhang, Y., Shen, L., Hu, Y., & Li, H. (2017). Association of serum levels of laminin, type IV collagen, procollagen III N-terminal peptide, and hyaluronic acid with the progression of interstitial lung disease. *Medicine*, 96(18), e6617. <https://doi.org/10.1097/MD.0000000000006617>

Sueblinvong, V., Neujahr, D. C., Mills, S. T., Roser-Page, S., Ritzenthaler, J. D., Guidot, D., Rojas, M., & Roman, J. (2012). Predisposition for Disrepair in the Aged Lung. *The American Journal of the Medical Sciences*, 344(1), 41–51. <https://doi.org/10.1097/MAJ.0b013e318234c132>

Takekoshi, D., Matsui, Y., Akutsu, T., Nishioka, A., Kiritani, A., Okuda, K., Watanabe, J., Miyagawa, H., Utsumi, H., Hashimoto, M., Wakui, H., Minagawa, S., Hara, H., Numata, T., Noda, Y., Makishima, R., Ikegami, M., Kawabata, Y., Araya, J., & Kuwano, K. (2020). Dasatinib-induced Nonspecific Interstitial Pneumonia That Developed 7 Years after the Initiation of Dasatinib. *Internal Medicine (Tokyo, Japan)*, 59(18), 2297–2300. <https://doi.org/10.2169/internalmedicine.4714-20>

Takenouchi, Y., Kitakaze, K., Tsuboi, K., & Okamoto, Y. (2020). Growth differentiation factor 15 facilitates lung fibrosis by activating macrophages and fibroblasts. *Experimental Cell Research*, 391(2), 112010. <https://doi.org/10.1016/j.yexcr.2020.112010>

Tanabe, N., McDonough, J. E., Vasilescu, D. M., Ikezoe, K., Verleden, S. E., Xu, F., Wuyts, W. A., Vanaudenaerde, B. M., Colby, T. V., & Hogg, J. C. (2020). Pathology of Idiopathic Pulmonary Fibrosis Assessed by a Combination of Microcomputed Tomography, Histology, and Immunohistochemistry [Publisher: Elsevier]. *The American Journal of Pathology*, 190(12), 2427–2435. <https://doi.org/10.1016/j.ajpath.2020.09.001>

Tang, H., Geng, A., Zhang, T., Wang, C., Jiang, Y., & Mao, Z. (2019). Single senescent cell sequencing reveals heterogeneity in senescent cells induced by telomere erosion. *Protein & Cell*, 10(5), 370–375. <https://doi.org/10.1007/s13238-018-0591-y>

Taniguchi, H., Ebina, M., Kondoh, Y., Ogura, T., Azuma, A., Suga, M., Taguchi, Y., Takahashi, H., Nakata, K., Sato, A., Takeuchi, M., Raghu, G., Kudoh, S., Nukiwa, T., & Japan, t. P. C. S. G. i. (2010). Pirfenidone in idiopathic pulmonary fibrosis [Publisher: European Respiratory Society Section: Original Articles: Interstitial lung disease]. *European Respiratory Journal*, 35(4), 821–829. <https://doi.org/10.1183/09031936.00005209>

Team, R. D. C. (2008). R: A language and environment for statistical computing. <http://www.R-project.org>.

Thadathil, N., Selvarani, R., Mohammed, S., Nicklas, E. H., Tran, A. L., Kamal, M., Luo, W., Brown, J. L., Lawrence, M. M., Borowik, A. K., Miller, B. F., Van Remmen, H., Richardson, A., & Deepa, S. S. (2022). Senolytic treatment reduces cell senescence and necroptosis in Sod1 knockout mice that is associated with reduced inflammation and hepatocellular carcinoma. *Aging Cell*, 21(8), e13676. <https://doi.org/10.1111/acel.13676>

Uhl, F. E., Vierkotten, S., Wagner, D. E., Burgstaller, G., Costa, R., Koch, I., Lindner, M., Meiners, S., Eickelberg, O., & Königshoff, M. (2015). Preclinical validation and imaging of Wnt-induced repair in human 3D lung tissue cultures. *The European Respiratory Journal*, 46(4), 1150–1166. <https://doi.org/10.1183/09031936.00183214>

United Nations Department of Economic and Social Affairs, Population Division. (2022). World Population Prospects 2022: Summary of Results. Retrieved June 17, 2023, from <https://population.un.org/wpp/>

Veith, C., Drent, M., Bast, A., van Schooten, F. J., & Boots, A. W. (2017). The disturbed redox-balance in pulmonary fibrosis is modulated by the plant flavonoid quercetin. *Toxicology and Applied Pharmacology*, 336, 40–48. <https://doi.org/10.1016/j.taap.2017.10.001>

Verma, R., Kushwah, L., Gohel, D., Patel, M., Marvania, T., & Balakrishnan, S. (2013). Evaluating the Ameliorative Potential of Quercetin against the Bleomycin-Induced Pulmonary Fibrosis in Wistar Rats. *Pulmonary Medicine*, 2013, 921724. <https://doi.org/10.1155/2013/921724>

Victorelli, S., & Passos, J. F. (2017). Telomeres and Cell Senescence - Size Matters Not. *EBioMedicine*, 21, 14–20. <https://doi.org/10.1016/j.ebiom.2017.03.027>

Vogler, M., Dinsdale, D., Dyer, M. J. S., & Cohen, G. M. (2009). Bcl-2 inhibitors: Small molecules with a big impact on cancer therapy. *Cell Death & Differentiation*, 16(3), 360–367. <https://doi.org/10.1038/cdd.2008.137>

Wang, T.-W., Johmura, Y., Suzuki, N., Omori, S., Migita, T., Yamaguchi, K., Hatakeyama, S., Yamazaki, S., Shimizu, E., Imoto, S., Furukawa, Y., Yoshimura, A., & Nakanishi, M. (2022). Blocking PD-L1–PD-1 improves senescence surveillance and ageing phenotypes [Number: 7935 Publisher: Nature Publishing Group]. *Nature*, 611(7935), 358–364. <https://doi.org/10.1038/s41586-022-05388-4>

Wang, Y., Boerma, M., & Zhou, D. (2016). Ionizing Radiation-Induced Endothelial Cell Senescence and Cardiovascular Diseases. *Radiation research*, 186(2), 153–161. <https://doi.org/10.1667/RR14445.1>

Weatherald, J., Bondeelle, L., Chaumais, M.-C., Guignabert, C., Savale, L., Jaïs, X., Sibton, O., Rousselot, P., Humbert, M., Bergeron, A., & Montani, D. (2020). Pulmonary complications of Bcr-Abl tyrosine kinase inhibitors [Publisher: European Respiratory Society Section: Review]. *European Respiratory Journal*, 56(4). <https://doi.org/10.1183/13993003.00279-2020>

Weng, N.-p., Akbar, A. N., & Goronzy, J. (2009). CD28 T cells: Their role in the age-associated decline of immune function. *Trends in immunology*, 30(7), 306–312. <https://doi.org/10.1016/j.it.2009.03.013>

Wiley, C. D., Flynn, J. M., Morrissey, C., Lebofsky, R., Shuga, J., Dong, X., Unger, M. A., Vijg, J., Melov, S., & Campisi, J. (2017). Analysis of individual cells identifies cell-to-cell variability following induction of cellular senescence. *Aging Cell*, 16(5), 1043–1050. <https://doi.org/10.1111/acel.12632>

Wollin, L., Wex, E., Pautsch, A., Schnapp, G., Hostettler, K. E., Stowasser, S., & Kolb, M. (2015). Mode of action of nintedanib in the treatment of idiopathic pulmonary fibrosis. *The European Respiratory Journal*, 45(5), 1434–1445. <https://doi.org/10.1183/09031936.00174914>

Xie, M., Liu, X., Cao, X., Guo, M., & Li, X. (2020). Trends in prevalence and incidence of chronic respiratory diseases from 1990 to 2017. *Respiratory Research*, 21(1), 49. <https://doi.org/10.1186/s12931-020-1291-8>

Xue, W., Zender, L., Miethling, C., Dickins, R. A., Hernando, E., Krizhanovsky, V., Cordon-Cardo, C., & Lowe, S. W. (2007). Senescence and tumour clearance is triggered by p53 restoration in murine liver carcinomas. *Nature*, 445(7128), 656–660. <https://doi.org/10.1038/nature05529>

Yao, C., Guan, X., Carraro, G., Parimon, T., Liu, X., Huang, G., Soukiasian, H. J., David, G., Weigt, S. S., Belperio, J. A., Chen, P., Jiang, D., Noble, P. W., & Stripp, B. R. (2019). Senescence of alveolar stem cells drives progressive pulmonary fibrosis

[Publisher: Cold Spring Harbor Laboratory Section: New Results]. *bioRxiv*, 820175. <https://doi.org/10.1101/820175>

Yao, L., Wright, M. F., Farmer, B. C., Peterson, L. S., Khan, A. M., Zhong, J., Gewin, L., Hao, C.-M., Yang, H.-C., & Fogo, A. B. (2019). Fibroblast-specific plasminogen activator inhibitor-1 depletion ameliorates renal interstitial fibrosis after unilateral ureteral obstruction. *Nephrology, Dialysis, Transplantation: Official Publication of the European Dialysis and Transplant Association - European Renal Association*, 34(12), 2042–2050. <https://doi.org/10.1093/ndt/gfz050>

Zhang, L., Pitcher, L. E., Prahalad, V., Niedernhofer, L. J., & Robbins, P. D. (2023). Targeting cellular senescence with senotherapeutics: Senolytics and senomorphics [eprint: <https://onlinelibrary.wiley.com/doi/pdf/10.1111/febs.16350>]. *The FEBS Journal*, 290(5), 1362–1383. <https://doi.org/10.1111/febs.16350>

Zhang, Y., Jiang, M., Nouraie, M., Roth, M. G., Tabib, T., Winters, S., Chen, X., Sembrat, J., Chu, Y., Cardenes, N., Tuder, R. M., Herzog, E. L., Ryu, C., Rojas, M., Lafyatis, R., Gibson, K. F., McDyer, J. F., Kass, D. J., & Alder, J. K. (2019). GDF15 is an epithelial-derived biomarker of idiopathic pulmonary fibrosis. *American Journal of Physiology. Lung Cellular and Molecular Physiology*, 317(4), L510–L521. <https://doi.org/10.1152/ajplung.00062.2019>

Zheng, Q., Cox, I. A., Campbell, J. A., Xia, Q., Otahal, P., Graaff, B. d., Corte, T. J., Teoh, A. K. Y., Walters, E. H., & Palmer, A. J. (2022). Mortality and survival in idiopathic pulmonary fibrosis: A systematic review and meta-analysis [Publisher: European Respiratory Society Section: Review]. *ERJ Open Research*. <https://doi.org/10.1183/23120541.00591-2021>

Zhou, S., Zhu, J., Zhou, P.-K., & Gu, Y. (2022). Alveolar type 2 epithelial cell senescence and radiation-induced pulmonary fibrosis. *Frontiers in Cell and Developmental Biology*, 10. Retrieved July 14, 2023, from <https://www.frontiersin.org/articles/10.3389/fcell.2022.999600>

Zhu, Y., Tchkonia, T., Fuhrmann-Stroissnigg, H., Dai, H. M., Ling, Y. Y., Stout, M. B., Pirtskhalava, T., Giorgadze, N., Johnson, K. O., Giles, C. B., Wren, J. D., Niedernhofer, L. J., Robbins, P. D., & Kirkland, J. L. (2016). Identification of a novel senolytic agent, navitoclax, targeting the Bcl-2 family of anti-apoptotic factors. *Aging Cell*, 15(3), 428–435. <https://doi.org/10.1111/acel.12445>

Zhu, Y., Tchkonia, T., Pirtskhalava, T., Gower, A. C., Ding, H., Giorgadze, N., Palmer, A. K., Ikeno, Y., Hubbard, G. B., Lenburg, M., O'Hara, S. P., LaRusso, N. F.,

Miller, J. D., Roos, C. M., Verzosa, G. C., LeBrasseur, N. K., Wren, J. D., Farr, J. N., Khosla, S., ... Kirkland, J. L. (2015). The Achilles' heel of senescent cells: From transcriptome to senolytic drugs. *Aging Cell*, 14(4), 644–658. <https://doi.org/10.1111/acel.12344>

Acknowledgments

I would like to thank my parents, Catalina and Rafael, for their support and love during my career and the weekly video calls that kept us closer during these years. I would like to thank my sister Angélica for being there when I needed you and being my confidant. I am eternally thankful to my fiance Aníbal for his constant support, love, and company every day during this journey. This would not have been possible without you!

I want specially thank my mentor Mareike Lehmann for trusting me with her first project, supporting me in every step of this process, and encouraging me every time to try new things to advance my career. Also for your trust and friendship during these years and for showing me with your example, how to be a passionate researcher! I would also like to thank all the members of my thesis committee: Melanie Königshoff, Jürgen Behr, and Heiko Adler for their invaluable support and guidance that help me to advance my doctoral project.

I am thankful to all my colleagues and friends at the transatlantic pink lab: QJ, Nora, Fenja, Bea, Carina, Gowtham, Eshita, Tudor, Anastasia, and Kathrin for supporting me and making research fun and rewarding every day. Also for all my mentees for giving me the opportunity to build myself as a mentor. I would like to thank all the Cell Circuits group, especially Janine for being my mentor and introducing me to the world of *in situ* proteomics. I would also like to thank Diana for her friendship and companionship over these years and for all the experiences we shared in this crazy world of the PCLS. Also, thanks to Sara for your friendship and support for my project. I would also like to thank everyone from the LHI, the CPC, and the research schools at Helmholtz for their support, especially Önder and Claudia for their professional support and guidance.

Finally, I gratefully acknowledge the provision of human biomaterial and clinical data from the CPC-M bioArchive and its partners at the Asklepios Biobank Gauting, the LMU Hospital, and the Ludwig-Maximilians-Universität München. I thank the patients and their families for their support. I also would like to thank Anja, Diana, Verena, and the whole CPC-bioArchive team for their help and support during these years. Moreover, I acknowledge funding from the Deutsche Forschungsgemeinschaft (DFG, German Research Foundation) – 512453064, Federal Institute for Risk Assessment (Bundesinstitut für Risikoforschung, BfR) 60-0102-01.P588, and the German Center for Lung Research (DZL).

I am incredibly happy and grateful for these years of medical research, for all the friendships that I found

on the way, and for everything that I learned during this time. Thank you to everyone that made this possible. Now it is time to celebrate that I can finally call myself Dr. Camila Melo!

MARÍA CAMILA MELO NARVÁEZ

Doctoral candidate in Medical Research

✉ maria.melonarvaez@helmholtz-munich.de

📞 +491737586894

📍 Munich, Germany

EXPERIENCE

Student Assistant

AGV research unit gene vectors, Helmholtz Zentrum München

📅 Feb 2019 – Dec 2019 📍 Munich, Germany

Graduate Teaching Assistant

Laboratory of Molecular Diagnosis and Bioinformatics LDMB, Universidad de los Andes

📅 Jan 2017 – May 2017 📍 Bogotá, Colombia

Research Assistant

Center of Microscopy, Universidad de los Andes

📅 Jun 2016 – Dec 2016 📍 Bogotá, Colombia

Student Assistant - Virology Laboratory

Universidad de los Andes

📅 Aug 2016 – Nov 2016 📍 Bogotá, Colombia

Student Assistant - Molecular Biology Laboratory

Universidad de los Andes

📅 Jan 2016 – May 2016 📍 Bogotá, Colombia

📅 Aug 2013 – Nov 2013

EDUCATION

Master of Science (Biology)

Ludwig-Maximilians Universität München

📅 2017-2019 📍 Munich, Germany

Bachelor of Science (Microbiology)

Universidad de los Andes

📅 2012-2016 📍 Bogotá, Colombia

High School Diploma

Teresiano School

📅 2001-2011 📍 Bogotá, Colombia

FUNDING AND AWARDS

Grant Writing Challenge 2021

Comprehensive Pneumology Center Research School "Lung Biology and disease"

📅 Oct, 2021 – Oct 2022 📍 Munich, Germany

- Award: 2000 Euros for research proposal

Scholarship Program for Foreign Students

Konrad Adenauer Foundation

📅 Oct, 2017 – Dec, 2019 📍 Munich, Germany

- 2-year fully-funded scholarship for master studies in a German university

RESEARCH PROJECTS

Doctoral thesis: Lung aging in the dish

Institute of Lung Health and Immunity, LHI, CPC München, Helmholtz Center Munich

📅 March 2020 – today 📍 Munich, Germany

Master Thesis: Silencing of cellular genes by vector-borne artificial siRNA during the early phase of EBV infection of B lymphocytes

Helmholtz Zentrum München

📅 May, 2019-Nov 2019 📍 Munich, Germany

Research Internship

Clinic and polyclinic for radiotherapy and radio-oncology LMU

📅 Oct, 2018-Nov, 2018 📍 Munich, Germany

- Image analysis of spheroid formation capacity

Research Internship

AGV research unit gene vectors, Helmholtz Zentrum München

📅 May, 2018-Jun, 2018 📍 Germany

- BAC recombineering and HEK293-based viral production

Bachelor Thesis: Genotyping of *vacA* and *cagA* of *Helicobacter pylori* strains isolated from Colombian adult Patients and their possible association with the presence of gastric pathologies

Laboratory of Molecular Diagnosis and Bioinformatics LDMB, Universidad de los Andes

📅 Jan, 2016 - Dec, 2016 📍 Bogotá, Colombia

Doctoral Candidate Assistant

Laboratory of Molecular Diagnosis and Bioinformatics LDMB, Universidad de los Andes

📅 Jun, 2014 - Dec, 2016 📍 Bogotá, Colombia

- Molecular identification of clinical strains of *Helicobacter pylori*

RESEARCH INTERESTS

- Chronic Lung Diseases
- Infectious diseases
- Immunology
- Aging

CONFERENCE TALKS

Using PCLS to study premature aging phenotypes in the human lung

DZL DPLD Annual meeting 2023

Jun 2023

📍 Fuerstenfeldbruck, Germany

Cellular aging of the alveolar epithelium contributes to non-resolving fibrosis of the lung

2nd Academy Symposium of the DZL

Nov 2022

📍 Giessen, Germany

Induction of epithelial cellular senescence and pro-fibrotic changes in human precision-cut lung slices

DGP-Herbsttagung der Sektion Zellbiologie

Oct 2022

📍 Marburg, Germany

Invited talk: Lung Aging in a dish

MBML Annual Retreat 2022

Oct 2022

📍 Giessen, Germany

POSTER SESSIONS

Teaser: "Lung aging in a dish": Epithelial cellular senescence and pro-fibrotic changes in human precision-cut lung slices

DZL Annual Meeting 2023

Jun 2023

📍 Fuerstenfeldbruck, Germany

Induction of epithelial cellular senescence in precision-cut lung slices

DZL Annual Meeting 2022

Jul 2022

📍 Hannover, Germany

RAPiD: Rapid Abstract Poster Discussion: A Human Ex Vivo Model of Lung Cellular Senescence to Study Age-Related Pulmonary Diseases

2022 ATS International Conference

May 2022

📍 San Francisco, USA

An ex vivo model of cellular senescence and inflammmaging in precision-cut lung slices

ERS Lung Science Conference 2022

March 2022

📍 Estoril, Portugal

Genotyping of *vacA* and *cagA* of *Helicobacter pylori* strains isolated from Colombian adult Patients and their possible association with the presence of gastric pathologies

Pan American Digestive Week 2016

Sep 2016

📍 Cartagena, Colombia

PUBLICATIONS

• Bramley N. & Melo-Narváez MC., et al. Primary human lung fibroblasts exhibit trigger- but not disease-specific cellular senescence and impair alveolar epithelial cell progenitor function. bioRxiv (2023); DOI: [10.1101/2023.07.24.550385](https://doi.org/10.1101/2023.07.24.550385).

• Heinzemann K, et al. Single-cell RNA sequencing identifies G-protein coupled receptor 87 as a basal cell marker expressed in distal honeycomb cysts in idiopathic pulmonary fibrosis. Eur Respir J. (2022);59(6):2102373. DOI: [10.1183/13993003.02373-2021](https://doi.org/10.1183/13993003.02373-2021).

• Mei, J., et al. Development of a model for fibroblast-led collective migration from breast cancer cell spheroids to study radiation effects on invasiveness. Radiat Oncol 16, 159 (2021). DOI:<https://doi.org/10.1186/s13014-021-01883-6>

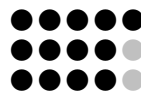
• Melo-Narváez MC., et al. Lung regeneration: implications of the diseased niche and aging. Eur Respir Rev. (2020); 29(157):200222. DOI:[10.1183/16000617.0222-2020](https://doi.org/10.1183/16000617.0222-2020)

• Liu, WH., et al. Inducible transgene expression in PDX models in vivo identifies KLF4 as a therapeutic target for B-ALL. Biomark Res 8, 46 (2020). DOI: <https://doi.org/10.1186/s40364-020-00226-z>

• Melo-Narváez MC., et al. Genotyping of *cagA* and the intermediate region of *vacA* in strains of *Helicobacter pylori* isolated from Colombian adult patients and associations with gastric diseases. 1. (2018);33(2):103-10. DOI:<https://doi.org/10.22516/25007440.168>

LANGUAGE SKILLS

Spanish



English

German

SOFTWARE SKILLS

R



ImageJ



GraphPad Prism



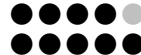
Zen Blue



MacVector



CLC Main Workbench



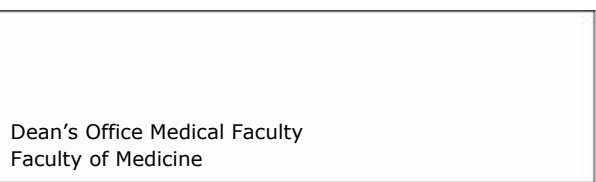
Adobe Illustrator



MS Office

List of publications

- Bramey N. & Melo-Narváez MC., et al. Primary human lung fibroblasts exhibit trigger- but not disease-specific cellular senescence and impair alveolar epithelial cell progenitor function. bioRxiv (2023); DOI: [10.1101/2023.07.24.550385](https://doi.org/10.1101/2023.07.24.550385).
- Heinzelmann K, et al. Single-cell RNA sequencing identifies G-protein coupled receptor 87 as a basal cell marker expressed in distal honeycomb cysts in idiopathic pulmonary fibrosis. Eur Respir J. (2022);59(6):2102373. DOI: [10.1183/13993003.02373-2021](https://doi.org/10.1183/13993003.02373-2021).
- Mei, J., et al. Development of a model for fibroblast-led collective migration from breast cancer cell spheroids to study radiation effects on invasiveness. Radiat Oncol 16, 159 (2021). DOI: [10.1186/s13014-021-01883-6](https://doi.org/10.1186/s13014-021-01883-6)
- Melo-Narváez MC., et al. Lung regeneration: implications of the diseased niche and ageing. Eur Respir Rev. (2020); 29(157):200222. DOI: [10.1183/16000617.0222-2020](https://doi.org/10.1183/16000617.0222-2020)
- Liu, WH., et al. Inducible transgene expression in PDX models in vivo identifies KLF4 as a therapeutic target for B-ALL. Biomark Res 8, 46 (2020). DOI: [10.1186/s40364-020-00226-z](https://doi.org/10.1186/s40364-020-00226-z)
- Melo-Narváez MC., et al. Genotyping of *cagA* and the intermediate region of *vacA* in strains of *Helicobacter pylori* isolated from Colombian adult patients and associations with gastric diseases. 1. (2018);33(2):103–10. DOI:[10.22516/25007440.168](https://doi.org/10.22516/25007440.168)



Affidavit

Melo Narvaez, Maria Camila

Surname, first name

Max-Lebsche-Platz 31, 81377 München

Address

I hereby declare, that the submitted thesis entitled

Lung Aging in a Dish: Induction of senescence and pro-fibrotic changes in
human precision-cut lung slices

is my own work. I have only used the sources indicated and have not made unauthorised use of services
of a third party. Where the work of others has been quoted or reproduced, the source is always given.

I further declare that the dissertation presented here has not been submitted in the same or simi-
lar form to any other institution for the purpose of obtaining an academic degree.

Munich, 22.01.2024

Maria Camila Melo

Place, Date

Signature doctoral candidate

**Confirmation of congruency between printed and electronic version of the
doctoral thesis**

Doctoral candidate: Maria Camila Melo Narvaez

Address: Max-Lebsche-Platz 31, 81377 München

I hereby declare that the electronic version of the submitted thesis, entitled
Lung Aging in a Dish: Induction of senescence and pro-fibrotic changes in
human precision-cut lung slices
is congruent with the printed version both in content and format.

Munich, 22.01.2024

Place, Date

Maria Camila Melo

Signature doctoral candidate